Testing halo mass functions and heavy seed formation pathways in the high-redshift Universe

Hannah O'Brennan
BA, MSc

Thesis presented for the degree of

Doctor of Philosophy

to

Maynooth University
Department of Physics

April 2025

Department Head

Dr. Neil Trappe

Research advisor

Dr. John Regan

Contents

Declaration

This thesis has not been submitted in whole, or in part, to this or any other university for any other degree and is, except where otherwise stated, the original work of the author.

Chapter 2 is based on the article "Halo mass functions at high redshift" published in Volume 7 of the Open Journal of Astrophysics in (which can be found here: https://doi.org/10.33232/001c.126010). The methodology and results were developed by the author. John Regan provided feedback; Chris Power provided feedback and we used the `hmf` and `halomod` packages which he developed; John Brennan provided training in running `Enzo` simulations; Saoirse Ward provided training in using `MUSIC` and running `SWIFT` simulations; Joe McCaffrey providing training in using `MUSIC`.

Chapter 3 is based on the article "Predicting the number density of heavy seed massive black holes due to an intense Lyman-Werner field" published in Volume 8 of the Open Journal of Astrophysics (which can be found here: https://doi.org/10.33232/001c.141953). The methodology and results were developed by the author. John Regan shared output data from the `Renaissance` simulations and provided feedback; Eli Visbal and John Wise provided feedback; John Brennan reviewed the analysis pipeline; Joe McCaffrey shared data from his own work post-processing `Renaissance` data; Alessandro Trinca shared data from his own work using the Cosmic Archaeology Tool; Michael L. Norman is a co-author as we used data from the `Renaissance` simulations (Xu et al., 2016b).

Hannah O'Brennan, August 20, 2025

Acknowledgments

First, I want to thank my wonderful family for always supporting me unconditionally and nourishing my passion for physics. I appreciate every book I was gifted and every interesting science article sent my way. Thank you to Mam, Dad, Callum, Nathan, my grandparents Harry and Helen and the rest of my extended family. Thank you to my family chickens and also my late pets Pippin, Tabby and Garfield for the somewhat one-sided conversations and great comfort. Next I want to thank my fantastic partner Carolyn for being there for me through this entire journey and especially for the past year. Thank you for your patience, kindness and all the times you've cheered me up when I needed it. Thank you also to her family for always being very welcoming to me and providing many a Sunday dinner.

I want to thank my supervisor John Regan for getting me this far, providing incredibly helpful feedback and guidance, and making me a better physicist. I feel very lucky to have been part of such a wonderful research group with everyone willing to collaborate, share knowledge or provide a second opinion. Thank you to all group members past and present: Stefan, Joe, Saoirse, John Brennan, Pelle, Daxal and Lewis. Thank you especially to Joe, Saoirse, Daxal and Aoibhinn for making our office such a welcoming space. I also want to thank the co-authors on my submitted papers whose contributions helped make this thesis possible: Chris Power, Eli Visbal, John Wise, Alessandro Trinca and Michael L. Norman.

I am very glad to have been in a very friendly and easy-going department and sharing my work days with the rest of the theoretical physics corridor. In addition to those already mentioned, this includes Eddie, Gerhard, Rachel, Kay, John Ibrahim, Jasmine, Dale, Phil, Aonghus, Stephen, Gert, Nathan, Babatunde, Graham, Peter, Paul, Jiří, Joost, Jon-Ivar and Suzie. I also really enjoyed getting to know those upstairs in experimental physics during the weekly astrophysics coffee mornings (not just for the biscuits). I also appreciate the undergraduate and taught postgraduate students for making the coffee room lively and full of good chat.

I want to thank my friends from school, Trinity College Dublin, the University of Edinburgh and elsewhere for your continued support, studying with me and helping me believe in myself. I am very grateful to my family friends John and

Ann whom I lived with for the entirety of my undergraduate free of charge. Their unbelievable generosity cannot be thanked for enough and was vital for the start of my journey into physics.

I was taught by many wonderful teachers, lecturers and supervisors. I want to especially thank my school teachers Frank McQuaid, Kathryn Higgins and Jimmy Brophy and my past project supervisors Mauro Ferreira, Leron Borsten and James Lucietti.

At time of writing I cannot drive so I am incredibly grateful to every Bus Éireann, Dublin Bus, Luas and Irish Rail driver who got me to work and got me home. I also want to thank all the staff who run arXiv.org and the Astrophysics Data System (ADS). These are both incredibly underrated projects that have given me and millions of others free access to almost any academic paper that we would need. Completing this thesis would have been much more cumbersome without the invaluable access they provide. I am very grateful to staff at the Irish Centre for High End Computing (ICHEC), EuroHPC and IT4Innovations for providing access to the supercomputers Kay, MeluXina and Karolina respectively and for addressing any issues I had.

Finally I want to thank the Maynooth University Library Cat whose sighting was always a lovely part of my day as well as letting me give him the occasional head scratch.

Abstract

We investigate the high-redshift ($z \geq 10$) Universe i.e. when it was < 1 Gyr old. We focus our investigation in two main areas: the distribution of dark matter (DM) halos and the formation of intermediate-mass ($M \sim 10^3 - 10^5$ $M_\odot$) black holes (IMBHs). We examine the abundance of DM halos as a function of redshift and mass using N-body simulations. We also analyse the influence of both Lyman-Werner (LW) radiation and metal enrichment on the number density of IMBHs using analytic models and by post-processing simulation data.

We first review the state of the field today by discussing the fundamentals of Λ-Cold Dark Matter (ΛCDM), DM clustering on both small and large scales, quasars and the supermassive black holes (SMBHs) that power them. We also detail how data from the James Webb Space Telescope (JWST) have prompted us to question the origins of SMBHs and have shown us how different the high-z Universe is from the local one ($z \sim 0$). Finally, we describe the computational tools employed in our investigations.

Next we use the adaptive mesh-refinement code `Enzo` and the N-body smoothed particle hydrodynamics code `SWIFT` to compare (semi-)analytic DM halo mass functions against the results of direct N-body models at high redshift. Our goal is to investigate if these fitting functions could be a source of error when comparing JWST data to cosmological models.

Next we compare the number density of IMBHs informed by an analytic model accounting for LW radiation and metal pollution with one informed by simulation results from `Renaissance`. This is a high-resolution simulation suite with the purpose of probing the high-z Universe. Our goal is to determine if recent JWST observations could be accounted for by this heavy seed formation pathway alone. We also compare this channel against other recent models in the literature.

Finally, we summarise our aims, methodology, conclusions and we briefly discuss how this work could be expanded upon in future. In §2, we find that the difference between direct N-body calculations and (semi-)analytic halo mass function fits is generally $<$ a factor of 2 (at $z \sim 10$) within the mass range of galaxies currently being observed by JWST, and is therefore not a dominant source of error when comparing theory and observation at high redshift. In §3, we find the highest number densities ($n_{\text{heavy seed host}} \sim 10^{-4}$ comoving Mpc^{-3} at

$z \sim 10$) are still too low for this channel to be the dominant formation pathway for heavy seeds when compared to JWST observations, especially when considering the growth requirements and duty cycle of active galactic nuclei (AGNs) necessary. This channel can at best be responsible for only a small subset of high-z AGNs while other models from the literature (e.g. rapid assembly) are more promising to explain JWST observations at high redshift.

Chapter 1

Introduction

1.1 Cosmology

Cosmology is the study of the Universe and the Universe is simply all that was, is and will ever be. Easy-peasy. Cosmologists concern themselves with the birth, evolution, structure and death of the Universe. The current consensus tells us that the Universe as we know it began ~ 13.8 billion years ago with a Big Bang. The first physical evidence for this was found in 1929 when Edwin Hubble found that the galaxies furthest from Earth also had the greatest velocities i.e. space is expanding away from us (Hubble, 1929). Due to the finite speed of light, we observe the most distant galaxies as they appeared billions of years ago i.e. observations of distant space are synonymous with observations of the distant past.

The Big Bang was followed by a short period ($\sim 10^{-32}$ s) of rapid expansion called inflation, subsequently causing quantum fluctuations in the infant Universe (Starobinskiĭ, 1979; Guth, 1981). At this time, there were no atoms or even protons yet but a quark-gluon soup. By the time the Universe was ~ 3 minutes old, quarks combined to form protons and neutrons. These early baryons went on to form hydrogen and helium nuclei in a process known as nucleosynthesis.

At this stage, we have nuclei, electrons and photons in a hot, high-density plasma with participants frequently scattering off one another. The collisions are so frequent that the mean free path of photons is incredibly short, such that it is near-impossible for a photon to travel through the ionised gas without being scattered i.e. photons at this stage in the evolution of the Universe will never reach us. Then, about 380,000 years after the Big Bang, we have recombination (nuclei combining with electrons forming neutral hydrogen) and decoupling (photons have a large enough mean free path to separate from the gas). At this time of last scattering, the photons escape and may be seen today as the Cosmic Microwave Background (CMB). The existence of the CMB was first predicted by George Gamow, Ralph Alpher and Robert Herman in 1948 (Alpher & Herman,

1948) and later detected by Arno Penzias and Robert Wilson in 1964 (Penzias & Wilson, 1965). The CMB is largely uniform in temperature and density aside from some inhomogeneities (1 in 10^5) that were seeded by the post-inflation quantum fluctuations.

What follows for about 100 Myr is known as the Cosmic Dark Ages: the Universe consists largely of neutral hydrogen and no stars have formed yet. The CMB inhomogeneities result in regions of overdensity, which later evolve to form the first stars and proto-galaxies. The photons emitted by the first stars gradually reionize the neutral hydrogen for approximately 600 Myr from redshift $z = 15$ to $z = 6$ (Robertson et al., 2015; De Barros et al., 2017; Wise, 2019; Witten et al., 2024). Redshift is a means of describing a point in the Universe's history where low-redshift refers to the recent past (with $z = 0$ being present-day), while high-redshift refers to points early in the Universe's evolution (with $z \to \infty$ referring to the Big Bang).

Following reionization and the formation of the first galaxies, the Universe continues to expand and reaches Cosmic Noon at $z \sim 2$ when it was approximately 2 Gyr old. During this time, the global star formation rate density peaks at approximately 10^{-1} $M_\odot$ yr^{-1} Mpc^{-3}, compared to $\sim 10^{-2}$ $M_\odot$ yr^{-1} Mpc^{-3} in the present day (Madau & Dickinson, 2014). About half of the stellar mass observed today was formed between $z \sim 3$ and $z \sim 1$ while Universe doubled in size due to expansion (Förster Schreiber & Wuyts, 2020).

Today our Universe is highly ionised and made up of billions of galaxies that continue to expand away from one another. We can trace this expansion using the scale factor $a(t)$ as a function of time, where $t = 0$ refers to the Big Bang and $t = t_0$ refers to the present day. The scale factor is a fraction of the Universe's present-day size i.e. $a = 1/2$ refers to when the Universe was half its current size and $a(t = t_0) = 1$ in the present day. As $t \to 0$, $a(t) \to 0$ i.e. the Big Bang singularity. We describe the relationship between the scale factor and time in greater detail in §1.2.

As the distance between present-day Earth and some distant galaxy expands, the wavelength of photons emitted by stars within that galaxy increases i.e. the wavelength is redshifted by the time we measure it.

$$\begin{aligned} z &= \frac{\lambda_{\text{obs}} - \lambda_{\text{emit}}}{\lambda_{\text{emit}}} = \frac{\lambda_{\text{obs}}}{\lambda_{\text{emit}}} - 1, \\ 1 + z &= \frac{\lambda_{\text{obs}}}{\lambda_{\text{emit}}}. \end{aligned} \tag{1.1}$$

We set the scale factor $a = 1/(1 + z)$ i.e. low-redshift refers to the local Universe and recent past where $a \sim 1$, high-redshift refers to points very distant from Earth and early in the Universe's history where $a \to 0$. Figure 1.1 summarises the evolution of the Universe as a function of its age and redshift.

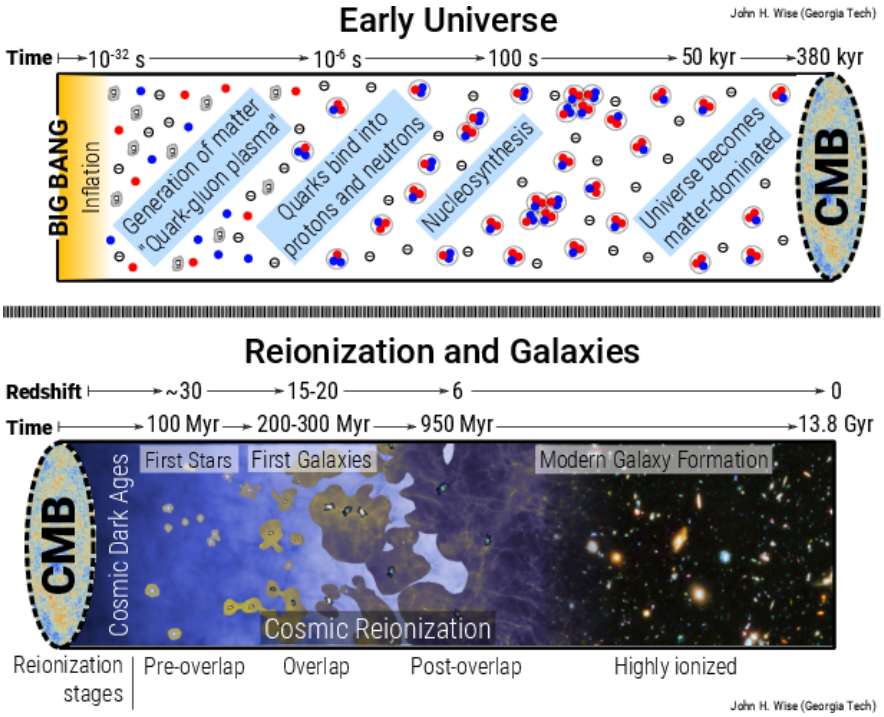

Figure 1.1: Timeline of the Universe, taken from Figure 1 of Wise (2019). Note that time as a variable here refers to time since the Big Bang.

We can relate this scale factor a which describes the expansion of the Universe to a so-called co-moving distance. Consider a photon that is emitted at some time $t' = t$ and some distance from present-day Earth $r' = r$. The photon arrives at $r' = 0$ and $t' = t_0$ where $t_0 > t$. We can express the co-moving distance travelled r in terms of a as:

$$\begin{aligned} \int_0^r dr' &= -\int_{t_0}^{t} \frac{cdt'}{a(t')}, \\ r &= \int_t^{t_0} \frac{cdt'}{a(t')}, \end{aligned} \tag{1.2}$$

i.e. as $t \to 0$, $a(t) \to 0$ in an expanding Universe and the co-moving distance travelled r increases. This depends on how the scale factor $a(t)$ evolves with time t which is dependent on the matter-energy content of the Universe (see §1.2). Comoving distances are measured in comoving units e.g. cMpc refers to units of comoving Mpc. We can relate the physical distance between two points to comoving distance as:

$$\begin{aligned} r_{\rm phys} &= a(t) r_{\rm co}, \\ r_{\rm phys} &= \frac{1}{1+z} r_{\rm co}. \end{aligned} \tag{1.3}$$

Our primary concern in this work is with the high-redshift ($z \geq 10$) Universe i.e. when the Universe was less than 1 Gyr old and when the supermassive black holes (SMBHs) that power galactic centres today were first seeded. In §1.2, we detail the standard model of cosmology that we utilise, $\Lambda-$Cold Dark Matter, and

its main parameters. In §1.3, we describe the structure of cold dark matter on small scales i.e. halos (§1.3.1) and on larger scales i.e. the Cosmic Web (§1.3.2). These halos are the hosts of galaxies and some host SMBHs. These SMBHs accrete matter, producing the incredible luminosities of quasars. In §1.4, we discuss the properties of these quasars and their discovery history. Since the launch of the James Webb Space Telescope (JWST) in 2021, we have entered a new era of high-redshift observational astrophysics. In §1.5, we illustrate some of the recent discoveries of JWST and what they tell us about SMBHs and their seeding mechanisms in the early Universe. Finally for this Chapter, in §1.6 we describe the computational tools employed in §2 and §3.

1.2 ΛCDM Paradigm

In this section, we define the parameters in use in §2 and §3 of the current standard model of cosmology Λ−Cold Dark Matter (ΛCDM).
In 1915, Albert Einstein published his general theory of relativity, describing how matter and energy curve spacetime (Einstein, 1915). This can be summarised in the Einstein field equations in tensor form:

$$R_{\mu\nu} - \frac{1}{2}Rg_{\mu\nu} + \Lambda g_{\mu\nu} = \frac{8\pi G}{c^4}T_{\mu\nu}, \tag{1.4}$$

where $g_{\mu\nu}$ is the spacetime metric and the unknown of this equation. The indices μ, ν refer to spacetime coordinates t, r, θ or ϕ (time and spherical space coordinates). $R_{\mu\nu}$ and R are the Ricci tensor and Ricci scalar respectively - they are functions of $g_{\mu\nu}$ and its derivatives with respect to the spacetime coordinates. $T_{\mu\nu}$ is the stress-energy tensor and is a function of density ρ, pressure p and $g_{\mu\nu}$. Finally, Λ is the cosmological constant. The left-hand side of this equation describes the curvature of spacetime and the right-hand side of the equation describes the matter and energy curving spacetime.

A solution to Eq. 1.4 is the Friedmann-Lemaître-Robertson-Walker (FLRW) metric (Friedmann, 1922; Lemaître, 1931; Robertson, 1935, 1936a,b; Walker, 1937), which describes a universe that is isotropic and homogeneous. This is, of course, a simplification as the presence of planets, stars and galaxies tells us that the Universe is not truly homogeneous in density. However this metric remains a very useful approximation to describe the Universe on cosmic scales. Due to this isotropy and homogeneity, we can assume spherical symmetry as follows:

$$(ds)^2 = c^2(dt)^2 - a(t)^2\left(\frac{(dr)^2}{1-kr^2} + r^2(d\Omega)^2\right), \tag{1.5}$$

where t is our coordinate indicating time since the Big Bang, $a(t)$ is the dimensionless scale factor described in §1.1, r is our radial coordinate, k describes the

curvature of the Universe and $d\Omega = \sin\theta\, d\theta\, d\phi$ is the solid angle measure. We need the scale factor $a(t)$ in order to account for the expansion of the Universe while we measure the distance between two points. The r coordinate does not vary with time or redshift and is a comoving distance. The index k describes the curvature of the Universe as:

$$k = \begin{cases} -1\,\text{cMpc}^{-2} & \text{hyperbolic (open)}, \\ 0 & \text{Euclidean (flat)}, \\ 1\,\text{cMpc}^{-2} & \text{elliptical (closed)}, \end{cases} \tag{1.6}$$

where r is in units of cMpc. By substituting this metric into the Einstein field equations, we are left with the first Friedmann equation:

$$\left(\frac{\dot{a}(t)}{a(t)}\right)^2 = H(t)^2 = \frac{8\pi G}{3}\rho(t) - \frac{kc^2}{a(t)^2} + \frac{\Lambda c^2}{3}. \tag{1.7}$$

This illustrates how the scale factor $a(t)$ i.e. the size of the Universe evolves with time. Note that while $a(t)$ is dimensionless, both k and Λ have dimensions of length^{-2}. The Hubble parameter $H(t)$ describes the rate of expansion normalised by the scale factor at a given time. At $t = t_0$ and $a = 1$, $H(t = t_0) = H_0$ i.e. the Hubble constant. It is given in units of km s^{-1} Mpc^{-1}. If we set $H_0 = 70$ km s^{-1} Mpc^{-1}, then two points separated by 1 Mpc would recede from one another at 70 km/s.

The expansion of the Universe is driven by the density of matter and radiation $\rho(t)$ and the cosmological constant Λ in a flat universe ($k = 0$). Matter refers to both baryonic matter which can be detected electromagnetically and dark matter which cannot. Dark matter only interacts with the gravitational force and its exact nature has yet to be determined at time of writing. In 1933, its presence was inferred by Fritz Zwicky through measurements of galaxy velocities within a galaxy cluster (Zwicky, 1933, 1937). He determined that the galaxies were moving too quickly given their (baryonic) mass and that some invisible mass ought to be present too. Later in the 1970s, Vera Rubin and W. Kent Ford, Jr. found a similar result when examining galaxy rotation curves (Rubin & Ford, 1970): the rotational velocity of a galaxy was too high given the baryonic mass known, implying that another type of matter must also contribute to the total galaxy mass. The existence of dark matter can also be inferred by examining the baryon acoustic oscillations, driving some CMB temperature anisotropies (Planck Collaboration et al., 2014). The model we use for dark matter is currently the more favoured in modern cosmology: cold dark matter, whose particles move at non-relativistic velocities. We can rescale $\rho(t)$ by a constant to include the contribution from Λ like so:

$$
\begin{aligned}
H(t)^2 &= \frac{8\pi G}{3}\Big(\rho(t) + \frac{\Lambda c^2}{8\pi G}\Big) - \frac{kc^2}{a(t)^2}, \\
\rightarrow H(t)^2 &= \frac{8\pi G}{3}\rho(t) - \frac{kc^2}{a(t)^2}, \\
\rho(t) &= \rho_{\mathrm{m}}(t) + \rho_{\mathrm{r}}(t) + \rho_{\Lambda}, \\
\rho(t) &= \rho_{\mathrm{m},0}a(t)^{-3} + \rho_{\mathrm{r},0}a(t)^{-4} + \rho_{\Lambda},
\end{aligned}
\tag{1.8}
$$

where ρ_{m} is the density of matter, ρ_{r} is the density of radiation and now ρ_{Λ} is known as the density of dark energy. Due to the $a(t)^{-4}$ dependence, the total density was dominated by radiation ($\rho_{\mathrm{r}}(t)$) for the lowest values of $a(t)$ i.e. early in the evolution of the Universe, until approximately 30,000 years after the Big Bang. This was followed then by a matter-dominated era due to the $a(t)^{-3}$ dependence of $\rho_{\mathrm{m}}(t)$, until approximately 9 billion years after the Big Bang. Finally, about 4 billion years ago, the Universe entered the dark energy-dominated era. Dark energy has yet to be detected but has been driving the acceleration of the expansion of the Universe. Note that ρ_{Λ} is constant in t in this model but there exist others where the dark energy density evolves with time (Copeland et al., 2006; Carloni et al., 2025).

From here, we can solve for the critical density i.e. the density of matter, radiation and dark energy required for the Universe to be flat in curvature ($k = 0$):

$$
\begin{aligned}
H(t)^2 &= \frac{8\pi G}{3}\rho_{\mathrm{c}}(t), \\
\rho_{\mathrm{c}}(t) &= \frac{3H(t)^2}{8\pi G}.
\end{aligned}
\tag{1.9}
$$

We can rewrite Eq. 1.8 by normalising $\rho(t)$ by the present-day critical density $\rho_{\mathrm{c},0} = \rho_{\mathrm{c}}(t = t_0)$:

$$
\begin{aligned}
H(t)^2 &= \frac{8\pi G}{3}(\rho_{\mathrm{m},0}a(t)^{-3} + \rho_{\mathrm{r},0}a(t)^{-4} + \rho_{\Lambda}) - kc^2a(t)^{-2}, \\
H(t)^2 &= \frac{8\pi G}{3H_0^2}H_0^2(\rho_{\mathrm{m},0}a(t)^{-3} + \rho_{\mathrm{r},0}a(t)^{-4} + \rho_{\Lambda}) - kc^2a(t)^{-2}, \\
H(t)^2 &= \frac{1}{\rho_{\mathrm{c},0}}H_0^2(\rho_{\mathrm{m},0}a(t)^{-3} + \rho_{\mathrm{r},0}a(t)^{-4} + \rho_{\Lambda}) - kc^2a(t)^{-2}, \\
H(t)^2 &= H_0^2\Big(\frac{\rho_{\mathrm{m},0}}{\rho_{\mathrm{c},0}}a(t)^{-3} + \frac{\rho_{\mathrm{r},0}}{\rho_{\mathrm{c},0}}a(t)^{-4} + \frac{\rho_{\Lambda}}{\rho_{\mathrm{c},0}}\Big) - kc^2a(t)^{-2}, \\
H(t)^2 &= H_0^2\big(\Omega_{\mathrm{m},0}a(t)^{-3} + \Omega_{\mathrm{r},0}a(t)^{-4} + \Omega_{\Lambda,0} + \Omega_{\mathrm{k},0}a(t)^{-2}\big),
\end{aligned}
\tag{1.10}
$$

where $\Omega_{\mathrm{m},0}$, $\Omega_{\mathrm{r},0}$, $\Omega_{\Lambda,0}$ and $\Omega_{\mathrm{k},0}$ are the present-day matter, radiation, dark energy and curvature density parameters respectively. The current consensus is that the Universe is largely flat i.e. $k \approx 0$, $\Omega_{\mathrm{k},0} \approx 0$ and $\Omega_{\mathrm{m},0} + \Omega_{\mathrm{r},0} + \Omega_{\Lambda,0} \approx 1$. Thus we can consider these density parameters as present-day fractions of the total density

of the Universe. We can also introduce $\Omega_{\rm DM,0}$ and $\Omega_{\rm b,0}$ which are the dark matter and baryonic density parameters respectively (where $\Omega_{\rm m,0} = \Omega_{\rm DM,0} + \Omega_{\rm b,0}$).

The final two parameters to introduce are the scalar power-law index $n_{\rm s}$ and the amplitude of the linear power spectrum σ_8. As previously mentioned in §1.1, the CMB is largely homogeneous in temperature aside from some minute anisotropies. These anisotropies are the framework by which stars and galaxies would eventually form. The primordial power spectrum describing these anisotropies is described by perturbations in density due to curvature ($\mathcal{R}$) (Peiris et al., 2003; Clesse, 2015). Inflation models (see Martin et al. (2014) for a review) predict that the dimensionless primordial power spectrum $\Delta^2_{\mathcal{R}}(k)$ can be described as a function of wavenumber k approximately by a power law (Peiris et al., 2003):

$$\begin{aligned} \Delta^2_{\mathcal{R}}(k) &= \frac{k^3}{2\pi^2}\langle|\mathcal{R}_k|^2\rangle \propto k^{n_{\rm s}-1}, \\ n_{\rm s}(k_0) - 1 &= \left.\frac{d\ln\Delta^2_{\mathcal{R}}(k)}{d\ln k}\right|_{k=k_0}, \end{aligned} \tag{1.11}$$

where $n_{\rm s}$ is the scalar power-law index and k_0 is a specific wavenumber scale. Eq. 1.11 is from §3.2.1 of Peiris et al. (2003) where $k_0 = 0.002\,{\rm cMpc}^{-1}$. The current consensus is that $n_{\rm s} < 1$ and thus the primordial power spectrum deviates from scale invariance.

The amplitude of the linear power spectrum σ_8 dictates the distribution of matter at a particular scale ($R = 8\,{\rm cMpc/h}$)[1] and linearly extrapolated to $z = 0$ (van den Bosch et al., 2013). More generally, the variance of a matter density field at some redshift z and smoothed on some scale R (i.e. we are only interested in fluctuations below this scale) is given as:

$$\begin{aligned} \sigma^2(z,R) &= \frac{1}{2\pi^2}\int_0^\infty k^2\,P(z,k)\,\tilde{W}^2(kR)\,dk, \\ \tilde{W}(kR) &= \frac{3}{(kR)^3}\left[\sin(kR) - (kR)\cos(kR)\right], \end{aligned} \tag{1.12}$$

where $P(z,k)$ is the matter power spectrum (dimensions of length^3) and $\tilde{W}(kR)$ is the Top Hat filter. This value of R was chosen such that $\sigma_8 \approx 1$.

Many experiments have been completed for over 20 years to determine the values of these parameters by analysing the CMB (Spergel et al., 2003; Hinshaw et al., 2013; Planck Collaboration et al., 2014, 2020) and galaxy clustering (Perlmutter et al., 1999; Riess et al., 2004, 2011, 2016). There is still tension between these methods in determining the Hubble constant H_0 and $\Omega_{\rm m,0}$ in particular (Efstathiou, 2025). We summarise the parameter values deduced by Planck13 in Table 1.1 (see leftmost column of Table 2 in Planck Collaboration et al. (2014)). Note that the parameter values used in §2 and §3 deviate slightly from the Planck13 cosmology. We exclude baryons and radiation in §2 for our dark-matter-only simulations; we

[1] h is the dimensionless Hubble constant defined as ${\rm h} = H_0/(100\,{\rm km\,s^{-1}\,Mpc})$.

mimic the cosmology from Dijkstra et al. (2014) in §3.

Parameter	Value
h	0.6711
$\Omega_{\mathrm{DM},0}$	0.2671
$\Omega_{\mathrm{b},0}$	0.0490
$\Omega_{\Lambda,0}$	0.6825
n_{s}	0.9624
σ_8	0.8344

Table 1.1: Parameter values from Planck13

1.3 Hierarchical Structure Formation

1.3.1 Dark Matter Halo Formation

Here we briefly describe how baryons and dark matter contribute to galaxy formation. We consider a galaxy of baryons (made up of stars, gas and dust) to be contained within a spherical dark matter halo. The CDM model implies that structure forms in a bottom-up hierarchical fashion: low-mass dark matter halos form at high redshift, they merge together to form more massive halos and the most massive halos only exist at low redshift (Binney & Tremaine, 2008). Early in the evolution of the Universe and prior to the formation of atoms (decoupling and recombination), free charged particles are scattered by photons i.e. Thomson scattering. Photons scatter both electrons and protons but due to their much lower mass, electrons experience a greater change in their momentum. Protons are then dragged by these electrons due to Coulombic attraction. While this occurs for baryons, dark matter is unaffected by electromagnetic radiation. This leaves dark matter free to collapse under gravity, producing gravitational potential wells. Both baryons and photons then fall into these potential wells (i.e. dark matter halos), the baryons collapse and later form galaxies (White & Rees, 1978; Weinberg et al., 2008).

According to the spherical collapse model (Binney & Tremaine, 2008), the halo initially expands due to being coupled to the Hubble flow until it reaches a maximum radius (called the turn-around radius) and subsequently begins to collapse until it reaches a physical radius $r_{\mathrm{vir}}(z)$ i.e. until virialisation is achieved. The virial mass $M_{\mathrm{vir}}(z)$ of such a halo is given as:

$$M_{\mathrm{vir}} = \frac{4\pi}{3} r_{\mathrm{vir}}^3 \Delta_{\mathrm{c}}(z) \rho_{\mathrm{c}}(z), \tag{1.13}$$

where $\Delta_{\mathrm{c}}(z)\rho_{\mathrm{c}}(z)$ is the average density contained within a sphere of mass M_{vir}

and radius $r_{\rm vir}$ (Bryan & Norman, 1998). At high z (i.e. the matter-dominated era of the Universe), $\rho_{\rm c}(z) \approx \rho_{\rm m}(z)$. By applying the virial theorem and assuming a flat universe, we can express $\Delta_{\rm c}(z)$ as:

$$\begin{aligned} \Delta_{\rm c}(x) &= 18\pi^2 + 82x - 39x^2, \\ x(z) &= \frac{\Omega_{\rm m,0}(1+z)^3}{\Omega_{\rm m,0}(1+z)^3 + \Omega_{\Lambda,0}} - 1. \end{aligned} \tag{1.14}$$

For high z, $x \to 0$ and $\Delta_{\rm c} \to 18\pi^2 \approx 200$. This overdensity is key when identifying halos in dark matter-only simulations, later seen in §2. Also in the high-z limit, the Hubble parameter can be approximated as $H(z) \approx H_0\, \Omega_{\rm m,0}^{1/2}(1+z)^{3/2}$. Using these approximations, we can express the physical virial radius as:

$$\begin{aligned} r_{\rm vir}(z, M) = (7.84 \times 10^{-4}) &\Big(\frac{M}{10^8\, {\rm h^{-1}M_\odot}}\Big)^{1/3} \Omega_{\rm m,0}^{-1/3} \\ &\times \Big(\frac{1+z}{10}\Big)^{-1} {\rm Mpc/h}. \end{aligned} \tag{1.15}$$

Additionally, we can derive a relationship between the virial mass $M_{\rm vir}$ and the virial temperature $T_{\rm vir}$ of the gas within the halo. By assuming an isothermal distribution, the density ρ at a given physical radius r from the halo centre is:

$$\rho(r) = \frac{\sigma^2}{2\pi G r^2}, \tag{1.16}$$

where σ is the velocity dispersion of the particles within the halo. By integrating Eq. 1.16 over a sphere of radius $r_{\rm vir}$, we can find $r_{\rm vir} = r_{\rm vir}(\sigma)$. By substituting this into Eq. 1.13, we find:

$$\sigma = M_{\rm vir}^{1/3} \frac{H(z)^{1/3} \Delta_{\rm c}^{1/6}(z) G^{1/3}}{16^{1/6}}. \tag{1.17}$$

Again by assuming an isothermal distribution, we can relate this to the temperature T of the gas as:

$$T = \frac{\mu m_p \sigma^2}{k_{\rm B}}, \tag{1.18}$$

where μ is the mean molecular weight, $m_{\rm p}$ is the proton mass and $k_{\rm B}$ is the Boltzmann constant. Finally we can substitute σ from Eq. 1.17 into Eq. 1.18 to find an expression between $M_{\rm vir}$ and $T_{\rm vir}$:

$$T_{\rm vir} = \frac{G M_{\rm vir}^{2/3} \mu m_{\rm p}}{2 k_{\rm B}} \frac{H(z)^{2/3} \Delta_c^{1/3}(z)}{(2G)^{1/3}}. \tag{1.19}$$

Later, in §3, we consider supermassive stars (SMSs) as a formation pathway for intermediate-mass black holes (IMBHs), which act as heavy seeds for supermassive black holes (SMBHs). In order to form a SMS within a halo, the gas must cool via atomic hydrogen only where $T_{\rm vir} \approx 10^4$ K. If we set $T_{\rm vir} \approx 10^4$ K and take the

high-z approximation ($H(z) \approx H_0\,\Omega_{\rm m,0}^{1/2}(1+z)^{3/2}$), we find:

$$M_{\rm vir} \approx (4 \times 10^7\,{\rm M}_\odot)\left(\frac{1+z}{11}\right)^{-3/2}. \tag{1.20}$$

This is the minimum halo mass required for cooling via atomic hydrogen i.e. the atomic-cooling limit (Regan & Haehnelt, 2009; Fernandez et al., 2014). In §3, we use both Eq. 1.15 and 1.20 to compute the IMBH number density.

1.3.2 Large-Scale Structure

Later in §2, we investigate how the number density of dark matter halos varies with mass M and redshift z by comparing simulation results with both analytic and semi-analytic models. In this subsection, we describe the large-scale structure of the Universe due to the clustering of dark matter and galaxies as observed in both galaxy surveys and large-scale simulations, illustrating the power of these simulations to study the high-z Universe.

As stated in §1.2, the isotropy of the Universe is best realised on very large scales i.e. hundreds of Mpc. Due to the influence of gravity, dark matter clumps together in knots, filaments and sheets while leaving extremely under-dense regions in between called voids. Baryons are gravitationally bound to this framework and later form galaxies within dark matter halos. This entire structure is known as the Cosmic Web. However since we are in the dark energy-dominated era of the Universe's evolution, the accelerated expansion of the Universe will continue to work against this clustering by pushing distant galaxies further apart.

The first galaxy redshift survey of the local Universe was completed by the Centre for Astrophysics | Harvard & Smithsonian in Massachusetts, USA from 1977 to 1982 (Huchra et al., 1983), later referred to as CfA. Here, the radial velocities of 2401 galaxies were measured. This was followed up by another redshift survey later known as CfA2 (Geller & Huchra, 1989) which ran from 1984 to 1995 and measured the redshifts of 18,000 galaxies. This survey included the discovery of a filament of galaxies known as the CfA2 Great Wall, measuring $\sim$ 600 light-years in length (see central sector of Figure 1.6).

From 1997 to 2002, the Australian Astronomical Observatory conducted the Two-Degree Field Galaxy Redshift Survey (2dF-GRS) using the Anglo-Australian Telescope (Colless et al., 2001), covering 1500 deg^2 of the sky. The spectra and redshifts of over 200,000 galaxies were measured with the most distant at $z < 0.3$ and $\sim$ 600 Mpc away (Colless et al., 2003). Figure 1.2 shows the galaxy distribution of the completed survey with present-day Earth at the centre of the figure.

The more ambitious Sloan Digital Sky Survey (SDSS) began operations in 2000 (Gunn et al., 2006) from the Apache Point Observatory in New Mexico,

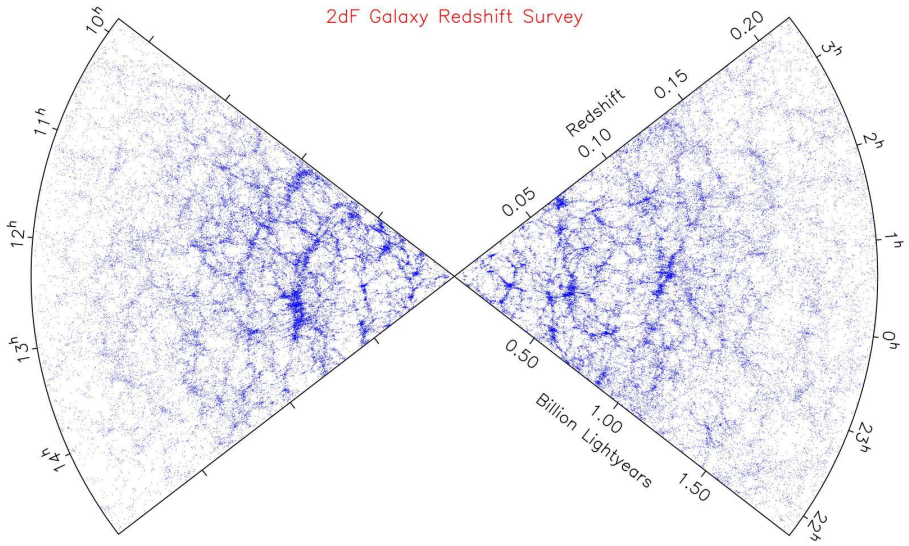

Figure 1.2: The galaxy distribution from the completed 2dF-GRS. Taken from Figure 2 of Colless et al. (2003).

USA and is still releasing data today with the most recent data release in 2023 (Almeida et al., 2023). Initially (SDSS-I and SDSS-II phases) 8000 deg^2 were mapped and the spectra of over 800,000 galaxies and 100,000 quasars (see §1.4) were determined. This includes a filament called the Sloan Great Wall which measures 1.37 billion light-years in length (see topmost sector of Figure 1.6). Figure 1.3 shows the galaxy distribution up to $z < 0.16$ with present-day Earth at the centre. Dust from the Milky Way hinders our ability to survey some of the sky so these blank regions were not surveyed. This was expanded in the SDSS-III phase of the operation with the survey covering 14,555 deg^2 of the sky (Aihara et al., 2011). The spectra of many $z \sim 6$ quasars were determined using this survey (Jiang et al., 2016). Both Figures 1.2 and 1.3 clearly show the shape of the Cosmic Web, with galaxies clustering in knots and filaments.

To understand the evolution of the Cosmic Web, several powerful cosmological simulations have been completed with the output still being analysed today. In 2005, the Virgo Consortium completed the Millennium Run simulations (Springel et al., 2005), a suite of dark matter-only cosmological simulations (run using the cosmological code `GADGET2` (Springel et al., 2001; Springel, 2005)) which tracked the formation of dark matter halos. They began at $z = 127$, finished at $z = 0$ and had a volume of $V = (500 \text{ cMpc/h})^3$ with $N = 2160^3$ particles. Croton et al. (2006) applied a semi-analytic model of galaxy evolution and formation to the dark matter halo merger tree structure while post-processing the initial Millennium Run output. Figure 1.4 shows the distribution of galaxies from a slice of this simulation volume.

Following the Millennium Run, many more simulation projects have been

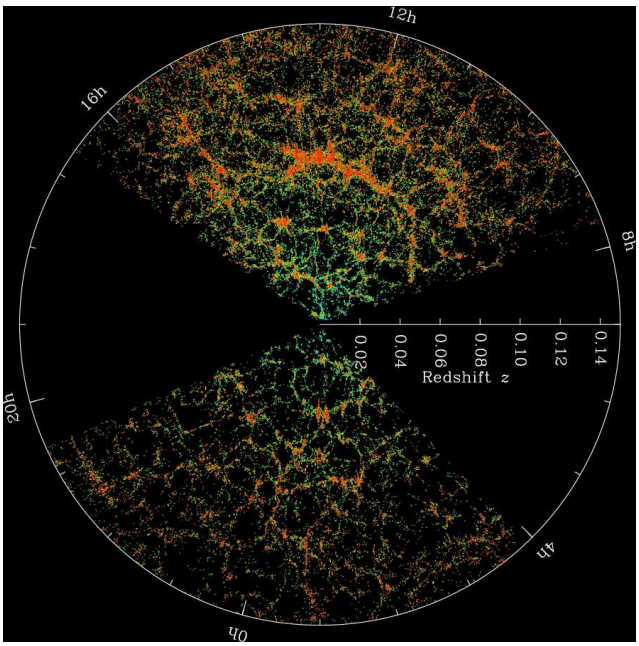

Figure 1.3: Taken from the press release SDSS Collaboration (2008), following the completion of SDSS-II. Each dot represents a galaxy, with redder galaxies being made up of older stars.

completed. These include but are not limited to EAGLE (Schaye et al., 2015), HorizonAGN (Dubois et al., 2014), MassiveBlack-II (Khandai et al., 2015) and Romulus25 (Tremmel et al., 2017). We discuss in detail below two well-regarded simulation projects: Illustris and IllustrisTNG. The first simulations of the Illustris project were completed in 2013 (Vogelsberger et al., 2014) using the hydrodynamic `AREPO` code (Springel, 2010). These simulations all had a volume of $V = (75$ cMpc/h$)^3$, began at $z = 127$, ended at $z = 0$ and varied in mass resolution, with the highest resolution consisting of 1820^3 dark matter particles and the same number of hydrodynamic cells and Monte Carlo tracers. These simulations tracked the evolution of both dark matter and baryonic structures, accounting for gas cooling, photo-ionisation, star formation and both stellar and black hole feedback.

These initial simulations were succeeded by a follow-up project called IllustrisTNG which consists of three different simulation volumes of $V = (302.6$ cMpc$)^3$ (TNG300), (110.7 cMpc$)^3$ (TNG100) (Springel et al., 2017; Nelson et al., 2018; Marinacci et al., 2018; Naiman et al., 2018; Pillepich et al., 2018) and (51.7 cMpc$)^3$ (TNG50) (Pillepich et al., 2019; Nelson et al., 2019a). The highest resolution of TNG300 consists of 2500^3 dark matter particles and the same number of gas and tracer particles. Like their predecessors, these simulations began at $z = 127$ and ended at $z = 0$. They improve on the original Illustris simulations by updating their active galactic nuclei (AGN) feedback model, including a new parameterisation of galactic winds and including magnetic fields based on ideal magneto-hydrodynamics. The TNG300 simulation in particular has been used to demonstrate the large-scale structure of the Universe, seen in Figure 1.5.

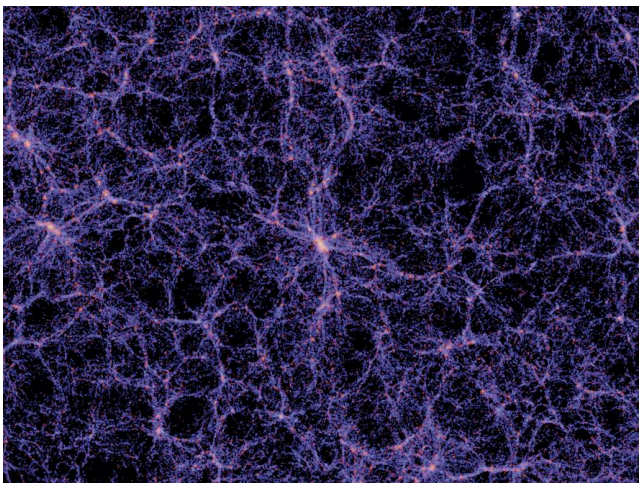

Figure 1.4: The distribution of light from galaxies in a 330 cMpc/h × 280 cMpc/h slice from the Millennium Run, integrated over 15 cMpc/h, the intensity indicating surface brightness. Taken from Figure 1 (bottom panel) of Croton et al. (2006).

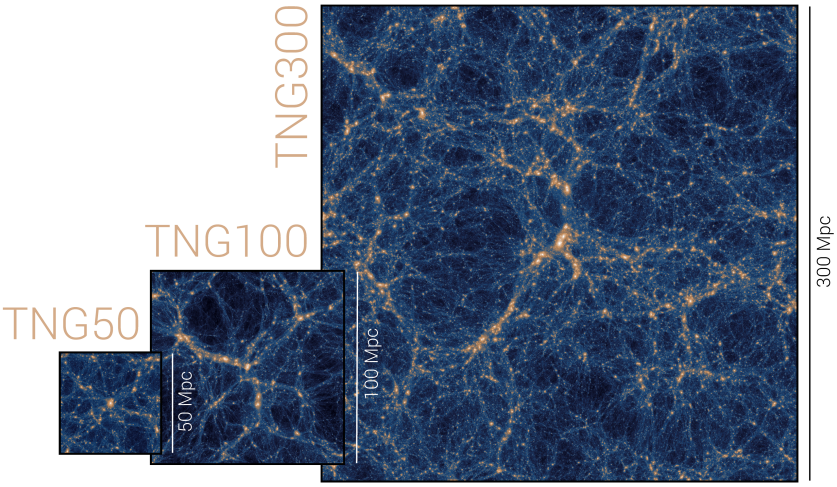

Figure 1.5: A comparison of the dark matter large-scale structure shown in the three IllustrisTNG boxes, taken from Figure 1 of Nelson et al. (2019b).

These cosmological simulations compare well with observations of the large-scale structure in the local Universe as shown in Figure 1.6 which compares sections of data from CfA2, 2dF-GRS and SDSS as well as mock data from the Millennium simulation. Since the Cosmic Web is constructed by gravity acting on very large scales, dark matter-only simulations such as Millennium are incredibly valuable for probing this large-scale structure of the high-redshift Universe. While the inclusion of baryonic processes would be more physical, this would result in effects acting on smaller scales, so dark matter-only simulations still remain a useful approximation when testing theories of large-scale structure.

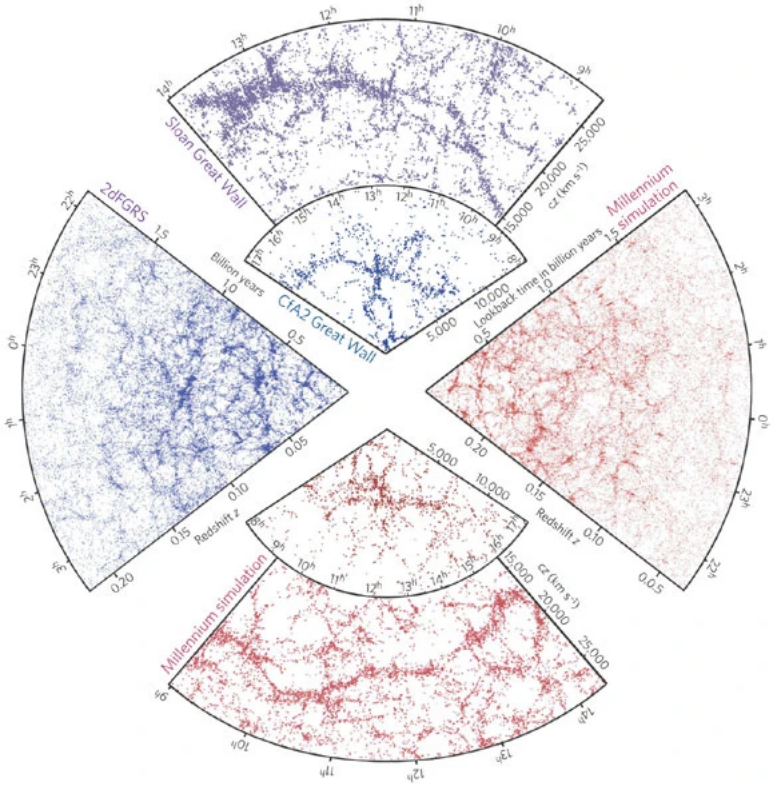

Figure 1.6: A comparison of large-scale structure demonstrated by data from CfA2, 2dF-GRS and SDSS and mock data from Millennium. Taken from Figure 1 of Springel et al. (2006).

1.4 Quasars

Objects in the high-z Universe generally have very low fluxes due to their great distances from us and this is the main challenge with observing such objects. Quasi-stellar objects (or quasars) act as our guiding light to the high-z Universe due to their incredible luminosities as some of the brightest objects in the Universe. As described in the previous section, hundreds of quasars at $z \gtrsim 6$ have been discovered in the last 20 years (Fan et al., 2006, 2023), many found as part of the SDSS. In this section, we describe their properties and what questions their presence raises about the early Universe.

A quasar is the most luminous type of active galactic nucleus (AGN) and among the most luminous objects in the Universe (Wolf et al., 2024). An AGN resides at the centre of a galaxy with a luminosity so great it cannot be accounted for by only the stellar luminosity of the galaxy. The current consensus is that a supermassive black hole (SMBH) would be accreting matter at the centre of this galaxy (see Figure 1.7). As matter is accreted, it heats up and emits radiation across the electromagnetic spectrum (Shields, 1999). Quasars were first discovered in the late 1950s and early 1960s with one of the first identified being 3C 273 with

$z = 0.158$ and an estimated bolometric luminosity[2] of $L_{\text{bol}} \sim 10^{47}$ erg/s (Schmidt, 1963; Greenstein & Schmidt, 1964; Landt et al., 2011; Thorne et al., 2025).

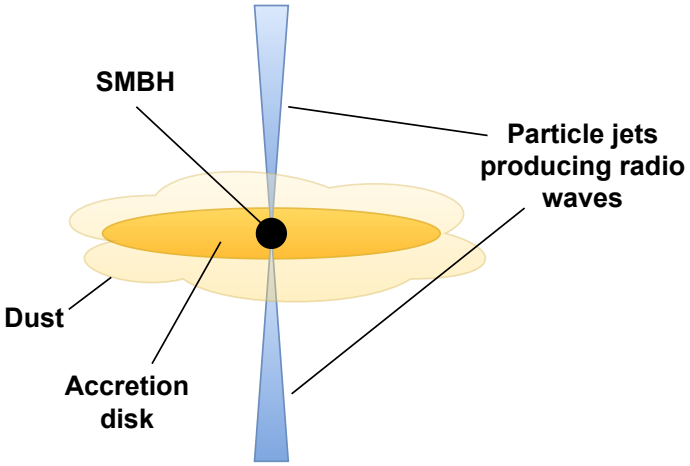

Figure 1.7: A quasar consisting of a supermassive black hole (SMBH) accreting matter and producing jets of relativistic particles which emit radio waves.

At time of writing, the quasar SMSS J215728.21-260215.1 is one of the most luminous quasars known with a bolometric luminosity of $L_{\text{bol}} = 2.66 \times 10^{48}$ erg/s, $z = 4.75$ and was discovered by Wolf et al. (2018) at the Australian National University's Siding Spring Observatory.

Quasars act as an incredibly useful probe into the first Gyr of the Universe, particularly the epoch of reionization. The most distant quasar currently known is UHZ-1 at $z \sim 10.3$ and $L_{\text{bol}} \sim 5 \times 10^{45}$ erg/s by the Chandra X-ray Observatory (Bogdán et al., 2024; Natarajan et al., 2024). Quasars were more common in the past ($z \sim 1 - 2$) (Richards et al., 2006) than in the local Universe ($z \sim 0$). Once a quasar has accreted much of the surrounding matter, it no longer produces this high level of radiation and its luminosity is more comparable to galaxies in the local Universe.

One observational feature of quasars is broadening of emission and absorption lines. The atoms constituting the gas of the accretion disk absorb and emit photons of distinct wavelengths, leading to these absorption and emission lines being a feature of the quasar spectrum. The atoms also move with large velocities, causing the photon wavelengths to be Doppler-shifted (Carroll & Ostlie, 2017). As a result, the lines at these wavelengths have a broader peak (see Figure 1.8).

In order to estimate the mass of the SMBH powering a quasar, we can use the full-width half maximum (FWHM) and luminosity associated with a specific emission line (Kaspi et al., 2000; Greene & Ho, 2004). There exist many fits using different spectral lines e.g.

[2]Bolometric luminosity refers to total luminosity from all electromagnetic wavelengths.

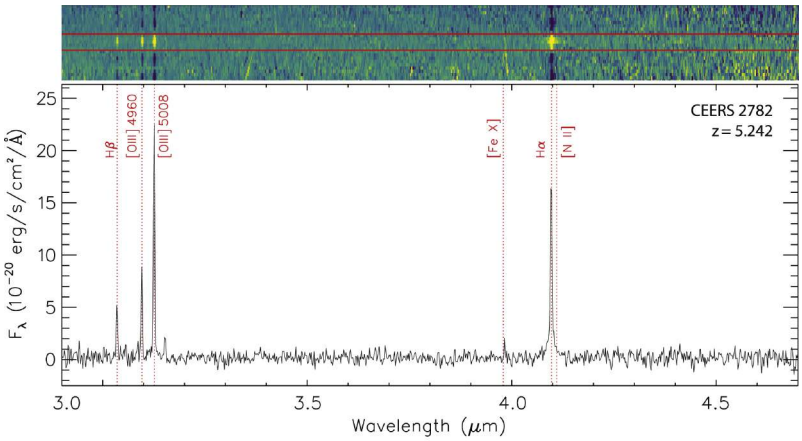

Figure 1.8: The spectrum of the quasar CEERS 2782, taken from Figure 2 (top panel) of Kocevski et al. (2023).

$$\log_{10}\left(\frac{M_{\rm BH}}{\rm M_\odot}\right) = \log_{10}\epsilon + 6.57 + 0.47\log_{10}\left(\frac{L_{\rm H\alpha}}{10^{42}\,\rm erg/s}\right) + 2.06\log_{10}\left(\frac{\rm FWHM_{H\alpha}}{10^3\,\rm km/s}\right), \tag{1.21}$$

where the scale factor is set to $\epsilon = 1.075$, $L_{\rm H\alpha}$ is the luminosity associated with the Hα line and $\rm FWHM_{H\alpha}$ is the velocity associated with this peak broadening (Reines & Volonteri, 2015). This illustrates that broader peaks and higher luminosities indicate greater SMBH masses.

Using fits like Eq. 1.21 for known quasars, we can estimate that the SMBHs powering quasars can have masses $M_{\rm BH} \gtrsim 10^8\,\rm M_\odot$. This holds even for quasars detected at $z \gtrsim 6$ when the Universe was less than 1 Gyr old. This raises two important questions about the high-redshift Universe: how were these SMBHs seeded and how do they grow to this mass in a relatively short amount of time? In the next section, we detail how the new era of observational astrophysics launched by the James Webb Space Telescope (JWST) hopes to answer these questions.

1.5 JWST

In this section, we briefly describe the James Webb Space Telescope (JWST), what it has already taught us about the high-redshift Universe and what questions the data raise. JWST is a space-based infrared telescope and to date it is the largest telescope placed in space (Gardner et al., 2006). JWST acts as a successor to the Hubble Space Telescope (HST) and such a telescope had been planned since the 1990s (Brown, 1996). The project is a collaboration between NASA, ESA and the Canadian Space Agency with a mission span of 5-10 years but with the potential to run for 20 years or longer (Gardner et al., 2023). The telescope was launched into space from French Guiana on Christmas Day 2021 and the first

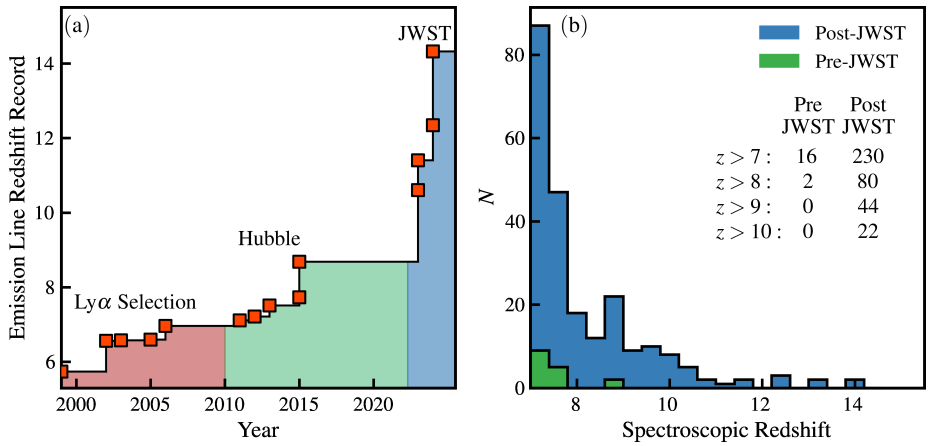

Figure 1.9: Recent high-redshift galaxy detections by JWST compared to older telescopes, taken from Figure 1 of Stark et al. (2025).

images were released in July 2022.

Some of its goals include observing the first galaxies and determining how these galaxies form and evolve. Due to the expansion of the Universe, the UV light emitted by these early galaxies has been redshifted to infrared wavelengths by the time it reaches present-day Earth. JWST has a wavelength coverage of 600 to 28,500 nm (orange visible light to mid-infrared) for this purpose, whereas HST covers 900 to 2,500 nm (near-infrared). Additionally, it boasts incredible sensitivity by detecting objects 10-100 times fainter than HST and with six times the light-gathering power (NASA, 2025). Another goal of JWST is to observe the first episodes of star formation, thought to occur at $z = 15$ to 30. At time of writing, the most distant galaxy observed by JWST is JADES-GS-z14-0 with a spectroscopically-confirmed redshift of $z = 14.32$ (Carniani et al., 2024). Figure 1.9 shows how the high-redshift detection threshold has continued to be raised, largely thanks to JWST.

In the rest of this section, we describe some of the findings of JWST and how they relate to the growth of SMBHs in the early Universe.

1.5.1 Low-Luminosity Active Galactic Nuclei (AGNs)

Prior to the launch of JWST, our observational knowledge of AGNs was limited by what older telescopes could see i.e. the brightest AGNs unobscured along our line of sight (Stark et al., 2025). With JWST being capable of detecting objects up to 100 times fainter than what HST could detect, we have seen a widening of the luminosity range of high-redshift AGNs detected since 2022. On the lower end of this, we have faint AGN, so-called for both their low fluxes due to their great distances from us and their low intrinsic luminosities. As mentioned in §1.4, the origin of SMBHs remains an open question. The recent observations of such low-luminosity AGN (with lower central black hole masses) may help shed light

on their seeding and evolution.

In 2023, 10 faint AGNs with broad Hα emission lines were found using JWST data at $z = 4.016$ to 6.936 and with estimated central black hole masses $M_{\mathrm{BH}} \sim 10^6\,\mathrm{M}_\odot$ to $10^8\,\mathrm{M}_\odot$ and bolometric luminosities $L_{\mathrm{bol}} \sim 10^{44}$ to 10^{46} erg/s (Harikane et al., 2023). These particular AGNs have lower values of M_{BH} and L_{bol} than quasars found previously at similar redshifts by ground-based telescopes. Two of these AGNs show red spectral energy distributions (SEDs) and large dust attenuation, indicating that they are dusty red AGNs. More local AGNs ($z \sim 0$) with similar mass ranges tend to have lower bolometric luminosities than those found in this sample - this may be due to selection bias by Harikane et al. (2023).

1.5.2 Little Red Dots (LRDs)

Another recent discovery by JWST are Little Red Dots (LRDs) (Matthee et al., 2024). These are high-redshift ($z \sim 4 - 8$) galaxies that are very compact (with a supposed AGN region $< 100\,\mathrm{pc}$ (Lambrides et al., 2024)) with broad Hα emission lines and predominantly red spectra. Matthee et al. (2024) identified an initial sample of 20 such objects with $L_{\mathrm{H}\alpha,\mathrm{broad}} > 2 \times 10^{42}\,\mathrm{erg/s}$ and $\mathrm{FWHM}_{\mathrm{H}\alpha,\mathrm{broad}} > 1000\,\mathrm{km/s}$.

The broad Hα emission lines suggest that LRDs are a population of high-redshift AGNs powered by an accreting SMBH. Given this assumption, we can estimate the black hole mass using Eq. 1.21. The bolometric luminosity can be estimated as:

$$\frac{L_{\mathrm{bol}}}{10^{44}\,\mathrm{erg/s}} = 10.33 \left(\frac{L_{\mathrm{H}\alpha,\mathrm{broad}}}{5.25 \times 10^{42}\,\mathrm{erg/s}} \right)^{\frac{1}{1.157}}, \tag{1.22}$$

following the approximation used by Harikane et al. (2023). For the sample found by Matthee et al. (2024), the estimated black hole masses are $M_{\mathrm{BH}} = 10^{6.9} - 10^{8.6}\,\mathrm{M}_\odot$ and the estimated bolometric luminosities are $L_{\mathrm{bol}} = 10^{44.7} - 10^{45.8}\,\mathrm{erg/s}$.

Bizarrely, these LRDs generally are not detected in X-ray observations, leading some to believe that they are not AGNs at all. The Hα emission lines may instead be due to galactic outflows from supernovae and/or star formation (Ananna et al., 2024). Kocevski et al. (2025) found a sample of 341 LRDs with $z \sim 2 - 11$ and only two were detected in X-ray observations. In the initial sample by Matthee et al. (2024), the X-ray non-detections may be due to X-ray limits with the surveys chosen to create the sample. It has also been suggested that the X-ray radiation has been absorbed by clouds with large column density (Maiolino et al., 2025).

1.5.3 Overmassive Black Holes

There have been many empirical relationships established between a black hole mass $M_{\rm BH}$ and its host galaxy properties e.g. galaxy bulge luminosity, velocity dispersion of stars nearest to the black hole and galaxy stellar mass. Locally ($z \sim 0$) these relationships can be expressed as power laws. Kormendy & Ho (2013) describe the relationships between $M_{\rm BH}$ and near-infrared bulge luminosity $L_{\rm K,\,bulge}$ and between $M_{\rm BH}$ and velocity dispersion $\sigma_{\rm e}$ (inside the effective radius that encompasses half the light of the bulge) as:

$$\begin{aligned} \frac{M_{\rm BH}}{10^9\,{\rm M}_\odot} &= (0.542^{+0.069}_{-0.061}) \left(\frac{L_{\rm K,\,bulge}}{10^{11}\,{\rm L}_{\rm K,\odot}} \right)^{1.21\pm0.09}, \\ \frac{M_{\rm BH}}{10^9\,{\rm M}_\odot} &= (0.309^{+0.037}_{-0.033}) \left(\frac{\sigma_{\rm e}}{200\,{\rm km/s}} \right)^{4.38\pm0.29}. \end{aligned} \tag{1.23}$$

Figure 1.10 shows how $M_{\rm BH}$ positively correlates with K-band bulge luminosity $L_{\rm K,\,bulge}$ (left panel) and velocity dispersion $\sigma_{\rm e}$ (right panel) with red dots referring to classical bulges and the black dots referring to elliptical galaxies. The empirical fits described in Eq. 1.23 are based on a symmetric, least-squares fit by Tremaine et al. (2002).

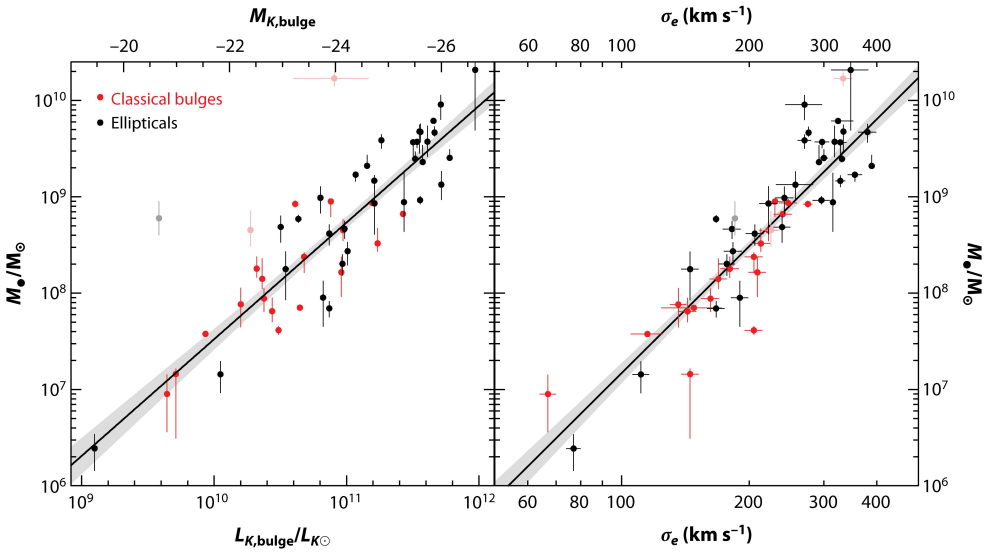

Figure 1.10: Black hole mass vs. K-band bulge luminosity (left panel) and velocity dispersion (right panel) with 1σ range of the fits (grey shading), taken from Figure 17 of Kormendy & Ho (2013).

Reines & Volonteri (2015) provide an empirical fit for $M_{\rm BH}$ and $M_{\rm stellar}$ in Figure 1.11. The colour of a marker indicates its galaxy morphology: E referring to ellipticals (brown), S0 referring to lenticulars (yellow) and Sab and Scd referring to types of spiral galaxies (dark green and light green respectively) (Carroll & Ostlie, 2017). The red line indicates the fit using AGNs and the blue line indicates the fit using classical bulges and elliptical galaxies that host dynamically-detected

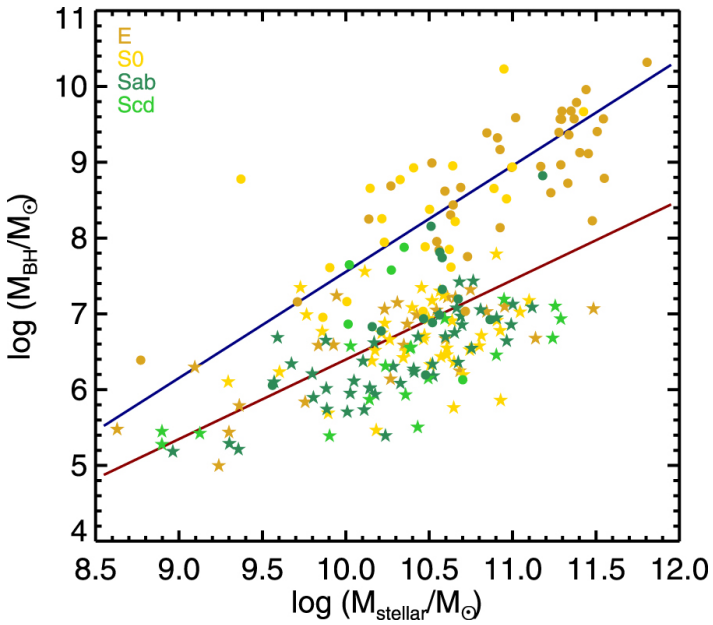

Figure 1.11: Black hole mass vs. stellar mass, taken from Figure 12 of Reines & Volonteri (2015). The markers describe E (ellipticals) (brown), S0 (lenticulars) (yellow), and spiral galaxies Sab (dark green) and Scd (light green). The stars refer to AGN while the dots refer to dynamically-detected black holes. The red line indicates the fit using AGNs and the blue line indicates the fit using dynamically-detected black holes.

black holes. Both lines describe power laws of the form:

$$\log_{10}(M_{\rm BH}/{\rm M}_\odot) = \alpha + \beta \log_{10}(M_{\rm stellar}/10^{11}\,{\rm M}_\odot), \tag{1.24}$$

where $\alpha = 7.45\pm0.08$, $\beta = 1.05\pm0.11$ (red line) and $\alpha = 8.95\pm0.09$, $\beta = 1.40\pm0.21$ (blue line).

These correlations suggest that black holes and their host galaxies co-evolve and regulate the growth of one another. This co-evolution is thought to be influenced by (1) the black hole feeding from the host galaxy, (2) galaxy (and black hole) mergers growing both the black hole and its host galaxy and (3) black hole feedback inhibiting star formation by preventing gas fragmentation.

However, recently it has been shown using JWST galaxies that this relatively simple empirical relationship does not hold at higher redshifts. Pacucci et al. (2023) showed that JWST black holes at $z = 4 - 7$ can be 10-100 times larger than their local counterparts for a given host galaxy mass. Figure 1.12 illustrates how these JWST galaxies deviate from the local relationship derived by Reines & Volonteri (2015). The blue markers refer to the sample of 8 galaxies found by Harikane et al. (2023); the green markers refer to the 12 galaxies found by Maiolino et al. (2024); the purple marker refers to the single galaxy found by Übler et al. (2023). The error bars refer to 1σ uncertainty in mass measurement. The blue line refers to the local relationship from Reines & Volonteri (2015) using

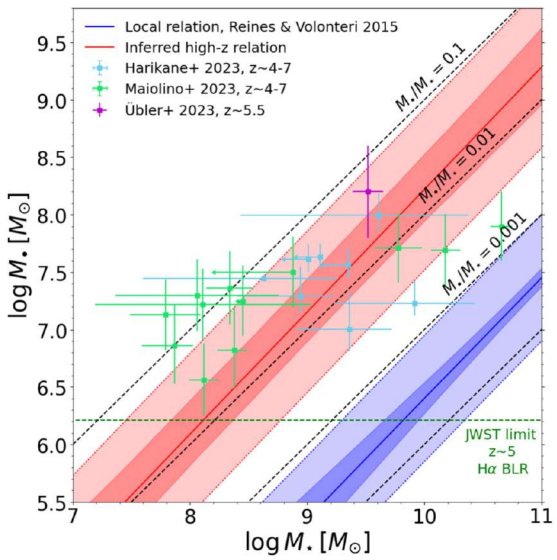

Figure 1.12: Black hole mass vs. host galaxy stellar mass, taken from Figure 2 (left) of Pacucci et al. (2023). The blue line refers to the local relationship from Reines & Volonteri (2015) using a sample of AGNs. The red line refers to the high-z fit from Pacucci et al. (2023). The dark and light shading refers to 1σ uncertainty and a root-mean-square deviation respectively. The green horizontal dashed line refers to the minimum black hole mass that could be detected by JWST at $z \sim 5.5$ (the median redshift of the sample).

a sample of AGNs (see red line from Figure 1.11). The red line refers to a high-z fit described as:

$$\log_{10}(M_{\rm BH}/{\rm M}_\odot) = \alpha + \beta \log_{10}(M_{\rm stellar}/{\rm M}_\odot), \tag{1.25}$$

where $\alpha = -2.43 \pm 0.83$, $\beta = 1.06 \pm 0.09$.

This suggests that at high-z, the black hole grows faster than the host galaxy. It is important to note that these relationships are empirical and need not necessarily hold at high redshift. The complex physical processes that dictate both black hole and galaxy growth are less well understood at high redshift. Nonetheless, if these black hole mass measurements are accurate, we must ask once again: how did the black holes grow to this magnitude in less than 1 Gyr? This high-z relation suggests that this growth is not strongly dependent on the growth of the host galaxy.

1.5.4 Black Hole Seeding

Here we describe some potential seeding mechanisms for these SMBHs. First, we define the black hole mass spectrum as understood at time of writing. A star at the end of its life may become a white dwarf, neutron star or a stellar black hole ($M_{\rm BH} \sim 10^1 - 10^2\,{\rm M}_\odot$). The final state depends on the final mass of the star. The progenitor stellar mass range required to form a neutron star is approximately

$M_* = 10 - 25\,\mathrm{M}_\odot$. The exact mass cut-off separating the most massive neutron stars from the least massive stellar black holes is still to be determined but is thought to be $\sim 2\,\mathrm{M}_\odot$ (Rezzolla et al., 2018). Stellar black holes have been detected by LIGO, Virgo and KAGRA when two such black holes merge and send out a gravitational wave (Abbott et al., 2023). At the upper end of the mass spectrum, SMBH masses are typically defined as $M_{\mathrm{BH}} \gtrsim 10^6\,\mathrm{M}_\odot$ and these black holes, as previously described, are found at the centres of galaxies. As stated in §1.4, these black holes power quasars and many at $z \gtrsim 6$ have been discovered using both ground-based and space-based telescopes. Finally in the middle of the mass spectrum, intermediate-mass black holes (IMBHs) are theorised to have $M_{\mathrm{BH}} \sim 10^3 - 10^5\,\mathrm{M}_\odot$. They are a population that still remains elusive but several candidates have been proposed from SDSS Data Release 7 (Chilingarian et al., 2018).

Stellar black holes in the early Universe act as a potential seed for SMBHs, known as light seeds ($M_{\mathrm{BH}} \sim 10^1 - 10^3\,\mathrm{M}_\odot$). Since SMBHs have been found when the Universe was less than 1 Gyr old, these light seeds must be even older. They would originate from the first generation of stars ($z \sim 20 - 30$), known as Population III (Pop III) stars. Pop III stars are theorised to be completely metal-free. When these first generations of stars end their lives as supernovae and create metals through nuclear fusion, the next generations of stars become metal-poor (Pop II) and even later metal-rich (Pop I) (Klessen & Glover, 2023).

One of the main issues with considering light seeds is that given their low initial mass, they would need to grow to $\sim 10^4$ times their mass in just a few hundred Myr. This intense growth would require very high rates of accretion, known as super-Eddington accretion. The Eddington luminosity refers to the maximum luminosity a spherically symmetric body of mass M can have while remaining in hydrostatic equilibrium i.e. the forces due to radiation pressure and gravity are equal and opposite:

$$L_{\mathrm{Ed}} = \frac{4\pi G m_{\mathrm{p}} c}{\sigma_{\mathrm{T}}} M, \tag{1.26}$$

where σ_{T} is the Thomson cross section and we assume that the accreted matter largely consists of ionised hydrogen (Carroll & Ostlie, 2017; Fan et al., 2023). We can use Eq. 1.26 to derive an Eddington accretion rate as:

$$\begin{aligned} L_{\mathrm{Ed}} &= \epsilon_{\mathrm{rad}} \dot{M}_{\mathrm{Ed}} c^2, \\ \dot{M}_{\mathrm{Ed}} &= \frac{L_{\mathrm{Ed}}}{\epsilon_{\mathrm{rad}} c^2}, \\ \dot{M}_{\mathrm{Ed}} &= \frac{4\pi G m_{\mathrm{p}}}{\epsilon_{\mathrm{rad}} \sigma_{\mathrm{T}} c} M, \\ \dot{M}_{\mathrm{Ed}} &\approx (2.218 \times 10^{-8}\,\mathrm{yr}^{-1}) M, \end{aligned} \tag{1.27}$$

where $\epsilon_{\rm rad}$ is the radiative efficiency and is typically set $\epsilon_{\rm rad} = 0.1$. Thus a light seed with an initial mass of $M = 10^2\,{\rm M}_\odot$ would only initially accrete mass at an Eddington-limited rate of $2.218 \times 10^{-6}\,{\rm M}_\odot\,{\rm yr}^{-1}$ which is insufficient given the time scale and final mass required. Super-Eddington accretion may be achieved in gas-rich environments and is unlikely to be sustained for several hundred Myr but rather in episodic bursts (Mehta et al., 2024; Trinca et al., 2024; Hu et al., 2025). An increase to super-Eddington luminosity could also lead to mass loss, driven by radiation feedback.

IMBHs can act as heavy seeds and are an appealing alternative origin for SMBHs as they do not require super-Eddington accretion to reach $10^6\,{\rm M}_\odot$ in the required time (Li et al., 2021). These black holes may form as the end state of a supermassive star (SMS). Such a star could form in particular circumstances where the temperature of the gas is kept high ($T \sim 10^4\,{\rm K}$) to reduce fragmentation and minimise typical star formation. This may be achieved by minimising cooling of the gas by (1) Lyman-Werner radiation dissociating H_2 that acts as a coolant (Dijkstra et al., 2014), (2) relative streaming velocities between baryons and dark matter particles which require deeper potential wells (i.e. larger halo masses) before baryonic collapse (thus delaying star formation) (Tseliakhovich & Hirata, 2010; Hirano et al., 2017) and (3) rapid assembly through major and minor halo mergers which heats the gas within the halos (Yoshida et al., 2003). While IMBHs have a head start in their initial mass, their drawback as a SMBH seed is in their potential rarity (Regan & Volonteri, 2024). In order to form these heavy seeds, extreme conditions as described above must be met to minimise gas cooling within a halo. The main questions with heavy seeds thus are (1) what is their number density and (2) is this number density sufficient to explain the number density of SMBHs currently known? Our attempts to answer these questions are detailed in §3.

1.6 Computational Cosmology

In the final section of this Chapter, we describe some of the numerical tools that we use to investigate the high-redshift Universe: Press-Schechter formalism, its semi-analytic generalisations, the cosmological simulation codes `Enzo` and `SWIFT`, and the Python packages `hmf`, `halomod` and `yt`. We use `Enzo` and `SWIFT` to run dark matter-only simulations and analyse the output using `yt` in §2, we use `halomod` to create halo-halo correlation functions in §3 and we use all other tools listed above in both §2 and §3. These tools are invaluable for testing physical theories against recent observations by JWST.

1.6.1 Press-Schechter Theory

Press-Schechter formalism (PS) is an analytic model that describes how the comoving number density of dark matter halos varies with redshift z and halo mass M (Press & Schechter, 1974). As described in §1.3.1, we consider a virialised halo to be spherically symmetric with a mass M contained within a sphere of average density $\Delta_{\rm c}(z)\rho_{\rm c}(z)$ (see Eq. 1.13). A halo centred at comoving coordinate $\vec{x}$ and redshift z can be associated with some peak in the matter density field $\rho_{\rm m}(\vec{x}, z)$ (Bardeen et al., 1986). This can be expressed as an overdensity compared to the mean matter density $\bar{\rho}_{\rm m}(z) = \Omega_{\rm m}(z)\rho_{\rm c}(z)$:

$$\delta(\vec{x}, z) = \frac{\rho_{\rm m}(\vec{x}, z)}{\bar{\rho}_m(z)} - 1. \tag{1.28}$$

The space and time dependence of this overdensity field can be separated as:

$$\begin{aligned} \delta(\vec{x}, z) &= D(a(z))\delta(\vec{x}), \\ \delta(\vec{x}) &= \frac{\delta(\vec{x}, z)}{D(a(z))}, \end{aligned} \tag{1.29}$$

where $\delta(\vec{x})$ is the space-dependent overdensity field and $D(a)$ is the linear growth factor given as:

$$\begin{aligned} D(a) &= \frac{5\Omega_{\rm m,0}}{2} \frac{H(a)}{H_0} \int_0^a \frac{da'}{\left[a' H(a')/H_0\right]^3}, \\ a &= \frac{1}{1+z}. \end{aligned} \tag{1.30}$$

The linear growth factor can be normalised to some reference $z = z_0$ such that $D(a(z_0)) = 1$. A region centred at $\vec{x}$ will collapse to produce a dark matter halo by redshift z if $\delta(\vec{x}) > \delta_{\rm c}/D(a(z))$ where $\delta_{\rm c} \approx 1.686$ is known as the critical overdensity (Binney & Tremaine, 2008).

The variance of this overdensity field can be computed as:

$$\sigma^2 = \langle \delta^2 \rangle = \frac{1}{V} \int \delta(\vec{x})^2 \mathrm{d}^3\vec{x} = \frac{1}{(2\pi)^3} \int P(\vec{k}) \mathrm{d}^3\vec{k} = \frac{1}{2\pi^2} \int_0^\infty k^2 \, P(k) \, \mathrm{d}k, \tag{1.31}$$

where V is the volume of the Universe and $P(k)$ is the spherically symmetric power spectrum. We define a smoothed overdensity field $\delta_R = \delta(\vec{x}; R)$ that is associated with a region of size R using a filter function $W(\vec{x}; R)$ (with dimensions of volume^{-1}):

$$\begin{aligned} \delta(\vec{x}; R) &= \int \delta(\vec{x}') \, W(\vec{x} - \vec{x}'; R) \, \mathrm{d}^3\vec{x}', \\ \int W(\vec{x} - \vec{x}'; R) \, \mathrm{d}^3\vec{x}' &= 1. \end{aligned} \tag{1.32}$$

We use the Top Hat filter given in coordinate space as:

$$W(r;R) = \begin{cases} \frac{3}{4\pi R^3} & \text{if } r \leq R, \\ 0 & \text{if } r > R, \end{cases} \tag{1.33}$$

and in k-space as:

$$\tilde{W}(kR) = \frac{3}{(kR)^3}\left[\sin(kR) - (kR)\cos(kR)\right]. \tag{1.34}$$

We can define a new variance σ_R associated with this region as:

$$\sigma^2(R) = \frac{1}{2\pi^2}\int_0^\infty k^2\, P(k)\, \tilde{W}^2(kR)\, dk, \tag{1.35}$$

as seen previously in §1.2 in Eq. 1.12. The corresponding mass M associated with this overdensity is $M = 4\pi\bar{\rho}_{\mathrm{m},0}R^3/3$ (van den Bosch et al., 2013). We can describe this filter using its radius R or mass M. Thus we can set the smoothed overdensity and variance as $\delta_M = \delta_R$ and $\sigma_M = \sigma_R$ respectively. We can show that σ_M is the mass variance by considering a region of mass $M(\vec{x};R)$ centred at $\vec{x}$ and contained within a volume V_R associated with a filter of size R:

$$M(\vec{x};R) = V_R \int \rho_{\mathrm{m}}(\vec{x}')\, W(\vec{x}-\vec{x}';R)\, \mathrm{d}^3\vec{x}'. \tag{1.36}$$

The density $\rho_{\mathrm{m}}(\vec{x}')$ can be related to the overdensity field $\delta(\vec{x}')$ as:

$$\begin{aligned} \delta(\vec{x}') &= \frac{\rho_{\mathrm{m}}(\vec{x}')}{\bar{\rho}_{\mathrm{m},0}} - 1, \\ \rho_{\mathrm{m}}(\vec{x}') &= \bar{\rho}_{\mathrm{m},0}(1+\delta(\vec{x}')). \end{aligned} \tag{1.37}$$

By substituting Eq. 1.37 into Eq. 1.36 and noting that $\bar{M} = V_R\bar{\rho}_{\mathrm{m},0}$, we find:

$$\delta(\vec{x};R) = \frac{M(\vec{x};R) - \bar{M}}{\bar{M}}. \tag{1.38}$$

Finally we can compute the smoothed variance associated with this filter and see that it is equal to the mass variance:

$$\begin{aligned} \sigma^2(R) &= \langle \delta^2(\vec{x};R)\rangle, \\ \sigma^2(R) &= \left\langle \left(\frac{M(\vec{x};R)-\bar{M}}{\bar{M}}\right)^2 \right\rangle, \\ \sigma^2(R) &= \sigma_M^2. \end{aligned} \tag{1.39}$$

In Press-Schechter formalism, the overdensity δ_M is a Gaussian random field

such that the probability that the overdensity exceeds the critical overdensity δ_c is:

$$\mathcal{P}(\delta_M > \delta_c) = \frac{1}{\sqrt{2\pi}\sigma_M} \int_{\delta_c}^{\infty} \exp\Big[- \frac{\delta_M^2}{2\sigma_M^2} \Big] \, \mathrm{d}\delta_M. \tag{1.40}$$

An issue with associating a given halo with a unique overdensity peak is the cloud-in-cloud problem: the ambiguity of whether a mass element belongs to a halo of mass M_1 or M_2 if it is associated with both peaks δ_{M_1} and δ_{M_2}. So rather than associate a halo with a unique density peak, this probability is equal to the fraction of the total mass of the Universe at a given redshift z that is contained within halos of mass greater than M. So what is the fraction of the total mass of the Universe at any redshift contained within halos of mass greater than $M = 0$ i.e. halos of any mass? Using Eq. 1.40 and setting $M \to 0$ and $\sigma_M \to \infty$, we find that $\mathcal{P} \to 1/2$ i.e. seemingly only half of the mass in the Universe is contained within halos. This was somewhat controversially resolved by Press & Schechter with the introduction of a so-called "fudge factor" of 2.

This reasoning is what allows us to compute the halo mass function i.e. the number of halos per comoving volume at redshift z with masses in the range $[M, M + \mathrm{d}M]$:

$$\frac{\mathrm{d}n_{\mathrm{PS}}(z, M)}{\mathrm{d}M} dM = \sqrt{\frac{2}{\pi}} \frac{\bar{\rho}_{\mathrm{m},0}}{M^2} \frac{\delta_c}{\sigma_M} \exp\Big[- \frac{\delta_c^2}{2\sigma_M^2} \Big] \left| \frac{\mathrm{d}\ln \sigma_M}{\mathrm{d}\ln M} \right| \mathrm{d}M, \tag{1.41}$$

where we include the z-dependence in σ_M through the power spectrum $P(z, k)$. The Press-Schechter halo mass function has been used to estimate the number density of dark matter halos, galaxies and SMBHs as a function of redshift z and halo mass M. A drawback is its tendency to overpredict the number density of halos at the low-mass end and underpredict the number density of halos at the high-mass end when compared to simulations of the local Universe (Springel et al., 2005). This discrepancy worsens at higher redshift. Another issue is the spherical collapse of halos being too simplistic. It has nonetheless been incredibly influential and its formalism has been the basis for many other descriptions of halo abundancy.

1.6.2 Generalisations of the Halo Mass Function

Since its original publication in 1974, there have been many generalisations of Press-Schechter formalism that aim to bridge the gap between theory, simulation results and observations. Eq. 1.41 can be generalised as:

$$\frac{\mathrm{d}n(z, M)}{\mathrm{d}M} dM = \frac{\bar{\rho}_{\mathrm{m},0}}{M^2} f(\sigma_M) \left| \frac{\mathrm{d}\ln \sigma_M}{\mathrm{d}\ln M} \right| \mathrm{d}M, \tag{1.42}$$

where $f(\sigma_M)$ is some function of the mass variance and

$$f_{\rm PS}(\sigma_M) = \sqrt{\frac{2}{\pi}}\frac{\delta_{\rm c}}{\sigma_M}\exp\left(-\frac{\delta_{\rm c}^2}{2\sigma_M^2}\right). \tag{1.43}$$

By considering the Zel'dovich approximation (Zel'dovich, 1970) (the velocity of a particle is the same direction as its initial displacement) in the linear regime, we find that prospective halos would collapse in an ellipsoidal manner rather than spherical. Sheth et al. (2001) (SMT) assume that the critical overdensity for ellipsoidal collapse $\delta_{\rm ec}$ depends on the mass variance σ_M and halo mass M, in contrast to spherical collapse in Press-Schechter formalism where $\delta_{\rm sc} = \delta_{\rm c}$ is a constant:

$$\frac{\delta_{\rm ec}}{\delta_{\rm sc}} \approx 1 + \beta\left[5(e^2 \pm p^2)\frac{\delta_{\rm ec}^2}{\delta_{\rm sc}^2}\right]^{\gamma}, \tag{1.44}$$

where $\beta = 0.47$, $\gamma = 0.615$, and the initial displacement field is described by the ellipicity e and the prolateness p. SMT found that when considering Gaussian fluctuations, $e = (\sigma_M/\delta_{\rm ec})/\sqrt{5}$ and $p = 0$ were the most probable values which leads to:

$$\frac{\delta_{\rm ec}}{\delta_{\rm sc}} \approx 1 + \beta\left[\frac{\sigma_M^2}{\delta_{\rm sc}^2}\right]^{\gamma}. \tag{1.45}$$

The SMT halo mass function $f_{\rm SMT}(\sigma_M)$ cannot be determined analytically due to this varying critical overdensity. It has been determined using Monte Carlo simulations as:

$$\begin{aligned} f_{\rm SMT}(\sigma_M) &= A\sqrt{\frac{2a}{\pi}}\left[1 + \left(\frac{\sigma_M^2}{a\delta_{\rm c}^2}\right)^p\right]\frac{\delta_{\rm c}}{\sigma_M}\exp\left(-\frac{a\delta_{\rm c}^2}{2\sigma_M^2}\right), \\ f_{\rm SMT}(\sigma_M) &= A\left[1 + \left(\frac{\sigma_M^2}{a\delta_{\rm c}^2}\right)^p\right] f_{\rm PS}\left(\frac{\sigma_M}{\sqrt{a}}\right), \end{aligned} \tag{1.46}$$

where $A = 0.3222$, $a = 0.707$ and $p = 0.3$. The SMT halo mass function is a better match than PS against N-body simulations especially in the local Universe (Springel et al., 2005) but overpredicts the number of halos by a factor of 10 compared to simulation results at $z > 10$ (Klypin et al., 2011). Many other generalisations exist that are derived from simulation results such as Reed07 (Reed et al., 2007), WatsonS0 and WatsonFoF (Watson et al., 2013) (see Table 1 of Murray et al. (2013) to see a summary of fitting functions $f(\sigma_M)$.) We compare each of these against simulation results in §2.

1.6.3 `Enzo`

The `Enzo` simulation code is an N-body cosmological hydrodynamics code capable of probing physics of the high-redshift Universe. It was first developed in the 1990s and 2000s (Bryan & Norman, 1997b,a; Norman & Bryan, 1999; O'Shea

et al., 2004; Norman et al., 2007), its 2.3 version was released in 2014 with its method paper (Bryan et al., 2014) and we use its 2.6 version released in 2019 (Brummel-Smith et al., 2019). `Enzo` has been used to investigate galaxy formation (Kim et al., 2014), the circumgalactic medium (Peeples et al., 2019) and Pop III star formation (Kulkarni et al., 2021).

`Enzo` is an adaptive mesh refinement (AMR) code which allows certain regions of the simulation volume (e.g. dark matter halos) to be highly resolved in a computationally effective way. The structure is a hierarchy of parent and child grids and the workload at a given level is distributed evenly across all processors. The child grids are better resolved than their parent grid by a factor of 2. A grid is a real grid on a given processor if its data is allocated to that processor. If the data is allocated on a different processor, then this grid is known as a ghost grid. Within a real grid, real zones store data field values (e.g. particle positions and velocities) and ghost zones temporarily store values from neighbouring and parent grids in order to update the real grids (see Figure 1.13).

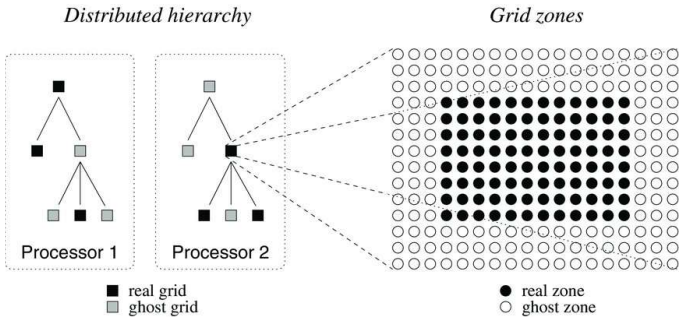

Figure 1.13: Sample 2D hierarchy of parent and child grids, taken from Figure 1 of Bryan et al. (2014). A given grid is real on only one processor and is a ghost grid on all others. A child grid must have only one parent grid but parent grids can have multiple child grids. Refinement increases as the level increases, top to bottom in the left panel.

We use `Enzo` for dark matter-only simulation runs in §2 such that the particles are only influenced by gravity. At each time step at the root grid, the Poisson equation is finite-differenced and solved using Fast Fourier Transforms:

$$\nabla^2 \vec{\Phi}(\vec{x}) = 4\pi G \rho(\vec{x}), \tag{1.47}$$

where $\vec{\Phi}$ is the gravitational potential. The boundary conditions on the child grids are interpolated from the parent grid and the Poisson equation is then solved one child grid at a time. The particle positions and velocities are then updated at each time step, see Figure 1.14 to see the order of operations in a sample grid structure.

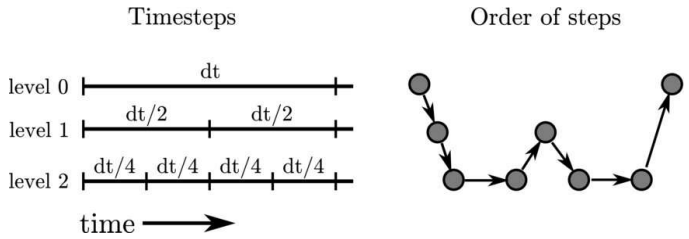

Figure 1.14: Order of operations in a sample grid structure, taken from Figure 2 of Bryan et al. (2014).

1.6.4 SWIFT

The *SPH With Inter-dependent Fine-grained Tasking* (SWIFT) simulation code is another cosmological hydrodynamics code suited for probing the high-redshift Universe and differs from Enzo in both its structure and its gravity solver (Schaller et al., 2018, 2024). It has been used to simulate star formation in disk galaxies (Nobels et al., 2024), jets from AGNs (Huško & Lacey, 2023) and high-redshift galaxy clustering (Pizzati et al., 2024).

SWIFT is a tree-based particle-mesh code with a smoothed particle hydrodynamics (SPH) solver. SPH is a computational method for solving the equations of hydrodynamics within a simulation volume by computing the density at a point using a weighted sum of nearest neighbouring particles, naturally forming neighbourhoods of varying volumes (Price, 2012). This neighbourhood structure leads to the formation of a Cartesian cell grid where the cell width is comparable to the particle-neighbour search radius. While hydrodynamics are not relevant for our simulations since they are dark matter-only, SWIFT uses this created structure to solve Poisson's equation. These cells can be viewed as a set of tree nodes and leaves and we consider interactions between particles within the same cell, particles of neighbouring cells and particles of distant cells (see Figure 1.15).

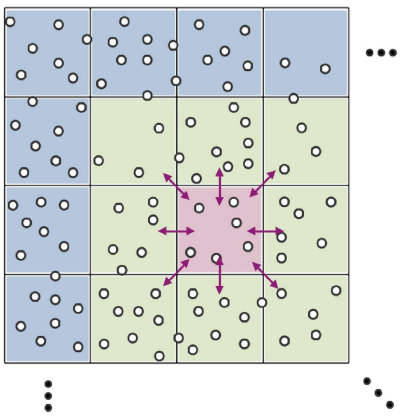

Figure 1.15: The Fast Multipole Method tree-walk for a sample cell (red) shown in 2D, taken from Figure 13 of Schaller et al. (2024). Within the red cell, we consider interactions between pairs of particles. The gravity kernels (P2M, M2L, L2P) are computed for each of the green-red cell pairs. The M2L kernel is computed for the total contribution of blue cells interacting with the red cell.

The gravitational potential ϕ experienced by particle a at point $\vec{x_a}$ due to every other particle in the simulation volume is given as:

$$\phi(\vec{x_a}) = \sum_{b \neq a} G m_b \varphi(\vec{x_a} - \vec{x_b}), \tag{1.48}$$

where φ refers to a potential corresponding to the density distribution. The Fast Multipole Method (FMM) is an approximation for computing this gravitational potential (Cheng et al., 1999). Computationally, this involves evaluating three different summations (or kernels): particle-to-multipole (P2M), multipole-to-local-expansion (M2L) and local-expansion-to-particle (L2P). This results in groups of particles with a sufficiently large separation (distant cells) being treated as point masses rather than as individual particles.

1.6.5 Python Packages

We use many specialised Python packages in our analysis pipelines. `hmf` and `halomod` allow one to make use of built-in analytic and semi-analytic halo mass functions, correlation functions and more while varying cosmological and numerical parameters (Murray et al., 2013; Murray et al., 2021). Many of the cosmological functions are derived using built-in `astropy` functions (Astropy Collaboration et al., 2013, 2018, 2022).

We use `yt` and `yt-astro-analysis` (Turk et al., 2011; Smith et al., 2022) to process output from our `Enzo` and `SWIFT` simulations and build halo catalogues. For `SWIFT`, we use the specialised version `yt-swift` that can read this output format (Rennehan, 2022).

We also filter out the noise of our data using a Savitzky-Golay filter (Savitzky & Golay, 1964) in Python. The degree of filtering is determined by two parameters: the window length w and the polynomial order p. The window length w refers to the number of consecutive points from a dataset which are selected at a time. These points are fitted to a polynomial of order p. We use this filter to create fits illustrating what trends the raw data clearly describe without distorting them. We can achieve this by maximimising the number of non-zero data points. We do this by optimising the number of histogram bins used when binning data by halo mass M (see §2.3) or redshift z (see §3.3).

Chapter 2

Halo Mass Functions at High Redshift

2.1 Introduction

Since its launch in December 2021 and its subsequent data releases in the months since, JWST has both reshaped and challenged our understanding of galaxy formation in the very early Universe ($z \gtrsim 10$). In particular, JWST has discovered a number of very massive and very luminous galaxies at redshifts in excess of $z = 10$ which, after initial photometric detection, have now been spectroscopically confirmed (Harikane et al., 2024; Arrabal Haro et al., 2023; Castellano et al., 2024; Hainline et al., 2024; Gentile et al., 2024). These galaxies, both in terms of their intrinsic luminosity and their potential host halo masses, provide a significant challenge to our understanding of structure formation in the early Universe. Boylan-Kolchin (2023), using an analytic model applied to the inferred JWST stellar masses of a number of high-redshift sources from Labbé et al. (2023), found that the stellar masses implied by the sources required star formation efficiencies, ϵ_*, significantly in excess of those from the present-day Universe and perhaps as implausibly high as $\epsilon_* = 1$. The model employed by Boylan-Kolchin (2023) hinges on a number of simple yet strong assumptions. These assumptions use the inferred stellar host mass to derive a host halo mass based on the ratios between the cosmic baryon density and the cosmic matter density and the star formation efficiency. These simple arguments culminate in a calculation of the probability of finding such (luminous) galaxies at early times in a ΛCDM universe.

Boylan-Kolchin (2023) conclude that the most massive JWST galaxies detected are both at the very limit of galaxy formation theory and that their number densities are difficult to equate with the JWST field of view. They conclude that these issues indicate that there are several unresolved issues in our theories. However, underneath the model employed by Boylan-Kolchin (2023) are a number of astrophysical assumptions which are used when converting the broadband

spectral energy distribution to a host stellar mass. This conversion is open to large uncertainties - particularly since our knowledge of how to do this conversion comes from the local Universe. There is no guarantee that these conversion relations can be directly mapped to the high-z Universe and in fact most analysis shows that it is almost certainly not the case (e.g. Kannan et al., 2023; Lu et al., 2025). For example, recent analysis by Steinhardt et al. (2023) show that modifying the host population IMF of the inferred stellar population results in a decrease in the stellar mass by factors of between 10 and 50. Such decreases in the host stellar mass have a direct knock-on effect to the inferred host halo mass and can significantly decrease the tension with ΛCDM models.

Adding to this important point is that Boylan-Kolchin (2023) (as well as many other studies) utilise the well-tested and parameterised halo mass function (HMF) derived by Sheth & Tormen (1999) in order to compute their galaxy number densities and cumulative comoving number density of galaxies. An important consideration therefore is to test, using explicit N-body calculations, how accurate the underlying HMF is at high-z (i.e. at $z \gtrsim 10$), compared to direct N-body calculations, and what error may be associated with this model. This is the goal of this study.

While preparing this Chapter, a study by Yung et al. (2024b) performed a similar investigation. Using a high-fidelity suite of N-body simulations across a broad range of box sizes and redshifts, Yung et al. (2024b) were able to show that HMFs derived from fitting functions and analytical approximations match extremely well to their N-body simulations. Yung et al. (2024b) found that even up to $z = 15$ the match between their N-body simulations and the fitting functions is no more than approximately a factor of two across a range of fitting functions. As discussed above, providing robust quantification of the match between fitting functions and direct N-body calculations at high-z is extremely timely given the recent JWST results.

This is particularly relevant when trying to understand the probability of finding such luminous and massive galaxies within a JWST field of view. Thus far several studies have tested the first results from JWST against state-of-the-art hydrodynamical simulations and the results agree within a factor of a few (e.g. Keller et al., 2023; McCaffrey et al., 2023; Sun et al., 2023; Rennehan, 2024). It is therefore timely to quantify potential sources of systematic error when comparing observations and models.

Here we perform a similar analysis to Yung et al. (2024b), with the difference being that we compare (semi-)analytical halo mass functions against two fundamentally different numerical codes - `Enzo` (Bryan et al., 2014; Brummel-Smith et al., 2019) and `SWIFT` (Schaller et al., 2018, 2024). While Yung et al. (2024b) used the publicly available `GADGET2` code (Springel (2005)), which is a TreePM

code with a similar gravitational solver to SWIFT, we also use the Particle-Mesh based Enzo code which gives an additional layer of comparison. Our analysis confirms the results of Yung et al. (2024b) and we generally observe a factor of approximately two difference between the HMFs generated by the N-body codes and the SMT and WatsonFoF fitting functions.

The structure of the Chapter is as follows: In §2.2 we outline the methodology including the simulations and fitting functions employed. In §2.3 we deliver the results of our analysis and in §2.4 we summarize and discuss our results in light of recent JWST observations.

2.2 Methodology

2.2.1 Numerical Simulations

We run a series of dark matter-only simulations using Enzo and SWIFT of varying resolutions, achieved by varying both the box size and particle number. The box size varies from $L = 0.5$ cMpc/h to 100.0 cMpc/h and the particle number varies from $N_{\rm DM} = 512^3$ to 1024^3. Details of the simulation boxes are summarised in Tables 2.1 and 2.2.

L [cMpc/h]	$N_{\rm DM}^{1/3}$	$\rm M_{DM}$ [$\rm M_\odot$/h]
0.5	512	6.69×10^1
1.5	512	1.81×10^3
2.5	512	8.37×10^3
7.5	1024	2.83×10^4
7.5	512	2.26×10^5
12.5	1024	1.31×10^5
12.5	512	1.05×10^6
25.0	1024	1.05×10^6
25.0	512	8.37×10^6
50.0	1024	8.37×10^6
50.0	512	6.70×10^7
100.0	1024	6.70×10^7
100.0	512	5.36×10^8

Table 2.1: Mass resolutions of each simulation box. All simulations but the $L = 7.5$ cMpc/h, $N_{\rm DM}^{1/3} = 1024$ box are run using both Enzo and SWIFT; this box is run using SWIFT only.

Our simulations begin at $z = 127.0$ with initial conditions set using MUSIC (Hahn & Abel (2011)) and end at $z = 10.0$. We use a ΛCDM cosmology with h = 0.6774,

L [cMpc/h]	$N_{\rm DM}^{1/3}$	$\Delta x_{\rm Enzo}$ [cpc/h]	$\Delta x_{\rm SWIFT}$ [cpc/h]
0.5	512	7.63×10^0	3.91×10^1
1.5	512	2.29×10^1	1.17×10^2
2.5	512	3.82×10^1	1.95×10^2
7.5	1024	-	2.93×10^2
7.5	512	1.14×10^2	5.86×10^2
12.5	1024	9.54×10^1	4.88×10^2
12.5	512	1.91×10^2	9.77×10^2
25.0	1024	1.91×10^2	9.77×10^2
25.0	512	3.82×10^2	1.95×10^3
50.0	1024	3.82×10^2	1.95×10^3
50.0	512	7.63×10^2	3.91×10^3
100.0	1024	7.63×10^2	3.91×10^3
100.0	512	1.53×10^3	7.81×10^3

Table 2.2: Highest space resolutions of each simulation box. All simulations but the $L = 7.5$ cMpc/h, $N_{\rm DM}^{1/3} = 1024$ box are run using both `Enzo` and `SWIFT`; this box is run using `SWIFT` only.

$\Omega_{\rm m,0} = 0.2592$, $\Omega_{\Lambda,0} = 0.7408$, $\sigma_8 = 0.8159$, $n_{\rm s} = 0.9667$ and the Eisenstein & Hu (1998) transfer function for no baryon acoustic oscillations. The two codes we use, `Enzo` and `SWIFT`, are both well-tested and have been used extensively within the community. Additionally, both codes use somewhat different strategies for solving the Poisson equation which allows for additional comparison between the various semi-analytic fits against numerical solutions. We now describe our application of both codes but refer the interested reader to the code method papers for more details.

`Enzo` is a grid-based N-body code with the capability for adaptive mesh refinement (AMR), widely used in cosmological hydrodynamics simulations. The AMR allows for improved resolution in areas of interest (e.g. collapsing structures) without greatly increasing computational cost and without needing prior knowledge of the volume to pre-select areas for increased refinement. The gravity solver works by implementing a Fast Fourier Transform (FFT) technique to solve Poisson's equation at the root grid of each timestep of the simulation. The boundary conditions on the subgrids are then interpolated from the parent grid and the Poisson equation is solved at each time step, one subgrid at a time. For a Unigrid `Enzo` simulation (i.e. no refinement), the minimum inter-particle separation in which gravity acts is twice the length of a cell, given as:

$$\Delta x_{\rm Unigrid} = 2\frac{L}{N_{\rm DM}^{1/3}}. \tag{2.1}$$

When running `Enzo` simulations, we used a maximum refinement level of 8, meaning that the resolution was increased by a factor 2^8 in regions of high particle density. This means the highest resolution is given as:

$$\Delta x_{\rm Enzo} = \frac{1}{2^8}\Delta x_{\rm Unigrid} = \frac{1}{2^7}\frac{L}{N_{\rm DM}^{1/3}}. \tag{2.2}$$

For the dark matter-only simulations carried out here, refinement is triggered once the particle over-density reaches a factor of 4 greater than the mean density (i.e. `MinimumOverDensityForRefinement = 4`). In addition to this we set the `MinimumMassForRefinementLevelExponent = -0.1` which makes the refinement scheme super-Lagrangian and allows for the higher levels of refinement to be more easily triggered (see e.g. O'Shea et al., 2005).

SPH With Inter-dependent Fine-grained Tasking - `SWIFT` - combines a tree-based N-body solver with a smoothed particle hydrodynamics (SPH) solver. In this study, we use the adaptive mode of the Fast Multipole Method (FMM) (Cheng et al. (1999)). This implements a Taylor expansion twice to resolve the gravitational potential (and later the forces) between particles in different cells. We set the accuracy criterion $\epsilon_{\rm FMM} = 0.001$. `SWIFT` takes advantage of the hierarchical tree structure to efficiently solve for the gravitational forces between particles. Particles from nearest neighbour cells are treated as individuals. A group of particles from distant cells are approximated as one particle with the total mass of the group located at the centre of mass. Long-range forces are resolved using a Fast Fourier Transform algorithm (Frigo & Johnson (2005)).

It is a non-trivial matter comparing `Enzo` and `SWIFT` due to the difference in the gravity solvers. Also the highest spatial resolution for an `Enzo` simulation, $\Delta x_{\rm Enzo}$, applies only to regions of high particle density while the softening length for a `SWIFT` simulation, $\Delta x_{\rm SWIFT}$, applies to the entire simulation volume. We compromise by setting the softening length to an intermediate value, between $\Delta x_{\rm Unigrid}$ and $\Delta x_{\rm Enzo}$:

$$\Delta x_{\rm SWIFT} = \frac{1}{5^2}\frac{L}{N_{\rm DM}^{1/3}}. \tag{2.3}$$

This softening length provides an upper bound when computing the gravitational forces between two nearby particles. Since the force $F_{\rm g}$ is an inverse square law, as the separation between two particles $r \to 0$, the force $F_{\rm g} \to \infty$:

$$F_{\rm g} = \frac{Gm_1m_2}{r^2}. \tag{2.4}$$

This force is modified with the softening length as such:

$$F'_{\rm g} = \frac{Gm_1m_2}{(r + \Delta x_{\rm SWIFT})^2}. \tag{2.5}$$

Finally, the initial conditions files for both simulation codes must be in .hdf5 format. The `SWIFT` initial conditions files are in binary format and can be converted to .hdf5 format using a Python script written by Bakels (2018).

2.2.2 Numerical Halo Finders

As discussed in §2.1, the goal of this study is to determine the differences between (semi-)analytic HMFs and those derived from direct N-body simulations. In order to determine the HMF from the cosmological simulations we must employ a halo finder and decide on the redshifts at which to evaluate the HMFs.

We analyse the simulation snapshots from our full suite of outputs at $z = 20.0$, $z = 15.0$ and $z = 10.0$ using both a friends-of-friends (FOF) (Efstathiou et al. (1985)) and HOP (Eisenstein & Hut (1998)) halo finder (results from the HOP finder can be found in §2.5 as the results are very similar between FOF and HOP and the goal of this study is not to compare halo finders). The FOF halo finder accounts for the distances between dark matter particles within a single snapshot. We use a linking length $\Delta x(b) = b \times L/N_{\rm DM}^{1/3}$, where $L/N_{\rm DM}^{1/3}$ is the mean inter-particle separation. This refers to the maximum permitted separation between two particles. A group i.e. halo is found from a set of inter-linked particles.

Our halos are approximated as spheres and ideally, we choose b such that each halo encompasses a volume with an overdensity $\Delta_{\rm c} \approx 18\pi^2$ i.e. 178 times the critical density $\rho_{\rm c}(z)$ (Bryan & Norman (1998)). The Python package `hmf` (Murray et al., 2013) provides an approximation relating $\Delta_{\rm c}$ and b:

$$\Delta_{\rm c}(z) = \frac{9}{2\pi b^3}\,\Omega_{\rm m}(z). \tag{2.6}$$

As $z \to \infty$, $\Omega_{\rm m}(z) \to 1$ in our cosmology. Therefore, $b = 0.2$ results in a predicted overdensity of $\Delta_{\rm c} \approx 178$ and this is the value we choose for our FOF algorithm.

The HOP halo finder accounts for the distances between particles as well as the computed density of each particle. Rather than creating a continuous density field in the simulation volume, the density of each particle at its given position is estimated using a spherically symmetric cubic spline kernel (Monaghan & Lattanzio (1985)) on its $N_{\rm dens} = 64$ nearest neighbours. The density is normalised to the average density of particles within the simulation box e.g. a particle with a computed density of $\delta = 80$ refers to a position 80 times denser than the average i.e. an overdensity (Skory et al. (2010)). A link is made by hopping from a given particle to the densest of its $N_{\rm hop} = 64$ neighbours. This process continues, forming a chain of increasing particle density until we reach a particle that is its own densest neighbour. All chains sharing the same densest particle are part of the same group. If the maximum particle density within a group is above a set threshold overdensity $\delta_{\rm peak}$, that group is defined as a halo. We use a threshold

overdensity of $\delta_{\text{peak}} = 100$. This value was chosen to calibrate the HOP finder with the FOF finder so both halo finders found a similar halo number and mass range for the `Enzo`, $L = 0.5$ cMpc/h, $N_{\text{DM}} = 512^3$, $z = 10$ snapshot.

The halo masses found from these halo catalogues are the FOF and HOP masses i.e. the mass of the halo is defined as the sum of the masses of the particles that make up the halos. After we create halo catalogues based on these halo finders, we only include halos made up of at least $N_{\text{DM, min}} = 100$ particles to reduce numerical over-counting (i.e. halos must be well resolved (by at least 100 particles) before we identify them as halos).

We find that there is little difference between the number densities found using FOF and HOP for a given simulation suite, with HOP underestimating the FOF number densities by a factor of ≈ 2 at most (see Figure 2.1 for a comparison). Given that the halo finder parameters were calibrated at $z = 10.0$, it is not surprising that there is little mass variance in their number density ratio at this redshift. In §2.3, we show the results for FOF only and leave those from HOP to §2.5.

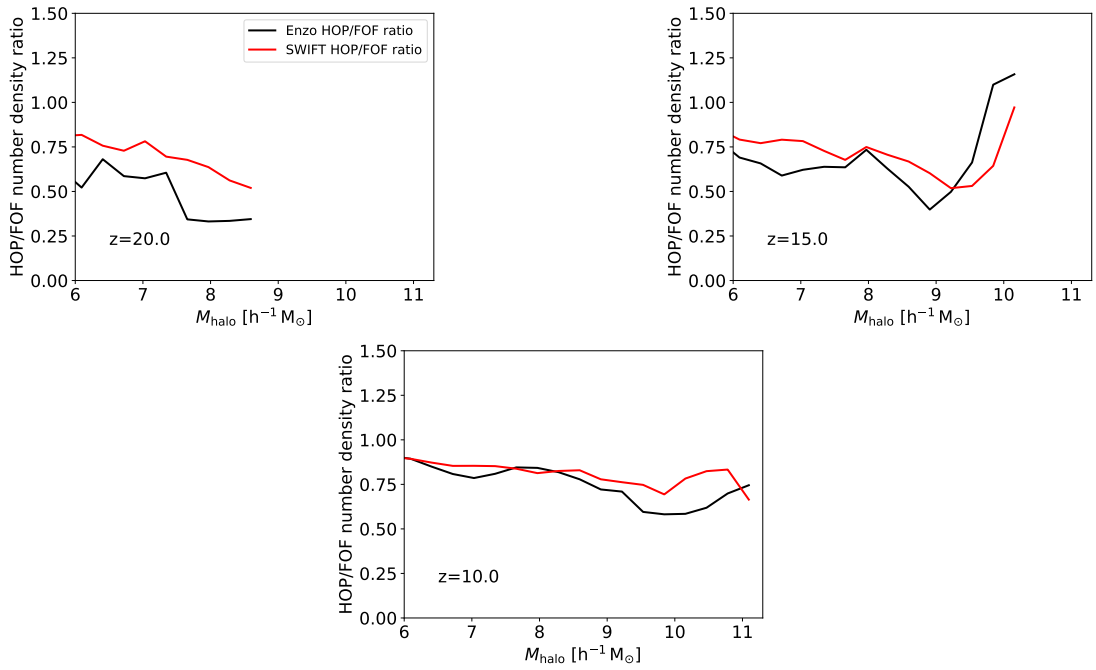

Figure 2.1: Comparing the FOF and HOP halo number densities derived from `Enzo` and `SWIFT` simulation data (with halo masses on a logarithmic scale). We show how the ratio of the HOP number density to the FOF number density varies with halo mass. The HOP number density is within a factor of 2 of its FOF counterpart - particularly at the $z = 10$ outputs. Some larger deviations at higher z are seen as expected.

2.2.3 Numerical Halo Number Densities

A halo catalogue is created from each snapshot with a specific halo finder using the `yt`[1] and `yt-astro-analysis` packages (Turk et al. (2011), Smith et al. (2022)). An array of halo mass values is generated from each halo catalogue, filtered to exclude halos consisting of $< N_{\text{DM, min}}$ particles. For each array, the halo mass values are binned on a logarithmic scale into 24 histogram bins with $M_{\text{min}} = 10^{3.75}\,\text{M}_\odot/\text{h}$ and $M_{\text{max}} = 10^{11.75}\,\text{M}_\odot/\text{h}$. Halo catalogues from a given simulation suite, halo finder and redshift, z, are combined, giving rise to 12 datasets (see Table 2.3 for more detail). For each `Enzo` dataset, we combine halo catalogues based on 12 simulation boxes. For each `SWIFT` dataset, we combine halo catalogues based on 13 simulation boxes (see Tables 2.1 and 2.2 for more detail). In our algorithm below, we index datasets with $i \in \{1, \cdots, 12\}$, mass bins with $j \in \{1, \cdots, 24\}$, `Enzo` simulation boxes with $k \in \{1, \cdots, 12\}$, and `SWIFT` simulation boxes with $k \in \{1, \cdots, 13\}$.

Simulation	Halo finder	Snapshot Redshift (z)
`Enzo`	FOF	20.0
		15.0
		10.0
	HOP	20.0
		15.0
		10.0
`SWIFT`	FOF	20.0
		15.0
		10.0
	HOP	20.0
		15.0
		10.0

Table 2.3: The 12 datasets derived by combining halo catalogues for each simulation suite, halo finder, and redshift combination.

For example, consider the $i = 3$ dataset (`Enzo`, FOF, $z = 10.0$). Say we wish to find the number density $n^{\text{num}}_{\text{halo, } i=3}(M_{\text{mid, } j})$ of the j^{th} bin centred at some mass $\log_{10}(M_{\text{mid, } j}/\text{h}^{-1}\,\text{M}_\odot)$. We count the number of halos $N_{\text{halo, } 3,j,k}$ in this bin for each simulation box $\forall k = 1, \cdots, 12$ and this specific halo number density is given as:

$$n^{\text{num}}_{\text{halo, } 3,j,k}(M_{\text{mid, } j}) = \frac{N_{\text{halo, } 3,j,k}}{V_k}, \tag{2.7}$$

[1]We use a version of `yt` called `yt-swift` developed by Rennehan (2022) as the most recently available version of `yt` cannot load `SWIFT` output data.

where V_k is the comoving volume of the k^{th} simulation box. We find the halo number density $n^{\text{num}}_{\text{halo},\,3}(M_{\text{mid},\,j})$ by averaging over all non-zero number densities across all 12 simulation boxes:

$$n^{\text{num}}_{\text{halo},\,3}(M_{\text{mid},\,j}) = \frac{1}{S_{3,j}} \sum_k n^{\text{num}}_{\text{halo},\,3,j,k}(M_{\text{mid},\,j}), \tag{2.8}$$

where $S_{3,j}$ is the number of halo catalogues that found a non-zero halo number density for the j^{th} bin in this dataset. We can generalise the above equation for the i^{th} dataset and j^{th} bin as:

$$n^{\text{num}}_{\text{halo},\,i}(M_{\text{mid},\,j}) = \frac{1}{S_{ij}} \sum_k n^{\text{num}}_{\text{halo},\,ijk}(M_{\text{mid},\,j}). \tag{2.9}$$

2.2.4 (Semi-)Analytical Halo Mass Functions

We compare our numerical halo number densities with those derived from both analytical forms and popular fits. The number density (units: $\mathrm{h^3\,cMpc^{-3}}$) of dark matter halos at a given redshift, z, in a mass bin centred at $\log_{10}(M_{\text{mid}}/\mathrm{h^{-1}\,M_\odot})$ with a width of $\Delta \log_{10} M$ is defined as:

$$\begin{aligned} n^{\text{fit}}_{\text{halo}}(z, M_{\text{mid}}) &= \int_{M_{\text{a}}(M_{\text{mid}})}^{M_{\text{b}}(M_{\text{mid}})} \frac{dn}{dM}(z, M)\, dM, \\ \log_{10} M_{\text{a}}(M_{\text{mid}}) &= \log_{10}\left(\frac{M_{\text{mid}}}{\mathrm{h^{-1}\,M_\odot}}\right) - \frac{\Delta \log_{10} M}{2}, \\ \log_{10} M_{\text{b}}(M_{\text{mid}}) &= \log_{10}\left(\frac{M_{\text{mid}}}{\mathrm{h^{-1}\,M_\odot}}\right) + \frac{\Delta \log_{10} M}{2}. \end{aligned} \tag{2.10}$$

The halo mass function (units: $\mathrm{h^4\,cMpc^{-3}\,M_\odot^{-1}}$) is the differential halo number density per unit mass and is defined as:

$$\frac{dn}{dM}(z, M) = \frac{\bar{\rho}_{\text{m},0}}{M^2}\, f(\sigma(z, M)) \left| \frac{d \ln \sigma(z, M)}{d \ln M} \right|. \tag{2.11}$$

Here $\bar{\rho}_{\text{m},0}$ (units: $\mathrm{h^2\,M_\odot\,cMpc^{-3}}$) and $\sigma(z, M)$ refer to the mean density of the Universe and mass variance respectively. The exact form of $f(\sigma(z, M))$ depends on the choice of fitting function for the halo mass function.

The mass variance is given as:

$$\sigma^2(z, M) = \frac{1}{2\pi^2} \int_0^\infty k^2\, P(z, k)\, \tilde{W}^2(kR(M))\, dk, \tag{2.12}$$

where $P(z, k)$ is the linear power spectrum and $\tilde{W}(kR)$ is a window function with a filter defined by $R = R(M)$. We use the Top Hat window function given as:

$$\tilde{W}(kR) = \frac{3}{(kR)^3} \left[\sin(kR) - (kR)\cos(kR)\right], \tag{2.13}$$

$$W(r) = \begin{cases} \frac{3}{4\pi R^3} & \text{if } r \leq R \\ 0 & \text{if } r > R. \end{cases} \tag{2.14}$$

The linear power spectrum evolves with z as:

$$P(z, k) = d(a(z))^2 \, P(z = 0, k), \tag{2.15}$$

where $a(z) = 1/(1 + z)$ and $d(a)$ is the normalised linear growth factor (Lukić et al. (2007)) given as:

$$d(a) = \frac{D^+(a)}{D^+(a = 1)}, \tag{2.16}$$

$$D^+(a) = \frac{5\Omega_{\mathrm{m},0}}{2} \frac{H(a)}{H_0} \int_0^a \frac{da'}{[a'H(a')/H_0]^3}. \tag{2.17}$$

The exact form of $P(z = 0, k)$ depends on the cosmology and the choice of transfer function. Like with our simulations, we initialise the `hmf` objects with the Eisenstein & Hu (1998) transfer function with no baryon acoustic oscillations.

Press-Schechter Theory

In Press & Schechter (1974) (PS), a spherical collapse model is assumed for dark matter halos and the probability of reaching a threshold density field value follows a Gaussian distribution. Thus the fitting function for PS is given as:

$$f_{\mathrm{PS}}(\sigma) = \sqrt{\frac{2}{\pi}} \frac{\delta_{\mathrm{c}}}{\sigma} \exp\Big(- \frac{\delta_{\mathrm{c}}^2}{2\sigma^2} \Big), \tag{2.18}$$

where $\delta_{\mathrm{c}} \approx 1.686$ is the critical overdensity required for a region to spherically collapse into a dark matter halo. A limitation of the PS fitting function is its tendency to overestimate the number of lower-mass halos and underestimate the number of higher-mass halos compared to N-body simulations (Lacey & Cole (1994), Sheth & Tormen (1999)). Since this seminal paper, many other fitting functions have been developed that aim to correct for this discrepancy as well as attempting to add additional sophistication to the modelling. In this work, we explore four other halo mass fitting functions in addition to PS.

Sheth, Mo & Tormen and Beyond

The Sheth et al. (2001) (SMT) halo mass function has a similar form to PS but assumes ellipsoidal collapse and is given as:

$$f_{\mathrm{SMT}}(\sigma) = A\sqrt{\frac{2a}{\pi}} \left[1 + \left(\frac{\sigma^2}{a\delta_{\mathrm{c}}^2} \right)^p \right] \frac{\delta_{\mathrm{c}}}{\sigma} \exp\left(-\frac{a\delta_{\mathrm{c}}^2}{2\sigma^2} \right), \tag{2.19}$$

where $A = 0.3222$, $a = 0.707$ and $p = 0.3$. We also test fitting functions developed by Reed et al. (2007) (Reed07) and Watson et al. (2013) (WatsonFoF refers to a fit using the Friends-of-Friends halo finder, WatsonSO refers to a fit using the Spherical Overdensity halo finder). The PS and SMT fits are widely-used and based on an analytical formalism, with no restriction on redshift or halo mass range. The Reed07, WatsonFoF and WatsonSO fits are based on simulation results, all with a redshift range of $z \in (0, 30)$ and no explicit restriction on halo mass (see Table 2.4). While many other halo mass fitting functions exist, we choose these fits as they were all calibrated across the redshift range of interest to us (i.e. $z > 10$). Other fitting functions are typically calibrated for lower redshifts.

Fitting function	z range	Reference
PS	No limit	Press & Schechter (1974)
SMT	No limit	Sheth et al. (2001)
Reed2007	0 - 30	Reed et al. (2007)
WatsonFoF	0 - 30	Watson et al. (2013)
WatsonSO	0 - 30	Watson et al. (2013)

Table 2.4: The fitted halo mass functions we use to compare to HMFs derived from numerical simulations.

We use the Python package `hmf` to compute halo number densities derived from the HMFs described above.

2.3 Results

As previously stated, the goal of this work is to compare halo number densities derived from simulation results with those derived from popular fits, and to test how well the fits can predict JWST halo mass abundances compared to simulations (e.g. Boylan-Kolchin, 2023).

In Figure 2.2, we compare the HMFs from `Enzo` and `SWIFT` data (dashed lines) with the chosen fits (solid lines) for $z = 20.0$, $z = 15.0$ and $z = 10.0$ using the FOF halo finder. The black rectangles indicate the high mass range depicted in more detail in Figure 2.3. The range of halo masses selected in the black rectangles is bounded by the approximate least massive halos which would host galaxies that are detectable by JWST at these epochs up to the most massive halo masses accessible by the numerical simulations at that redshift. This is only possible for our outputs at $z = 10.0$ and $z = 15.0$ as galaxy (and indirectly halo) masses large enough to be observed (except perhaps via extreme lensing) by JWST are simply not formed by $z = 20.0$ in a ΛCDM universe. Hence, we focus our analysis on the

$z = 15.0$ and $z = 10.0$ outputs in particular.

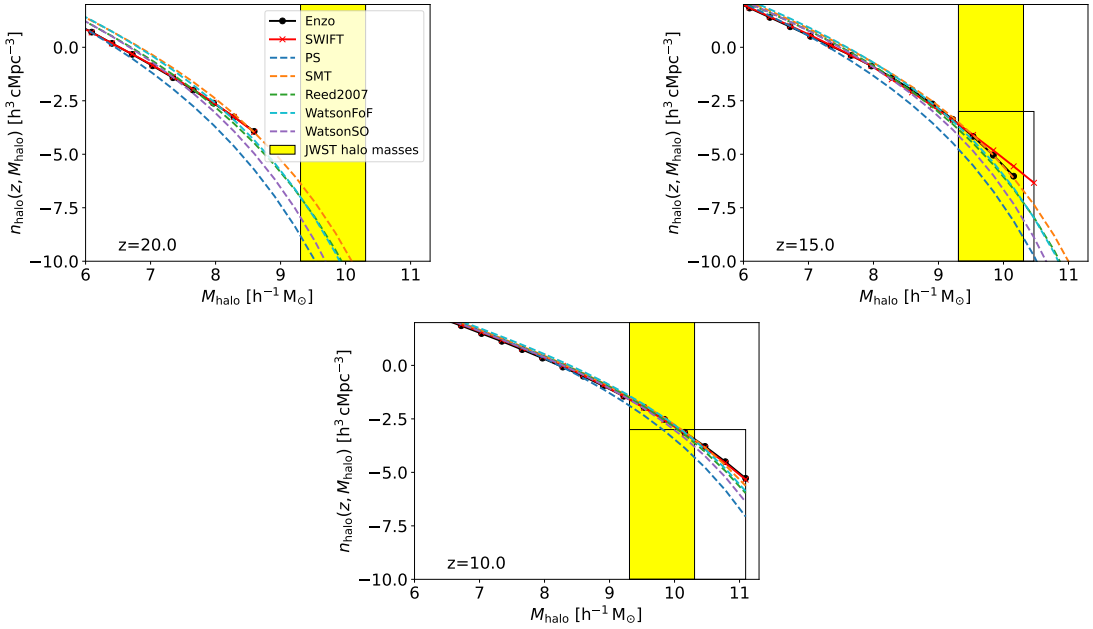

Figure 2.2: Comparing the `Enzo` and `SWIFT` halo number densities with five halo number densities derived from fits (see Table 2.4) at $z = 20.0$ (upper left panel), $z = 15.0$ (upper right panel) and $z = 10.0$ (lower panel) using the FOF halo finder (with halo masses and number densities on a logarithmic scale). The black rectangles indicate the regions for more detailed analysis as seen in Figure 2.3. The yellow shaded regions represent the approximate range of halo masses hosting galaxies detected by JWST at $z \geq 10.0$. Over the halo mass range selected at $z = 10.0$, all but the PS fit agree with numerical results within a factor of 2.

Overlaid onto Figures 2.2 to 2.5 are yellow rectangles which act as a visual aid, depicting an estimate for the range of halo masses that host recently-observed JWST galaxies and galaxy candidates. We choose sources with $10.0 < z < 15.0$ [2] and with an estimate of M_* or $M_{\rm halo}$ available. These sources include GN-z11 (Scholtz et al., 2024), Maisie's Galaxy (Arrabal Haro et al., 2023), GS-z14 (Helton et al., 2025) and others (Chakraborty et al., 2024). If there exists no estimate of $M_{\rm halo}$ yet for a given source, we estimate it using the following equation:

$$M_{\rm halo}(z, M_*) = \frac{\Omega_{\rm m}(z)}{\Omega_{\rm b}(z)} \frac{M_*}{\epsilon_*}, \tag{2.20}$$

where we set the star formation efficiency parameter $\epsilon_* = 0.1$. The width of the yellow rectangle is determined by the minimum and maximum halo masses in our sample and does not vary with redshift due to the small number of sources.

In Figures 2.4 and 2.5, we take the ratios of the semi-analytic halo number densities against the `Enzo` and `SWIFT` outputs respectively to quantify the overall disagreements at $z = 10.0$ and $z = 15.0$. Over the full mass range, for both simulation suites and halo finders, we find the fits considered agree generally

[2] We use photometric redshift only if spectroscopic redshift is not yet available.

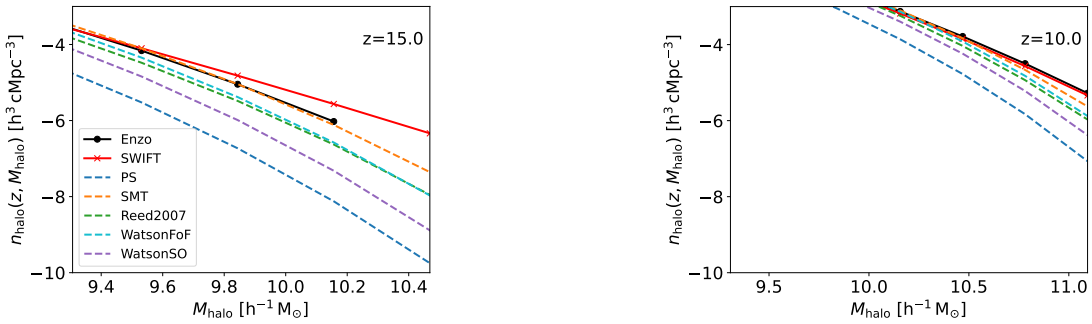

Figure 2.3: A zoom-in onto the black rectangles identified in Figure 2.2 (with halo masses and number densities on a logarithmic scale). These mass ranges represent the most massive halos accessible via numerical simulation at these redshifts. At this higher level of detail we see some discrepancy between the numerical halo mass functions of `Enzo` and `SWIFT` and their (semi-)analytical counterparts, particularly at $z = 15.0$. The ratio of each (semi-)analytic fit to numerical results is shown in Figure 2.4 and Figure 2.5.

within an order of magnitude of the numerical results, with the exception of the PS fit. The most favourable fits, SMT and WatsonFoF, agree within a factor of $\sim$ 2 for many mass ranges and redshifts. Additionally, the fits improve as redshift decreases - not just between the numerical results and the (semi-)analytic results but even among the (semi-)analytic fits themselves.

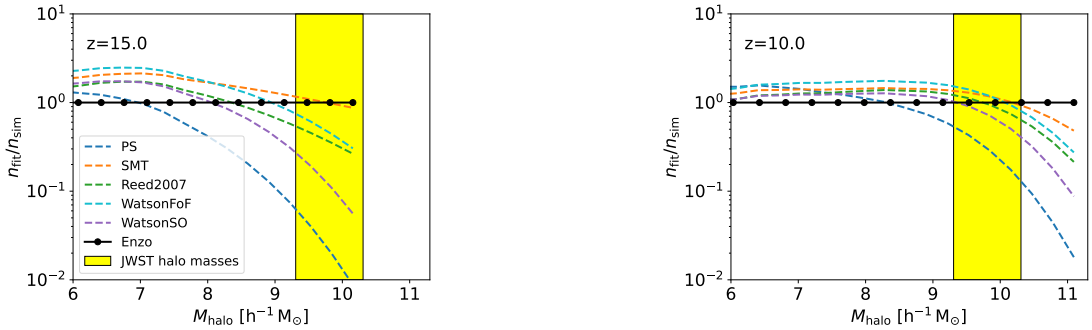

Figure 2.4: The ratios of the fitted halo number densities to the numerical halo number densities, derived from `Enzo` simulations and using the FOF halo finder (with halo masses on a logarithmic scale). Differences between the `Enzo` and the (semi-)analytical HMFs are typically less than a factor of two at $z = 10.0$, increasing to a factor of 5 at $z = 15.0$ (excluding the PS fit).

At the lower mass range (10^6 to 10^7 h^{-1} M$_\odot$), the semi-analytic fits overestimate the halo number densities by up to a factor of $\sim$ 2 compared to either `Enzo` or `SWIFT` data. At the mid-range masses (10^7 to 10^9 h^{-1} M$_\odot$) at $z = 10.0$, all but the PS fit overestimate the numerical simulations by less than a factor of 2. This is best illustrated by the right panels of Figures 2.4 and 2.5. For the same mass range at $z = 15.0$, there is a greater discrepancy with all but the SMT and WatsonFOF fits underestimating the halo number densities by up to a factor of $\sim$ 5 compared to numerical simulations (see the left panels of Figures 2.4 and 2.5).

In the JWST mass range, we see the greatest discrepancies. At $z = 15.0$, the

PS fit underestimates the Enzo halo number density by a factor of ~ 100 (see Figure 2.4 (left panel)). The other fits agree within a factor of ~ 50 (WatsonSO) in the worst case with the SMT fit providing the closest match by agreeing within a factor of ~ 2. We see a similar story at $z = 10.0$ with a less extreme discrepancy (PS underestimating by a factor of ~ 10, the other fits agreeing within a factor of ~ 2 (see Figure 2.4 (right panel))). This is consistent with the results and conclusions of Yung et al. (2024b).

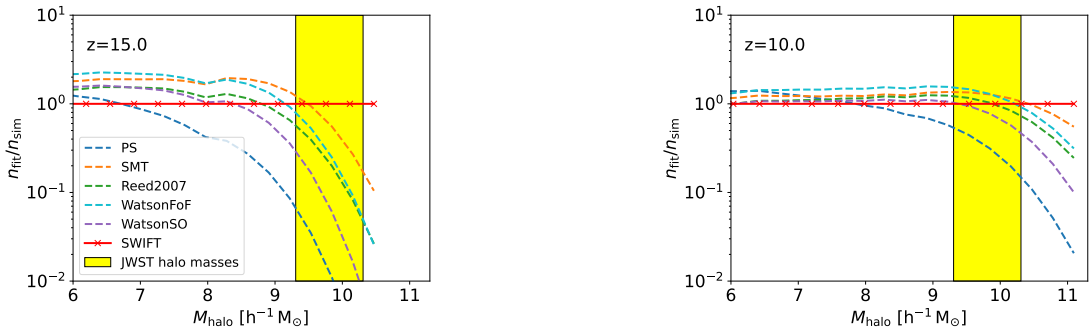

Figure 2.5: The ratios of the fitted halo number densities to the numerical halo number densities, derived from SWIFT simulations and using the FOF halo finder (with halo masses on a logarithmic scale). Similar to the Enzo result, SWIFT shows all fits except PS agreeing within a factor of ~ 2 for all but the highest masses at $z = 10.0$. There is a greater discrepancy present at $z = 15.0$, with some fits underestimating the numerical results by a factor of ~ 100 at the high-mass range.

For the SWIFT simulations at $z = 15.0$, we see a strong deviation towards higher masses which was not present for the Enzo simulations (see Figure 2.5 (left panel)). Both PS and WatsonSO underestimate the numerical halo number densities by a factor of ~ 100, and SMT agrees best within a factor of ~ 10. It appears here that the Enzo runs are better able to resolve halos at earlier times perhaps due to the inherent refinement strategy. A detailed analysis of the difference between the numerical codes is outside the scope of this study and comparisons in this direction have been undertaken in the past (e.g. O'Shea et al., 2005; Regan et al., 2007; Hayward et al., 2014). At $z = 10.0$, there is reasonable agreement between the numerical (SWIFT) results and the analytic fits (see Figure 2.5 (right panel)). The PS fit underestimates the numerical results by a factor of ~ 10, with the other fits generally agreeing within a factor of ~ 2.

In Figure 2.3 (right panel), we see a discrepancy between the Enzo and SWIFT results in the high-mass range at $z = 15.0$. Previous work (e.g. Warren et al., 2006; More et al., 2011) has shown that the FOF mass is sensitive to mass resolution and the presence of substructure, which will be strongly dependent on redshift and which is difficult to correct for in general. It will also depend on local clustering, which can lead to distinct structures being linked by bridges of particles. This is the most likely explanation for the variance between Enzo and SWIFT at $z = 15.0$. Note that this variance is absent from the HOP profiles (see Figure 2.7).

In summary, the agreement between the numerical N-body solvers and the (semi-)analytic fits depends both on the choice of fit and the redshift z. We find that the SMT fitting function provides the closest fit overall. With `Enzo`, there are deviations of at most a factor of ~ 2 at $z = 15.0$ (for low halo masses which host galaxies that are currently unobservable) and converging to much less than a factor of two within the JWST window at $z = 10.0$. For `SWIFT`, the agreement with SMT is equally excellent at $z = 10.0$ but deviates somewhat for the higher halo masses at $z = 15.0$. The WatsonFoF fitting function provides the second best fit overall while the other fitting functions deviate at worst by a factor of $\sim$100 at $z = 15.0$. These results suggest that both the SMT and WatsonFoF fits are the least likely to be a dominant source of error when testing high redshift observations against ΛCDM models.

2.4 Discussion

The recent explosion of data from the high-z Universe, particularly beyond $z = 10$, by JWST has led to a number of claims that the data is in tension with our galaxy formation and cosmological models (e.g. Boylan-Kolchin, 2023; Arrabal Haro et al., 2023; Yung et al., 2024b; Finkelstein et al., 2024). The Universe beyond $z = 10$ however is likely to be significantly different to the later and present-day Universe. At $z \gtrsim 10$, galaxies are still in their infancy, with the most massive galaxies at those epochs having stellar masses less than 10^{10} $M_\odot$ (these would be classified as dwarfs in the present-day Universe). Moreover, there is strong evidence that the astrophysical processes at play at $z = 10$ are sufficiently different to those of the present-day Universe and that they make significant alterations to the galaxy properties. This is particularly evident in galaxies like GN-z11 which is thought to harbour a massive black hole at its centre (Maiolino et al., 2024), moreover this galaxy contains species abundances which are difficult to explain through standard processes (e.g. Bunker et al., 2023; Cameron et al., 2023; Charbonnel et al., 2023; Nandal et al., 2024). This peculiarity and lack-of-understanding is not unique to GN-z11 with a number of galaxies displaying properties which has evoked confusion within the community (e.g. Maiolino et al., 2025). The most luminous galaxies observed by JWST remain in tension with state-of-the-art cosmological simulations (e.g. Keller et al. (2023)) with simulations struggling to model their extreme brightness at very early times. The reasons behind this are currently unknown but a greater emphasis on processes specific to the early Universe such as Pop III star formation and early black hole formation (e.g. McCaffrey et al. (2023)) may offer a pathway forward. It has also been argued that this tension may be resolved with the use of high-resolution simulations targeted at the high-redshift Universe (see McCaffrey et al. (2023)).

A key part of making progress in understanding the high-z Universe is therefore to identify sources of systematic error in our models at high-z. Some sources of uncertainty in counting galaxies at such redshifts include cosmic variance (especially significant at the distances considered), error in stellar mass estimation and the presence of backsplash halos (halos that have lost some dark matter from the host halo, giving the impression of a higher baryon-dark matter ratio). These uncertainties have been explored thoroughly by Chen et al. (2023). In this work we focus on exploring differences in fitting functions to the universal HMF and how they compare against direct N-body simulations at $z \geq 10$. In particular, we compare a wide range of fitting functions in use in the literature (see Table 2.4) against the adaptive mesh refinement code `Enzo` and against the N-body SPH code `SWIFT`.

We find that, for both `Enzo` and `SWIFT`, the match against the (semi-)analytic halo mass functions varies by fit, halo mass range and redshift z, with many fits agreeing with numerical results within a factor of ~ 2 for low and mid-range halo masses. The match against the standard Press & Schechter (1974) formalism is less accurate with deviations of up to an order of magnitude at $z = 10.0$ and over an order of magnitude at $z = 15.0$. Similarly, when comparing against other standard fitting formula (see Table 2.4), we again see good agreement with deviations typically within an order of magnitude up to $z = 15.0$ inside the window in which JWST can approximately observe high-z galaxies. The SMT and WatsonFoF fits provide the best agreements with numerical results by generally being within a factor of 2 even within the JWST mass window at $z = 15.0$ and $z = 10.0$. For the $z = 20.0$ snapshots, the (semi-)analytic results deviate from the numerical results by having significantly different power-law slopes from the `Enzo` or `SWIFT` results (see Figure 2.2 (upper left panel) and Figure 2.6 (upper panel)). Here, many of the (semi-)analytic fits overestimate the halo number densities compared to the numerical simulations, with the exception of the PS fit which underestimates the halo number densities. This suggests that there may be a calibration issue for these fits at higher redshifts. The power laws employed for these fits compare more favourably with numerical results at lower redshifts.

We caution that the spatial resolution employed, controlled via the softening parameter for `SWIFT` and via the level of maximum refinement with `Enzo`, is set relatively high for our simulations. For example, we use a softening length set to approximately the mean interparticle spacing divided by 25. This is slightly lower than the resolution we evolve the `Enzo` simulations with. This level of gravity resolution, specifically the softening length and spatial resolution here, is likely to be significantly higher than that used for typical galaxy formation simulations designed to run to $z \sim 0$ (e.g. Power et al., 2003, 2016; Zhang et al., 2019). It is also worth noting that the gravitational collapse of dark matter halos is sensitive

to the large-scale gravitational field, which in a numerical simulation depends on the size of the simulation volume. Previous work (e.g. Power & Knebe, 2006) has highlighted how the mass function is sensitive to simulation volume, with a deficit of halos of a given mass at high masses. This effect is most pronounced in studies of the mass function at high redshifts, where the necessary high mass resolutions and large simulation volumes make these simulations particularly challenging. We therefore caution the reader that matching the results from numerical simulations designed primarily for large-scale investigations may struggle to calculate the correct halo properties and abundances at $z \gtrsim 10$ (see e.g. Keller et al., 2023) unless the simulations are truly focused on high-z study (see e.g. McCaffrey et al., 2023).

Nonetheless, overall we find reasonable agreement between N-body simulations and both (semi-)analytic and fitting functions to HMFs, consistent with the results from Yung et al. (2024b), and that these functions (especially SMT and WatsonFoF) are unlikely to lead to large errors in our modelling of high-z host halos when appropriately modelled.

2.5 Alternative Halo Finding Techniques

In addition to the widely-used Friends-of-Friends halo finding algorithm, we also investigate how a different halo finder would impact our results. As discussed in §2.2 we also use the HOP halo finder (Eisenstein & Hut (1998)) in our analysis. In Figures 2.6 to 2.9, we reproduce Figures 2.2 to 2.5 from §2.3 respectively but with the halo finding technique switched to HOP instead of FOF.

Using the HOP halo finder, we find very similar results to the FOF method. We see a factor of ~ 2 to 3 difference between the HOP numerical results and the SMT and WatsonFoF fits in particular at both $z = 15.0$ and less than a factor of 2 at $z = 10.0$. At worst, the difference between HOP and the PS fitting function varies by a factor of 100.

We see little difference between FOF and HOP (see Figure 2.1) - a finding supported by other research studies (Knebe et al., 2011). However, as mentioned in §2.3, the use of the HOP halo finder appears to narrow the difference between the `Enzo` and `SWIFT` results themselves, particularly at $z = 15.0$ (see Figure 2.3 (left panel) and Figure 2.7 (left panel)). This may be due to how the FOF mass is computed within the simulations.

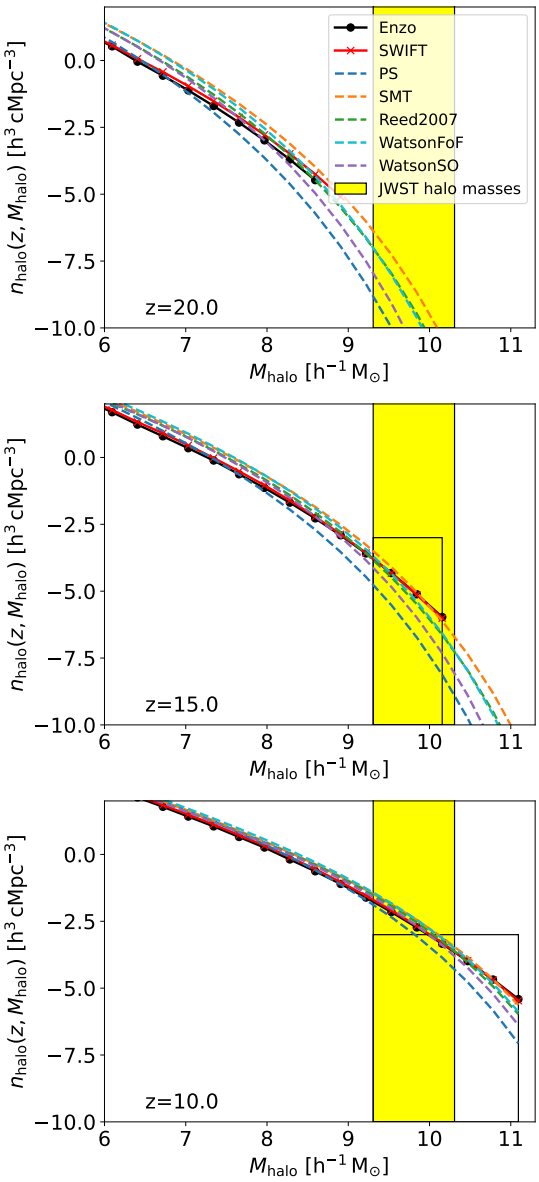

Figure 2.6: Comparing the `Enzo` and `SWIFT` halo number densities contrasted with 5 halo number densities derived from fits at $z = 20.0$ (upper left panel), $z = 15.0$ (upper right panel) and $z = 10.0$ (bottom panel) using the HOP halo finder (with halo masses and number densities on a logarithmic scale).

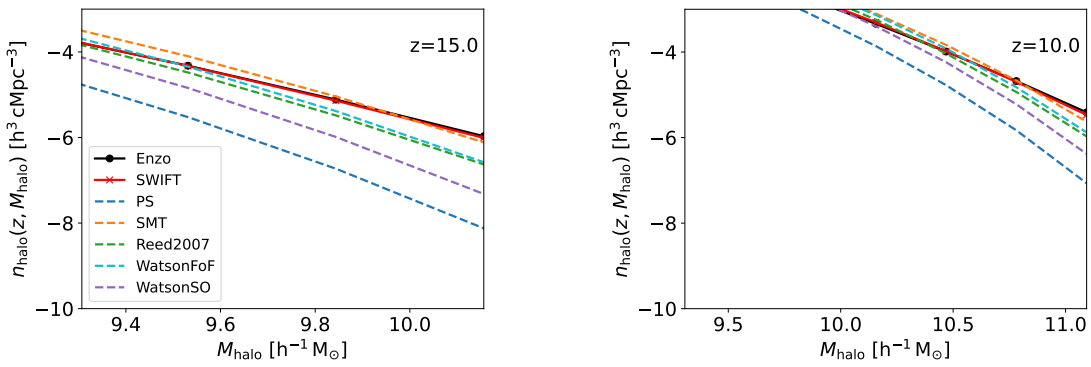

Figure 2.7: High-mass sections of Figure 2.6 (upper right and bottom panels) shown in more detail.

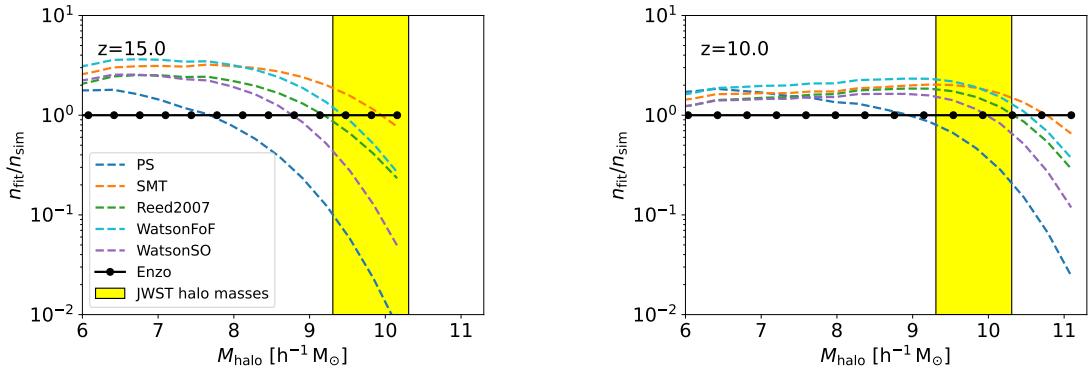

Figure 2.8: The ratios of the fitted halo number densities to the numerical halo number densities, derived from `Enzo` simulations and using the HOP halo finder (with halo masses on a logarithmic scale).

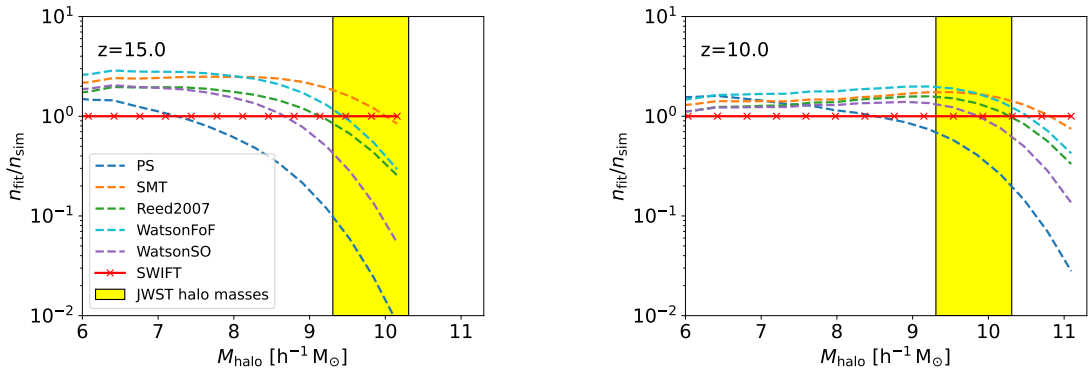

Figure 2.9: The ratios of the fitted halo number densities to the numerical halo number densities, derived from `SWIFT` simulations and using the HOP halo finder (with halo masses on a logarithmic scale).

Chapter 3

Predicting the Number Density of Heavy Seed Massive Black Holes due to an Intense Lyman-Werner Field

3.1 Introduction

Observations of high-z (i.e. $z \gtrsim 6$) quasars, with masses in excess of 10^8 $M_\odot$, indicate that the number density of such massive objects is approximately 1 per cGpc^3 (Bañados et al., 2018; Inayoshi et al., 2020). The origin of these high-z quasars poses a major challenge to our understanding of compact object formation and evolution in the early Universe. However, these extreme mass objects represent only the tip of the iceberg with smaller mass black holes likely being very much more abundant. Prior to the launch and subsequent observations of the James Webb Space Telescope (JWST), the number densities of this smaller mass population at high redshift could only be inferred from existing relations (Mortlock et al., 2011; Bañados et al., 2018; Matsuoka et al., 2019; Venemans et al., 2020; Wang et al., 2021; Yang et al., 2021; Izumi et al., 2021; Andika et al., 2022).

Recent observations of massive black holes (MBHs) with masses between 10^6 and 10^8 $M_\odot$ in the early Universe ($z \gtrsim 4$) have however started to indicate that the population of MBHs is potentially relatively high and certainly at the upper end of what theoretical models had previously suggested (e.g. Habouzit et al., 2016; Greene et al., 2020; Kokorev et al., 2023; Larson et al., 2023; Maiolino et al., 2024; Greene et al., 2024; Harikane et al., 2023). Significant uncertainties in determining the nature of a large population of so-called Little Red Dot (LRD) galaxies mean that it is too early, as of yet, to get clarity on the actual MBH population at high redshift (Lambrides et al., 2024; Li et al., 2025; Ma et al., 2025). Nonetheless, conservative estimates of the MBH population based on observations of LRDs indicate MBH number densities in excess of 10^{-4} cMpc^{-3} (e.g. Pérez-González

et al., 2024) (as opposed to a number density of approximately 10^{-9} cMpc^{-3} for the MBHs with masses in excess of 10^8 M$_\odot$).

The question then arises as to what is the formation process that drives the existence of this large population of MBHs? In this work we focus on the so-called heavy seed pathway, where the initial black hole has a mass in excess of 10^3 M$_\odot$(Regan & Volonteri, 2024). While it is possible that the entire population of MBHs originates from light seeds with initial masses of less than 10^3 M$_\odot$, we do not investigate that scenario here and instead direct interested readers to papers which investigate that channel (e.g. Madau & Rees, 2001; Alvarez et al., 2009; Madau et al., 2014; Lupi et al., 2016; Smith et al., 2018; Shi et al., 2024; Mehta et al., 2024).

For forming heavy seed MBHs, three mainstream (astrophysical) mechanisms have come to the fore which offer possible pathways to achieving the masses of this population within the required time-frame. All of the mechanisms we will discuss, except where we explicitly note, predict the formation of a super-massive star (SMS) as an intermediate stage and subsequently a transition into a MBH. This is often dubbed "Direct Collapse Black Hole (DCBH)" formation in the literature which is somewhat incorrect given the intermediate stage of stellar evolution which can, in theory, continue for ≥ 1 Myr. In fact, a more correct use of the DCBH terminology relates to the concept of the so-called "Dark Collapse" recently introduced into the literature by Zwick et al. (2023) and Mayer et al. (2025). We will therefore refrain from using the DCBH term here since we focus on the formation of massive stellar objects as precursors to MBH formation.

The first mechanism theorised to generate MBH seeds is through baryonic streaming velocities. Relative velocity differences between baryons and dark matter will arise following recombination (Tseliakhovich & Hirata, 2010). While the mean offset will be zero there will, nonetheless, be regions of the Universe where variations from the mean will exist. It is within these regions that the relative velocities can impact the early formation of structure. In particular, streaming motions can act to suppress star formation in the lowest mass halos, pushing the onset of star formation to higher mass halos and perhaps all the way up to the atomic-cooling limit (Naoz et al., 2012, 2013; Tanaka & Li, 2014; Latif et al., 2014b; Hirano et al., 2017; Schauer et al., 2017). In regions impacted by streaming velocities, the additional velocities of the baryons with respect to the dark matter means that baryons take additional time to settle in the halo centres, thus allowing the halo to grow in mass. Whether realistic streaming motions can truly allow halos to grow to the atomic-cooling limit without triggering star formation is unclear but it may be that the combination of streaming motions with a sufficiently intense Lyman-Werner (LW) flux (described below) may allow for this to occur (Kulkarni et al., 2021; Schauer et al., 2021).

The second mechanism is through the rapid growth of structure itself, be it the early rapid assembly of galaxies (Yoshida et al., 2003) or MBH formation triggered through mergers (Mayer et al., 2010, 2015; Zwick et al., 2023; Regan, 2023). In the case of early rapid assembly, halos below the atomic-cooling threshold experience rapid minor mergers and hence rapid growth. If the growth is particularly rapid then the heating caused by the dark matter inflows can offset the ability of H_2 to cool the gas effectively (Fernandez et al., 2014; Wise et al., 2019; Lupi et al., 2021). In this scenario normal metal-free (Population III; Pop III) star formation is delayed because the gas is unable to cool. Instead the halo continues to accumulate matter without forming stars. If the heating (i.e. rapid growth) is maintained then the halo can grow to the atomic-cooling limit where cooling by neutral hydrogen is triggered and star formation occurs regardless. However, having cooling commence at this mass scale offers the opportunity for SMS formation to occur as the gravitational potential is now sufficiently deep to enable this mechanism (e.g Regan et al., 2020; Latif et al., 2022; Regan, 2023).

In addition to this pathway, the related pathway of major mergers can drive huge gas inflows directly into the centres of merging halos. The large gas inflows can in some cases initiate a dark collapse through the formation of a super-massive disk (Zwick et al., 2023) and ultimately the direct formation of a MBH (Mayer et al., 2010, 2024). While the investigations of Mayer et al. (2024) focused on very massive objects and the formation in particular of high-z quasars, it is likely that this mechanism also acts on smaller mass scales, leading to the formation of a population of high-z MBHs with masses closer to the expected MBH seed masses (Regan, 2023).

The final mechanism and the one we will focus on in this Chapter is driven by local sources of LW radiation. LW radiation is emitted by stars and is composed of radiation below the hydrogen ionisation edge at photon energies between 11.2 and 13.6 eV. In order to form a Pop III star, the gas within a mini-halo[1] must cool down to $T_{gas} \approx 200$ K, allowing the gas to achieve the required densities and pressures to ignite star formation. Sufficiently intense LW radiation works against this process by dissociating H_2, thus removing (or at least suppressing) a critical coolant required for star formation to take place. In the primordial Universe, the formation of H_2 takes place via two possible routes (Galli & Palla, 1998). The first is through the radiative association of H and H^+ below i.e. the H_2^+ channel:

$$\begin{aligned} H + H^+ &\rightarrow H_2^+ + \gamma, \\ H_2^+ + H &\rightarrow H_2 + H^+. \end{aligned} \tag{3.1}$$

This reaction is only important at very high redshift ($z \gtrsim 365$) when $T_{CMB} > 10^3$

[1]We use the term mini-halo to refer to halos above $M_{halo} = 10^5$ $M_\odot$ and below the atomic-cooling threshold.

K and hence is less relevant for galaxy formation. The more relevant reaction is the associative detachment reaction of H and H^- i.e. the H^- channel which gives

$$\begin{aligned} H + e^- &\rightarrow H^- + \gamma, \\ H^- + H &\rightarrow H_2 + e^-. \end{aligned} \tag{3.2}$$

This is the critical reaction of H_2 formation in the high-z Universe relevant for galaxy formation and depends sensitively on the H^- abundances as well as the relic e^- fraction after recombination (Smith et al., 2008). In opposition to these formation pathways is LW radiation which can dissociate H_2. Radiation in the LW band excites electrons in the H_2 molecule, breaking the molecule down into its constituent atoms as such:

$$H_2 + \gamma_{LW} \rightarrow H_2^* \rightarrow H + H, \tag{3.3}$$

where initially the LW photons excite electrons in the H_2 molecule into an excited state from where they can decay with some probability into two hydrogen atoms. Crucially by removing the (inefficient) coolant H_2, the gas cannot cool and hence star formation is suppressed until the halo reaches the atomic-cooling limit, allowing the gas to cool and condense via neutral hydrogen transitions.

The intensity of LW radiation required to achieve full star formation suppression in mini-halos has been well-studied over the past decade. The consensus is that, while there is some spectral dependence on the critical flux of LW radiation required, values of at least 300 J_{21} are required for a $T \gtrsim 10^4$ K spectrum (e.g. Latif et al., 2014a; Regan et al., 2017) while values of as high as 1000 J_{21} may be required for a spectrum composed of Pop III stars only (i.e. $T\sim 10^5$ K spectrum) (Agarwal & Khochfar, 2015; Agarwal et al., 2016) (where $J_{21} = 10^{-21}\,\mathrm{erg\,s^{-1}\,Hz^{-1}\,sr^{-1}\,cm^{-2}}$). The value of the LW flux required is then known as the critical flux, $J_{\rm crit}$. The question then becomes under what circumstances can a LW flux greater than $J_{\rm crit}$ be achieved in practice? The goal of this work is to re-examine the methodology introduced by Dijkstra et al. (2008); Dijkstra et al. (2014) (hereafter D08 & D14) while also augmenting the models with data from the `Renaissance` (Chen et al., 2014; O'Shea et al., 2015; Xu et al., 2016a) simulation suite. Finally, we also compare the LW-only channel against more recent estimates of MBH heavy seed number densities through other channels (e.g. Trinca et al., 2022; McCaffrey et al., 2025). Using these combined results, we put tight limits on the number density of MBH seeds formed via LW feedback only and critically examine how viable the LW-only pathway is in the face of recent JWST observations.

The structure of the Chapter is as follows: In §3.2, we outline the methodology including the model from D14 and the relevant output post-processed from `Renaissance`. In §3.3, we deliver the results of our analysis, showing an updated

heavy seed number density plot. In §3.4, we summarize and discuss our results in light of recent JWST observations and other models in the literature.

3.2 Methodology

In this section, we detail our application of the heavy seed formation model used by D08 and D14. In §3.2.1, we describe the conditions a halo must meet to potentially host a heavy seed. In §3.2.2, we introduce the `Renaissance` simulations and how we post-process the data to supplement the fiducial (analytic-only) model. In §3.2.3, we define the halo mass function and how we use it to compute the halo number density. In §3.2.4, we discuss the impact of metal pollution, both from merger history and from neighbouring galaxy outflows. Finally, in §3.2.5, we show how the supercritical LW probability is computed, both in the fiducial model and one informed by `Renaissance` data.

3.2.1 Formation of Heavy Seeds

Here we refer to heavy seeds as MBH seeds that have initial masses $\geq 10^3$ $M_\odot$, as opposed to light seeds with initial masses $< 10^3$ $M_\odot$. We find the heavy seed number density $n_{\text{heavy seeds}}(z)$ (units: cMpc^{-3}) as a function of redshift z ($10 \leq z \leq 30$) by computing the number density of dark matter halos which meet the criteria to host heavy seeds (assuming one heavy seed forms per host halo). For the purpose of this study, the dominant criteria is the impact of a LW radiation field as discussed in §3.1 and in detail below.

Consider a potential host halo of mass M_{target} at redshift z (see Figure 3.1). It is surrounded by neighbouring dark matter halos of various masses, M, and physical separations, r. At this high-redshift range, the comoving distance from an observer on Earth to such a host halo is ≥ 9 cGpc (at $z = 10.0$, the proper distance would be $\gtrsim 800$ Mpc). We are considering physical separations between the host halo and its neighbours of $\lesssim 10$ Mpc. Since these separations are negligible compared to the proper distances from Earth, we approximate the neighbouring halos as having the same redshift as the potential host.

To form light seeds within a halo, baryonic gas would cool and fragment to form stars which would later collapse into stellar black holes if the progenitor stellar mass $M_* \gtrsim 25\,M_\odot$ (see Figure 1 of Heger et al. (2003)).[2]. Thus to reduce fragmentation and the formation of light seeds (forming heavy seeds instead), the temperature of the gas within the target halo must remain high ($T_{\text{gas}} \gtrsim 8000$ K). This can be achieved if the target halo meets the following criteria:

[2]At time of writing, it is still not clear whether there is a mass gap between the most massive neutron stars (≈ 2 $M_\odot$, Tolman-Oppenheimer-Volkoff limit (Heger et al., 2003)) and a minimum stellar black hole mass (≈ 5 $M_\odot$) (Farr et al., 2011; Kreidberg et al., 2012; Abbott et al., 2019).

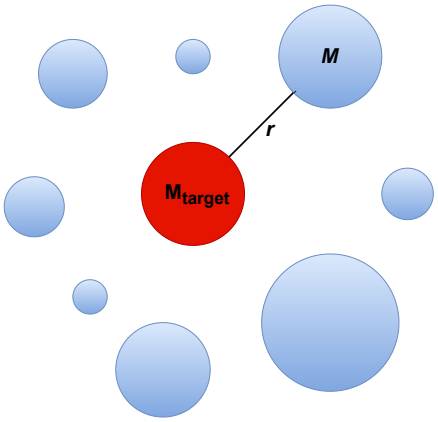

Figure 3.1: Target halo surrounded by neighbouring halos of various masses and physical separations. Here M refers to the mass of a given neighbouring halo, r is the physical separation between the neighbouring halo and the (central) target halo. The central target halo is later defined as having a mass $\mathrm{M_{target}} = \mathrm{M_{min}}(z)$ which is exactly equivalent to the virial mass of a halo at redshift z with temperature $\mathrm{T_{vir}} = 10^4$ K.

1. it is massive enough for the gas to cool via atomic hydrogen only;
2. it is chemically pristine i.e. free from metal enrichment;
3. it receives sufficient LW radiation from within its neighbours to suppress H_2 cooling.

The number density of dark matter halos (units: $\mathrm{cMpc^{-3}}$) meeting these criteria (and thus the heavy seed number density) is described as:

$$n_{\text{heavy seeds}}(z) = \int_{\mathrm{M_{min}}(z)}^{\infty} d\mathrm{M_{target}} \frac{dn_{\mathrm{SMT}}}{dM}(z, \mathrm{M_{target}}) \times P_{\text{pristine}}(z)\, P_{\mathrm{LW}}(z, \mathrm{M_{target}}). \tag{3.4}$$

We now briefly define each term in the above integral. We integrate over $\mathrm{M_{target}}$, the mass of a halo that is a potential heavy seed (or equivalently MBH) formation site. Here $\mathrm{M_{min}}(z)$ is the minimum mass where the virial theorem is satisfied with $\mathrm{T_{vir}} = 10^4$ K (Barkana & Loeb, 2001) i.e. the atomic-cooling limit and is given as:

$$\mathrm{M_{min}}(z) = 4 \times 10^7 \left(\frac{1+z}{11}\right)^{-3/2} \mathrm{M_\odot}. \tag{3.5}$$

We integrate the halo mass function $\frac{dn_{\mathrm{SMT}}}{dM}(z, \mathrm{M_{target}})$ (units: $\mathrm{M_\odot^{-1}\ cMpc^{-3}}$) to find the number density of halos greater than or equal to the atomic-cooling limit. The halo mass function gives the number of halos per comoving volume per unit mass. It was originally derived analytically in a seminal paper by Press & Schechter (1974). In this work we use the semi-analytic form from Sheth et al. (2001) (SMT) which assumes ellipsoidal halo collapse (as opposed to the idealised spherical collapse assumed by Press & Schechter (1974)). We implement it using

the Python package `hmf`, developed by Murray et al. (2013).

The quantity $P_{\text{pristine}}(z)$ refers to the probability of a target halo being pristine i.e. free from metal pollution. In §3.2.4, we discuss both the model used by D14 and one derived from `Renaissance` data and refer to the derived probabilities as $P_{\text{pristine, fid.}}(z)$ and $P_{\text{pristine, Ren.}}(z)$ respectively. $P_{\text{pristine, fid.}}(z)$ accounts only for metal pollution inherited via merging episodes and is based on previous work by Trenti & Stiavelli (2007); Trenti & Stiavelli (2009). This involves tracking Pop III star formation by noting how the minimum halo mass where H_2 cooling may occur, $M_{H_2}(z, J_{\text{bg}})$, varies as a function of redshift z and LW background flux J_{bg}. $P_{\text{pristine, Ren.}}(z)$ accounts for both inherited metal pollution and metal enrichment via supernovae outflows from neighbouring halos and does not distinguish between the two.

Finally, a given target halo receives LW radiation from its neighbours (which dissociates H_2) but also metal outflows from supernovae (which act as a coolant). If the target halo receives a total LW flux exceeding a threshold flux ($J > J_{\text{crit}}$), it is a candidate for heavy seed formation due to the sufficient dissociation of H_2. The quantity $P_{\text{LW, fid.}}(z, \text{M}_{\text{target}})$ refers to the probability of a target halo at redshift z and of mass M_{target} receiving supercritical LW radiation while also avoiding metal outflows from its neighbouring halos in the fiducial model. The analogous quantity $P_{\text{LW, Ren.}}(z, \text{M}_{\text{target}})$ refers only to supercritical LW radiation as metal outflows are accounted for by $P_{\text{pristine, Ren.}}(z)$ (see §3.2.4 for more detail). In this model, J_{crit} is a parameter and we evaluate the supercritical probability, and subsequently the heavy seed number density, at $J_{\text{crit}} = 300$ and 1000 J_{21}. This probability is highly dependent on the form of the mean LW luminosity density $\langle L_{\text{LW}}(z, M)\rangle$. We investigate both the form described by D14 and one derived from `Renaissance` data, referred to as $\langle L_{\text{LW, fid.}}(z, M)\rangle$ and $\langle L_{\text{LW, Ren.}}(z, M)\rangle$ respectively.

We describe each of the terms in Eq. 3.4 in greater detail in §3.2.3, §3.2.4 and §3.2.5 below. Our cosmology is similar to that used by D14: $n_{\text{s}} = 0.9624$, $\text{h} = 0.6711$, $\Omega_{\text{m,0}} = 0.317512$, $\Omega_{\text{b,0}}\text{h}^2 = 0.022069$, $\Omega_{\Lambda} = 0.682433$, $\Omega_{\text{r,0}} = 0.000055$ and $\sigma_8 = 0.8344$. The impact of a specific cosmology on our model is however likely to be minimal. Note that we use units with factors of h when performing calculations. This is to be consistent with units used in `hmf`[3] and `halomod`[4], two Python packages that we use to compute the halo mass function, power spectrum and halo bias factor (Murray et al., 2013; Murray et al., 2021). Our final results in Figure 3.7 have been converted to units without factors of h.

[3]hmf: https://pypi.org/project/hmf/1.6.2/
[4]halomod: https://github.com/halomod/halomod/

3.2.2 `Renaissance` Simulations

The `Renaissance` simulations (Xu et al., 2013, 2014; Chen et al., 2014; O'Shea et al., 2015; Smith et al., 2018; Wise et al., 2019) were run using the massively parallel adaptive mesh refinement `Enzo` code (Bryan et al., 2014; Brummel-Smith et al., 2019). We briefly describe the `Renaissance` suite here, but refer the interested reader to the previous papers for a more complete discussion. The `Renaissance` simulation suite is composed of three zoom-in regions extracted from a parent volume of $(40\ \mathrm{cMpc})^3$. The three separate zoom-in regions were named the *Rarepeak* (RP) region, the *Normal* region and the *Void* region. Each volume was smoothed on a scale of 5 cMpc, with the RP region corresponding to a mean overdensity of $\langle\delta\rangle \equiv \frac{\langle\rho\rangle}{\Omega_{\mathrm{m}}\rho_{\mathrm{c}}} - 1 \sim 0.68$ and the *Normal* region corresponding to $\langle\delta\rangle \equiv \frac{\langle\rho\rangle}{\Omega_{\mathrm{m}}\rho_{\mathrm{c}}} - 1 \sim 0.09$. The RP and *Normal* subregions have volumes of 133.6 and 220.5 cMpc^3 respectively. They were re-simulated with an effective initial resolution of 4096^3 grid cells and particles within the central, most refined regions, and have a particle mass resolution of $2.9 \times 10^4\ \mathrm{M}_\odot$. In addition to the initial nesting procedure, which allows the RP and *Normal* regions to be selected, up to 8 further levels of refinement are allowed, giving a total maximum spatial resolution of ≈ 19 cpc. For this study we focus on the *Normal* region only since it is a representative volume of mean cosmic density. This is potentially quite conservative since it is less likely to find high values of $P_{\mathrm{LW}}(z, J_{\mathrm{crit}})$ within *Normal* regions. We make this choice since the alternatives (RP and *Void*) would be difficult to relate to observations.

From `Renaissance` we can compare some of the key characteristics of the D14 model against simulation datasets in order to test the veracity of some of the key underlying assumptions of the model. Considering again Eq. 3.4, we see that calculating the number density depends on the halo mass function, the probability of a halo receiving supercritical flux and the probability of a halo remaining pristine. From `Renaissance` the key quantities that can be extracted are the mean LW luminosity densities $\langle L_{\mathrm{LW,\ Ren.}}(z, M)\rangle$ as a function of redshift and neighbouring halo mass and the pristine fraction of halos $P_{\mathrm{LW,\ Ren.}}(z, \mathrm{M}_{\mathrm{target}})$ as a function of redshift and target halo mass.

Note that while previous works (see e.g. Smith et al. (2018); McCaffrey et al. (2025)) showed that `Renaissance` post-processed black holes struggled to grow to heavy seed scales i.e. $M_{\mathrm{BH}} \sim 10^5\ \mathrm{M}_\odot$, we are only interested in halos themselves as hosts whose environment fits the criteria to later form heavy-seed black holes. We do not investigate the later growth and dynamics of these black holes in this study.

However, we begin our analysis by examining the halo mass function, which is the main driver of the number of heavy seeds. We then move onto the pristine fraction (where `Renaissance` will play a role) and the probability of a halo

receiving a super-critical flux (where again `Renaissance` will play a role).

3.2.3 Halo Mass Function

In Figure 3.2, we show how the halo mass function varies with halo mass ($10^7\,\mathrm{h}^{-1}\,\mathrm{M}_\odot \leq \mathrm{M}_{\mathrm{target}} \leq 10^{10}\,\mathrm{h}^{-1}\,\mathrm{M}_\odot$) at a number of fixed redshifts. More massive halos become significantly rarer at all redshifts, with the higher redshifts showing increased rarity of high mass halos as expected in a ΛCDM cosmology. The halo mass function is relatively well calibrated against N-body simulations at lower redshifts but can differ from N-body runs at high-z by up to an order of magnitude (for a discussion on this point see Yung et al., 2024a; O'Brennan et al., 2024). However, for the halo masses which we are concerned with here (i.e. close to the atomic-cooling limit) the differences are approximately a factor of two and we do not investigate systematic differences due to the halo mass function here.

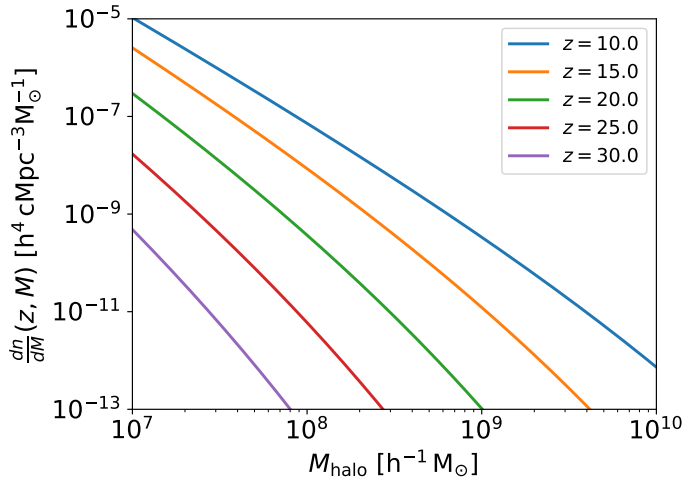

Figure 3.2: Halo mass function vs. halo mass at a number of redshifts. The lines shown here are generated using the `hmf` package developed by Murray et al. (2013). We use the SMT halo mass function and the modified Planck13 cosmology (used also by D14). The rarity of halos in a given mass range increases with increasing redshift.

Since the halo mass function decreases by several orders of magnitude with increasing halo mass, we approximate Eq. 3.4 as:

$$\begin{aligned} n_{\text{heavy seeds}}(z) \approx & \left[\int_{\mathrm{M}_{\mathrm{min}}(z)}^{\infty} d\mathrm{M}_{\mathrm{target}} \frac{dn_{\mathrm{SMT}}}{dM}(z, \mathrm{M}_{\mathrm{target}})\right] \\ & \times P_{\mathrm{pristine}}(z)\, P_{\mathrm{LW}}(z, \mathrm{M}_{\mathrm{min}}(z)), \end{aligned} \tag{3.6}$$

$$\begin{aligned} n_{\text{heavy seeds}}(z) \approx & \; n_{\mathrm{halo}}(\mathrm{M}_{\mathrm{target}} > \mathrm{M}_{\mathrm{min}}(z)) \\ & \times P_{\mathrm{pristine}}(z)\, P_{\mathrm{LW}}(z, \mathrm{M}_{\mathrm{min}}(z)), \end{aligned}$$

i.e. when computing P_{LW} in §3.2.5, we approximate all potential formation sites

at some redshift z as having a fixed mass of $\mathrm{M_{target}} = \mathrm{M_{min}}(z)$.

3.2.4 Metal Pollution

Metal pollution can come in two forms. Firstly it can be inherited "genetically" through the hierarchical assembly process and secondly it can come from outflows from neighbouring halos. For the fiducial (analytic-only) model these two forms are computed separately, while for the model where we additionally use `Renaissance` data we simply calculate the halo metallicity (or more precisely the probability of a halo being metal-enriched via mergers or outflows from neighbours).

Genetic Metal Pollution

Starting with the fiducial model: consider a target halo at redshift z with mass $\mathrm{M_{target}}$. During previous episodes of halo merging, this target halo may have had a progenitor halo that became metal-enriched via supernova outflows from Pop III stars. If so, then the target halo would inherit this metal pollution i.e. genetic metal pollution. The quantity $P_{\text{gen, fid.}}(z)$ refers to the probability of the target halo being met with this genetic metal pollution i.e. it has a metal-enriched progenitor halo. The quantity $P_{\text{pristine, fid.}}(z) = 1 - P_{\text{gen, fid.}}(z)$ refers to the probability of the target halo avoiding this genetic metal pollution i.e. it does not have a metal-enriched progenitor halo.

In our fiducial model, as with D14, we base the form of $P_{\text{gen, fid.}}(z)$ on the model proposed by Trenti & Stiavelli (2007) (TS07) and Trenti & Stiavelli (2009) (TS09). TS07 investigated the formation of the first generation of Pop III stars within dark matter halos and tracked their descendant halos using a combination of `GADGET2` N-body simulations and a Monte Carlo method based on linear theory. Using these simulation results, TS09 found how $\mathrm{M_{H_2}}(z, J_{\mathrm{bg}})$ (units: $\mathrm{h^{-1}\ M_\odot}$) varied as a function of redshift z and LW background flux J_{bg}. $\mathrm{M_{H_2}}$ refers to the minimum mass where H_2 cooling may occur within a progenitor halo, and later Pop III star formation. The LW background flux J_{bg} is described in TS09 in their section 2 just before their Eq. (10) and by Eq. (18) and (19). It is used to compute $\mathrm{M_{H_2}}$, described by their Eq. (9), (12) and (13). From $z = 30$ to $z = 10$, J_{bg} ranges from $\sim 10^{-4}$ to 5 $\mathrm{J_{21}}$. Since TS09 found $J_{\mathrm{bg}}(z)$ as a function of z, $\mathrm{M_{H_2}}$ is strictly a function of z only. This mass $\mathrm{M_{H_2}}$ is plotted against redshift z in their Figure 1 (upper right panel). We could not verify these masses for $10 \leq z \leq 30$ but there may be subtleties in their model regarding Pop II and III star formation that we do not capture (see TS09 section 2.7).

Figure 3.3 (a recreation of TS09 Figure 1 (upper right panel) using the masses that TS09 found) shows how this mass increases by a factor of ≈ 30 as redshift decreases from $z \approx 20$ to $z \approx 10$. Conversely, the atomic-cooling limit $\mathrm{M_{min}}(z)$ increases only by a factor of ≈ 4 in the same redshift range and

$\mathrm{M_{min}}(z) < \mathrm{M_{H_2}}(z, J_{\mathrm{bg}})$ at $z \lesssim 13$. Thus a progenitor halo is more likely to cool via atomic hydrogen than H_2 at low redshifts.

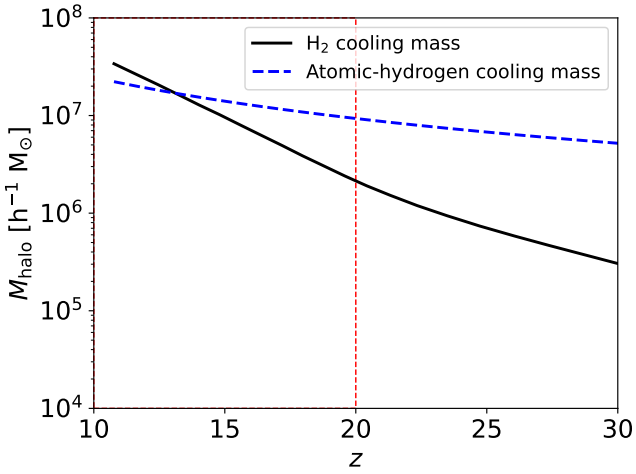

Figure 3.3: A recreation of Figure 1 (upper right panel) from Trenti & Stiavelli (2009). In this redshift range, the minimum halo mass for H_2 cooling to occur (solid black line) sharply increases as z decreases and is greater than the atomic-cooling limit (blue dashed line) at $z \lesssim 13$. The red dashed vertical line marks $z = 20$, the highest redshift considered by D14.

As a result, TS09 have shown that Pop III star formation is more likely to be delayed in the progenitor halo as redshift decreases. Subsequently the probability, $P_{\mathrm{gen,\ fid.}}(z)$, of a target halo having a metal-enriched progenitor decreases as redshift decreases (see the blue line of our Figure 3.4 for a recreation of TS09 Figure 1 (lower right panel)). TS09 found that $P_{\mathrm{gen}}(z = 20) \approx 0.9$ and $P_{\mathrm{gen}}(z = 10) \approx 0.1$.

We now look at metal enrichment in `Renaissance`. For the `Renaissance` halos, we select only halos above the atomic-cooling threshold mass, $\mathrm{M_{min}}$, and from the *Normal* region only. We show the probability of a halo being metal-enriched in `Renaissance`, $P_{\mathrm{enriched,\ Ren.}}(z)$, in Figure 3.4 as the orange line i.e. the fraction of halos found to be metal-enriched at a given redshift. Note that this metal enrichment is from both genetic pollution and external enrichment and hence direct comparisons should be treated with this in mind. We define a halo as metal-enriched if $Z \geq 10^{-16}$ $\mathrm{Z_\odot}$. At high redshifts ($z \gtrsim 18$), the metal-enriched fraction is zero due to the fact that there are no halos with masses in excess of $\mathrm{M_{min}}$ at that point in the simulation (sub)volumes. As structure formation evolves and halos accrete sufficient mass, then the first atomic halos are predominantly star-forming and metal-enriched and hence $P_{\mathrm{enriched,\ Ren.}}(z)$ is exceptionally high at $z \sim 18$. As more and more halos form, then the number (and fraction) of metal-enriched halos decreases substantially approaching 70% by the end of the simulation at $z \sim 10$. No turnover is seen but this is expected to occur as metal diffusion becomes more widespread over cosmic time. Note that the apparent sharp increase in $P_{\mathrm{enriched,\ Ren.}}$ from $z \approx 18$ to 17 in Figure 3.4 is likely noise due to small number statistics i.e. there are very few halos in this redshift range that

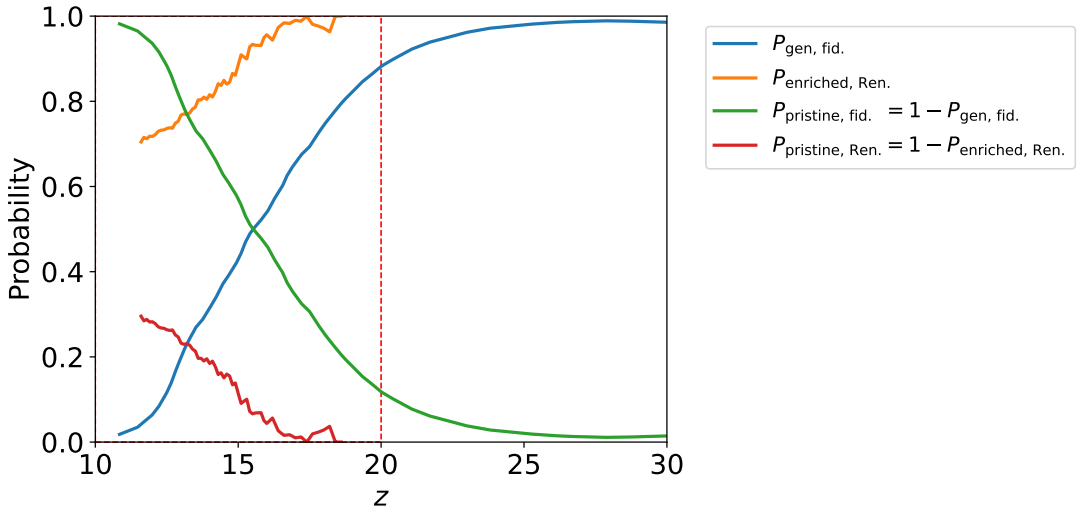

Figure 3.4: The probabilities $P_{\text{gen, fid.}}$, $P_{\text{enriched, Ren.}}$, $P_{\text{pristine, fid.}}$ and $P_{\text{pristine, Ren.}}$ as functions of redshift z. $P_{\text{gen, fid.}}$ (blue line) is the probability for genetic metal pollution to occur within a target halo with $\text{T}_{\text{vir}} = 10^4$ K and is a recreation of Figure 1 (lower right panel) from Trenti & Stiavelli (2009). From $z = 20$ to $z = 10$, $P_{\text{gen, fid.}}(z)$ sharply decreases i.e. a target halo at low redshift is less likely to have a metal-enriched progenitor halo. $P_{\text{enriched, Ren.}}$ (orange line) is the probability of a target halo with $M \geq M_{\text{min}}(z)$ being metal-enriched within the `Renaissance` simulation suite. This refers to both genetic and external metal pollution. $P_{\text{pristine, fid.}}$ (green line) and $P_{\text{pristine, Ren.}}$ (red line) are the complements of the probabilities described above. The dashed red line marks $z = 20$.

are massive enough to be counted in this analysis.

The `Renaissance` results are clearly deviant from the analytical models - likely due to the self-consistent treatment of structure formation and metal enrichment available to the hydrodynamic simulations. However, as noted already, we need to be somewhat careful here. Metal enrichment in the `Renaissance` halos can come from either genetic enrichment as well as external enrichment (via outflows from neighbouring galaxies). While we see a similar trend to the analytic models of TS07 and TS09, we clearly see that the hydrodynamical simulations predict higher values of (genetic and external) metal pollution than the analytic models. The green and red lines shows the same result, albeit inverted since we show the pristine fractions $P_{\text{pristine, fid.}}$ and $P_{\text{pristine, Ren.}}$ respectively (which are required each of our models). For the fiducial model, we address the issue of external metal enrichment in the next subsection.

Metal Pollution From Neighbouring halos

Within a neighbouring halo of mass M (units: h^{-1} $\text{M}_{\odot}$), massive stars eject metals as supernovae at the end of their lives. We approximate this phenomenon by assuming a fraction of stars within the halo enter their supernova phase simultaneously and there is a single physical radius of metal pollution $r_{\text{s}}(z, M, t)$

(units: h^{-1} Mpc) growing from the halo centre as t increases. It is given as:

$$r_{\mathrm{s}}(z, M, t) = \Big(\frac{E_0 \nu f_* \Omega_{\mathrm{b},0} M}{\rho_{\mathrm{gas}}(z) \Omega_{\mathrm{m},0}}\Big)^{1/5} t^{2/5}, \tag{3.7}$$

where $E_0 = 10^{51}$ erg is the supernova explosion energy, $\nu = 0.01\,\mathrm{M}_\odot^{-1}$ is the number of supernova per unit mass formed, and $\rho_{\mathrm{gas}}(z) = \Delta\Omega_{\mathrm{b},0}\rho_{\mathrm{c},0}(1+z)^3$ is the density of the ambient gas. We set our overdensity parameter to $\Delta = 60$. We assume that the beginning of the target halo collapse, the beginning of star formation within the neighbouring halo and the beginning of the neighbouring supernova phase occur simultaneously (at $t = 0$). The target halo must avoid metal pollution while $t < t_{\mathrm{ff}}(z)$ where $t_{\mathrm{ff}}(z)$ is the free-fall time of the target halo. In other words for a set redshift z and neighbouring halo mass M, the halo separation $r > r_{\mathrm{s}}(z, M, t = t_{\mathrm{ff}}(z))$ since r_{s} increases monotonically with t. When computing the heavy seed number density in the fiducial model, we include a Heaviside function $\Theta[r - r_{\mathrm{s}}(z, M, t_{\mathrm{ff}}(z))]$ to only include metal-free halos described above. Note that this is only necessary for the fiducial model. When modelling using the `Renaissance` data, we do not need to include the Heaviside function as this information is already contained as part of the pristine fraction of halos $P_{\mathrm{pristine,\ Ren.}}(z)$.

3.2.5 Supercritical Flux

Here we derive $P_{\mathrm{LW}}(z, \mathrm{M}_{\mathrm{target}})$ i.e. the probability of a target halo receiving supercritical LW radiation. Since we use the approximation described in Eq. 3.6, this probability is now a function of z only i.e. $P_{\mathrm{LW}}(z, \mathrm{M}_{\mathrm{target}}) = P_{\mathrm{LW}}(z, \mathrm{M}_{\mathrm{min}}(z)) = P_{\mathrm{LW}}(z)$. We compute this analytically by approximating that the LW flux received by the target halo is dominated by a single luminous nearby source. We integrate a probability density over LW flux J:

$$\begin{aligned} P_{\mathrm{LW,\ fid.}}(z) &= \int_{\log_{10} J_{\mathrm{crit}}}^{\infty} d\log_{10} J \, \frac{dP_{\mathrm{fid.}}}{d\log_{10} J}(z, J), \\ P_{\mathrm{LW,\ Ren.}}(z) &= \int_{\log_{10} J_{\mathrm{crit}}}^{\infty} d\log_{10} J \, \frac{dP_{\mathrm{Ren.}}}{d\log_{10} J}(z, J). \end{aligned} \tag{3.8}$$

Here J is in units of J_{21} and we integrate over the logarithmic value. The LW flux probability density is found by integrating over all possible masses (units: h^{-1} $\mathrm{M}_\odot$) and physical separations (units: h^{-1} Mpc) of neighbouring halos:

$$\frac{dP_{\rm fid.}}{d\log_{10} J}(z,J) = \int_{M_a}^{M_{b,\rm fid.}} dM \int_{r_{\rm min}(z,M)}^{r_{\rm max}(z)} dr \frac{d^2P}{dMdr}(z,M,r) \times \frac{dP}{d\log_{10} L}(\langle L_{\rm LW,\ fid.}(z,M)\rangle, J, r) \times \Theta[r - r_{\rm s}(z,M,t_{\rm ff}(z))],$$
$$\frac{dP_{\rm Ren.}}{d\log_{10} J}(z,J) = \int_{M_a}^{M_{b,\rm Ren.}} dM \int_{r_{\rm min}(z,M)}^{r_{\rm max}(z)} dr \frac{d^2P}{dMdr}(z,M,r) \times \frac{dP}{d\log_{10} L}(\langle L_{\rm LW,\ Ren.}(z,M)\rangle, J, r). \tag{3.9}$$

Here $\frac{d^2P}{dMdr}(z,M,r)$ (units: $\rm h^2\ M_\odot^{-1}\ Mpc^{-1}$) is the probability density used to count the number of neighbouring halos in a given mass-separation bin, we assign a LW luminosity to each halo using the probability density $\frac{dP}{d\log_{10} L}(\langle L_{\rm LW}(z,M)\rangle, J, r)$ and $\Theta[r - r_{\rm s}(z,M,t_{\rm ff}(z))]$ is a Heaviside function used to account for metal pollution via supernova outflows from a neighbouring halo in the fiducial model. Now we define each term in the integral over M and r below.

Counting the Neighbouring Halos

If the neighbouring halos were uniformly distributed in space, then the probability of finding a neighbouring halo with halo mass $[M, M + dM/2]$ and physical separation $[r, r + dr/2]$ from the target halo would be:

$$\frac{d^2P}{dMdr}(z,M,r)\,dMdr = 4\pi r^2 (1+z)^3 \frac{dn_{\rm SMT}}{dM}(z,M)\,dMdr. \tag{3.10}$$

Here $4\pi r^2\,dr$ is the physical volume of the shell surrounding the target halo, $\frac{dn_{\rm SMT}}{dM}(z,M)\,dM$ is the halo number per unit comoving volume and $(1+z)^3$ converts from it from comoving to physical volume. But this only holds for a comoving separation $r_{\rm co,\ max} \gtrapprox 100\,\rm cMpc$.[5] We must additionally account for dark matter clustering leading to deviations from the mean matter density $\bar{\rho}_{\rm m}$ at close range. We denote this deviation $\delta(z, r_{\rm co})$ by:

$$1 + \delta(z, r_{\rm co}) = \frac{\rho_{\rm m}(z, r_{\rm co})}{\bar{\rho}_m(z)}. \tag{3.11}$$

Rather than computing $\delta(z, r_{\rm co})$ directly, we find a related quantity: the dimensionless two-point halo-halo correlation function $\xi_{\rm hh}(z, \rm M_{min}(z), M, r_{co})$. This accounts for the excess probability of finding a neighbouring halo of mass M at a

[5] We computed this by finding $r_{\rm co,\ max}$ such that $\xi_{\rm mm} < 0$ for $r > r_{\rm co,\ max}$ and halos are no longer correlated.

comoving separation of $r_{\rm co}$ from our target halo of mass $\mathrm{M}_{\rm min}(z)$, both at redshift z. We can separate the M-dependence using the dimensionless halo bias terms $b(z, M)$ and the $r_{\rm co}$-dependence using the dimensionless two-point matter-matter correlation function $\xi_{\rm mm}(z, r_{\rm co})$ (van den Bosch et al., 2013):

$$\begin{aligned}\xi_{\rm hh}(z, \mathrm{M}_{\rm min}(z), M, r_{\rm co}) \approx b(z, \mathrm{M}_{\rm min}(z)) b(z, M) \\ \times \xi_{\rm mm}(z, r_{\rm co}).\end{aligned} \tag{3.12}$$

The redshift and mass dependence of the halo bias terms $b(z, M)$ are determined by a fitting function developed by Sheth et al. (2001). We can later relate physical and comoving separations by:

$$r = \frac{1}{1+z} r_{\rm co}. \tag{3.13}$$

The quantity $\xi_{\rm mm}(z, r_{\rm co})$ is found by taking the inverse Fourier transform of the nonlinear power spectrum $P(z, k)$ in spherical coordinates where we assume the power spectrum is spherically symmetric:

$$\xi_{\rm mm}(z, r_{\rm co}) = \frac{1}{2\pi^2} \int_0^\infty \mathrm{d}k\, k^2 P(z, k) \frac{\sin(k r_{\rm co})}{k r_{\rm co}}. \tag{3.14}$$

We note that the linear power spectrum $P(z, k)$ varies with z as:

$$P(z, k) = d(a(z))^2\, P(z = 10, k), \tag{3.15}$$

where $a(z) = 1/(1+z)$ and $d(a)$ is the normalised linear growth factor at $z = 10$ (Lukić et al. (2007)):

$$d(a) = \frac{D^+(a)}{D^+(a = 1/(1+10))}, \tag{3.16}$$

$$D^+(a) = \frac{5\Omega_{\rm m,0}}{2} \frac{H(a)}{H_0} \int_0^a \frac{da'}{[a' H(a')/H_0]^3}. \tag{3.17}$$

Thus we can approximate the redshift dependence of the matter-matter correlation function as:

$$\xi_{\rm mm}(z, r_{\rm co}) \approx d(a(z))^2\, \xi_{\rm mm}(z = 10, r_{\rm co}). \tag{3.18}$$

We create a fitting function based on arrays of $r_{\rm co}$ and $\xi_{\rm mm}(z = 10, r_{\rm co})$ values. This allows us to find $\xi_{\rm mm}(z, r_{\rm co})$ using Eq. 3.18, rather than computing it via integration as in Eq. 3.14 which is much more computationally heavy. For brevity, we shall refer to $\xi_{\rm hh}(z, \mathrm{M}_{\rm min}(z), M, r_{\rm co})$ as $\xi_{\rm hh}$. Finally, the probability of finding a neighbouring halo with halo mass $[M, M + dM/2]$ and physical separation

$[r, r + dr/2]$ is given by:

$$\frac{d^2P}{dMdr}(z, M, r)\, dMdr = 4\pi r^2(1+z)^3 \times \frac{dn_{\rm SMT}}{dM}(z, M)[1 + \xi_{\rm hh}]\, dMdr. \tag{3.19}$$

For the fiducial model, we integrate over the halo mass range $[M_a, M_{b,\rm fid.}] = [\mathrm{M_{min}}(z), 10^{15}\ \mathrm{M_\odot}]$. For the model informed by `Renaissance` data, we integrate over the range $[M_a, M_{b,\rm Ren.}] = [\mathrm{M_{min}}(z), 10^{9}\ \mathrm{M_\odot}]$ since no halos were found above this mass range for the redshifts considered ($11.6 \leq z \leq 18.6$). We define the minimum physical separation as $r_{\rm min}(z, M) = 2r_{\rm vir}(z, M)$ where $r_{\rm vir}$ is the virial radius of the neighbouring halo (Johnson (2012)). This avoids a neighbouring halo overlapping with the target halo.

$$r_{\rm vir}(z, M) = (7.84 \times 10^{-4})\Big(\frac{M}{10^8\ \mathrm{h^{-1}M_\odot}}\Big)^{1/3}\Omega_{\rm m,0}^{-1/3} \times \Big(\frac{1+z}{10}\Big)^{-1}\ \mathrm{Mpc/h}. \tag{3.20}$$

We set the maximum physical separation $r_{\rm max}(z) = r_{\rm co,\ max}/(1+z)$. We found $r_{\rm co,\ max} \approx 119.448$ cMpc/h, which is the maximum comoving separation where $\xi_{\rm mm}(z = 10.0, r_{\rm co}) > 0$. Beyond this value, a distant halo would no longer be correlated with the target halo.

Assigning Lyman-Werner Luminosity Density

Given a subset of neighbouring halos each with mass M (units: $\mathrm{h^{-1}\ M_\odot}$) and physical separation r (units: Mpc/h) from the target halo, how do we assign a LW flux to each of them? The most luminous halos would be the rarest, so we assume that the LW luminosity densities of this subset follow a lognormal distribution in L. The LW flux J can be related to L as $L = 16\pi^2 r^2 J$, and thus this becomes a lognormal distribution in r. The probability density that a neighbouring halo of mass M and physical separation r has a LW luminosity density L is given as:

$$\frac{dP}{d\log_{10} L}(\langle L_{\rm LW}(z, M)\rangle, J, r) = \frac{1}{\sigma_{\rm LW}\sqrt{2\pi}} \exp\left[\frac{-(x-\mu)^2}{2\sigma_{\rm LW}^2}\right], \tag{3.21}$$

where $\sigma_{\rm LW} = 0.4$, $x = \log_{10} L$ (L in units of 10^{26} erg $\mathrm{s^{-1}\ Hz^{-1}}$) and $\mu = \log_{10}\langle L_{\rm LW}(z, M)\rangle$ (adapted from Eq. 3 of Dijkstra et al. (2008)). A LW luminosity density (and LW flux) is assigned to each halo such that they follow a lognormal distribution in r with a mean LW luminosity density $\langle L_{\rm LW}(z, M)\rangle$. In our fiducial model, we adapt the model used by D08 and D14.

To compute $\langle L_{\rm LW,\ fid.}(z, M)\rangle$, we must first consider the mean LW photon

production rate $\langle Q(t) \rangle$ (units: h s^{-1} M$_\odot^{-1}$):

$$\langle Q(t) \rangle = (Q_0)[1 + (t_6/4)]^{-3/2} e^{-t_6/300}, \tag{3.22}$$

where $Q_0 = 10^{47}$ photons s^{-1} M$_\odot^{-1}$ and $t = (t_6)\,(10^6\,\mathrm{yr})$. This quantity is derived from the Starburst99 population synthesis model developed by Leitherer et al. (1999) while assuming that star formation occurs with a Salpeter initial mass function. The mean LW luminosity density $\langle L_{\mathrm{LW,\,fid.}}(t, M) \rangle$ (units: erg s^{-1} Hz^{-1}) of a halo of mass M at a time t after star formation begins is given as:

$$\langle L_{\mathrm{LW,\,fid.}}(t, M) \rangle = \frac{h_{\mathrm{P}} \langle \nu \rangle}{\Delta \nu} \langle Q(t) \rangle f_{\mathrm{esc}} f_* \frac{\Omega_{\mathrm{b},0}}{\Omega_{\mathrm{m},0}} M, \tag{3.23}$$

where h_{P} is Planck's constant, $\langle \nu \rangle$ is the mean LW frequency, $\Delta \nu$ is the LW frequency range, $f_{\mathrm{esc}} = 1$ is the LW photon escape fraction and $f_* = 0.05$ is the star formation efficiency. For possible heavy seed formation, it is imperative that the gas within the target halo fully collapses before it may cool and fragment to form stars. It must receive supercritical LW flux from its neighbouring halos for the duration of its free-fall time $t_{\mathrm{ff}}(z)$:

$$t_{\mathrm{ff}}(z) = \sqrt{\frac{3\pi}{32 G \rho(z)}} \sim 83 \left[\frac{1+z}{11} \right]^{-\frac{3}{2}} \mathrm{Myr}, \tag{3.24}$$

where the density of a halo $\rho(z) \approx 200 \bar{\rho}_{\mathrm{m}}(z)$ and we assume that star formation begins in all neighbouring halos simultaneously. Since $\langle L_{\mathrm{LW,\,fid.}}(t, M) \rangle$ monotonically decreases as t increases, if the target halo receives supercritical LW flux at $t = t_{\mathrm{ff}}(z)$, then it has received supercritical LW flux at $t < t_{\mathrm{ff}}(z)$. Therefore we evaluate $\langle L_{\mathrm{LW,\,fid.}}(t, M) \rangle$ at $t = t_{\mathrm{ff}}(z)$, making it strictly a function of z and M only.

Figure 3.5 depicts how $\langle L_{\mathrm{LW,\,fid.}} \rangle$ varies with z for three different values of M. The different values of M are marked as solid lines and vary from 4×10^7 M$_\odot$ up to 6×10^8 M$_\odot$. What we see is that for the fiducial model, the mean luminosity increases with redshift - primarily driven by the dependence on the free-fall time which depends on redshift z.

To test the physicality of this model we again appeal to `Renaissance` and plot the mean LW luminosity $\langle L_{\mathrm{LW,\,Ren.}} \rangle$ as a function of halo mass and redshift from `Renaissance`. When calculating the LW flux from `Renaissance` halos, we first determine the stellar mass of that halo and from that calculate the mean LW flux that is produced by that stellar mass according to the `Renaissance` model. While the data for the largest halo masses is relatively sparse (green data points), the data for the smaller halos is well sampled. In this case we see a relatively flat (slightly decreasing) LW luminosity as a function of redshift. For the lowest mass halos we would expect a slightly lower star formation efficiency and hence a lower

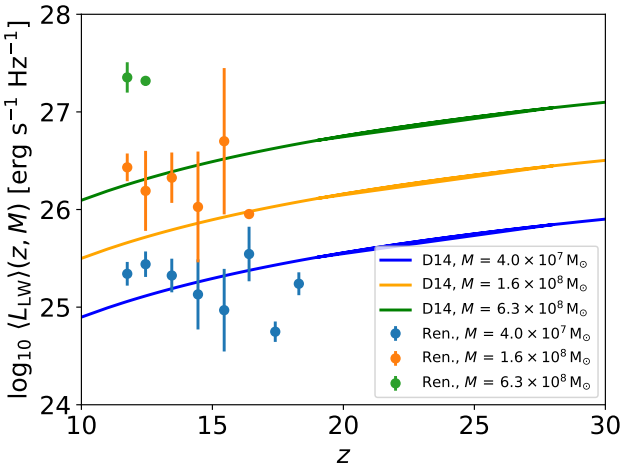

Figure 3.5: Mean LW luminosity density vs. redshift for a number of halo masses. This is the luminosity density, in units of erg s^{-1} Hz^{-1}, emitted by halos with the masses shown in the legend. The mean LW luminosity density in the fiducial model is given by Eq. 3.23. This quantity increases as time decreases and it is evaluated at the free-fall time. The free-fall time decreases as redshift increases, thus the mean luminosity increases as redshift increases. We are evaluating the luminosity when the stars are younger (and hence more luminous) at higher redshift. We also plot data points from the `Renaissance` simulation suite with the mean LW luminosity emitted from halos of a given mass as a function of z. In this case the mean LW luminosity is almost flat with a small decrease (i.e. lower star formation efficiencies) seen for the lowest mass halos. The `Renaissance` data points shown are the median values within a redshift bin, with the error bars being the interquartile range.

mean LW luminosity. However, what we do not see, and is a limitation of the fiducial model, is a mean LW luminosity density which increases with redshift over this range. This divergence of the analytic and hydrodynamical models will feed into our results. Having now introduced the methodology behind our analysis we now present our results.

3.3 Results

As previously stated, the aim of this work is firstly to reproduce and verify the results from D14 and secondly to compare the results of this analysis against the results of other numerical experiments from the literature. We augment this goal by also taking advantage of the `Renaissance` suite of simulations and use some of the relevant `Renaissance` data in the analytic models. Although the `Renaissance` suite cannot capture the rare halos that experience super-critical LW radiation at the values thought necessary to produce heavy seeds (i.e. $J_{\rm crit} \gtrsim 300$ J$_{21}$), it is nonetheless an important check on the self-consistency of the analytic model, particularly the probability of finding pristine halos $P_{\rm pristine}(z)$ as a function of redshift and the mean LW luminosity density $\langle L_{\rm LW}(z, M)\rangle$ as a function of halo

mass and redshift.

3.3.1 Supercritical Probability

In previous works, $J_{\rm crit}$ was chosen to be 30 – 300 J_{21} for a T = 10^4 K blackbody spectrum (see Shang et al. (2010)) and 1000 J_{21} for a T = 10^5 K spectrum (see Wolcott-Green et al. (2011)). D14 chose $J_{\rm crit} = 300\,J_{21}$ as an intermediate value between these two spectra. In this work we follow D14 and choose $J_{\rm crit} = 300 J_{21}$ as a critical threshold for the LW pathway. We also investigate solutions with $J_{\rm crit}$ = 1.0, 30.0 and 1000.0 J_{21}.

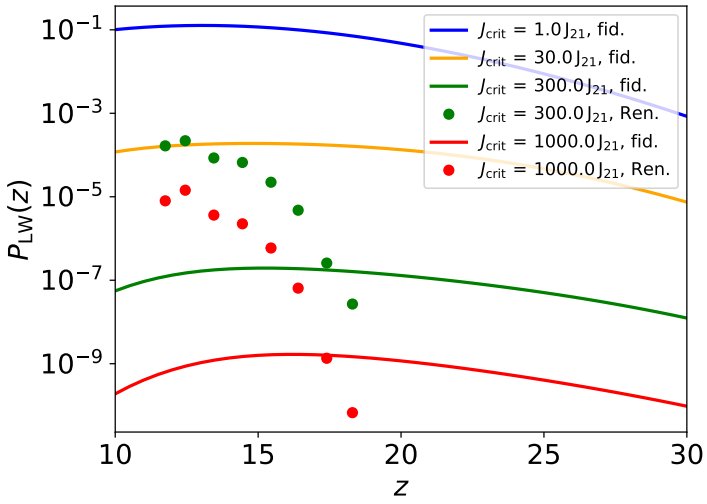

Figure 3.6: The supercritical probability vs. redshift. The probability of a halo receiving a super-critical LW flux is given by the y-axis. Line colours refer to values of $J_{\rm crit}$. As expected, the probability of a halo receiving a high flux (e.g. $J_{\rm crit} \geq 300$ J_{21}) is low. The solid lines are from the fiducial model. The points are from the `Renaissance`-augmented models. For these models, the probability of a halo receiving a super-critical flux drops sharply with redshift - more in line with expectations.

In Figure 3.6, we plot the probability of a target halo receiving a supercritical flux $P_{\rm LW}(z)$ at different redshifts. The probability is plotted for a range of different values of the critical flux, $J_{\rm crit}$, from $J_{\rm crit}$ = 1.0 J_{21} up to $J_{\rm crit}$ = 1000.0 J_{21}. Solid lines are from the fiducial model as described by the first line of Eq. 3.8 and the first line of Eq. 3.9. We also account for metal pollution from neighbouring halos using the Heaviside function (see the first line of Eq. 3.9). As expected the probability of a target halo receiving a flux in excess of J = 1.0 J_{21} is very high. In this case by a redshift of $z = 10$, approximately 1 in 10 halos meeting the target halo criteria will receive a flux greater than or equal to J = 1.0 J_{21}. However, the probability of a target halo receiving significantly higher fluxes is much less. For example the probability of a target halo receiving a flux in excess of J = 1000.0 J_{21} at $z = 10$ is less than 1 in 10^9. We test our fiducial model at $J_{\rm crit}$ = 1.0 and 30.0 J_{21} to verify that $P_{\rm LW}$ should increase as $J_{\rm crit}$ increases. Note that in this

model, the peak in terms of probabilities occurs at $z \sim 15$ and decreases at higher and lower redshifts.

It should also be noted that the probability of a halo receiving a supercritical flux does not decrease as rapidly as perhaps expected towards very high redshift (i.e. $z \geq 20$). This is an inherent characteristic of the fiducial model. The model requires that a target halo is illuminated by a super-critical flux for a free-fall time (see §3.2.5). While the number of star-forming halos decreases as per the halo mass function, the free-fall time shrinks dramatically with redshift. The two effects cancel each other out somewhat and hence the probability of receiving a super-critical flux does not decrease as redshift increases as rapidly as expected.

Overplotted in Figure 3.6 are the results from the `Renaissance`-augmented model as described by the second line of Eq. 3.8 and the second line of Eq. 3.9. The green and red dots refer to median $P_{\text{LW, Ren.}}(z)$ values of each redshift bin at $J_{\text{crit}} = 300$ and 1000 J_{21} respectively. We augment the fiducial model based on D14 with the mean LW values $\langle L_{\text{LW, Ren.}}(z, M)\rangle$ instead of the analytic model values $\langle L_{\text{LW, fid.}}(z, M)\rangle$. We also do not account for the influence of metal pollution in the `Renaissance`-augmented model here and thus comparisons to the fiducial model must be made cautiously. We account for metal pollution for the `Renaissance`-augmented model when plotting formation site number density $n_{\text{heavy seed host}(z)}$ as a function of redshift z in Figure 3.7 (see §3.3.2). We set $J_{\text{crit}} = 300$ and 1000 J_{21} for the `Renaissance`-augmented models only. This was to provide a comparison to the fiducial dataset of D14 at $J_{\text{crit}} = 300\,\text{J}_{21}$ (see black dots of Figure 3.7) and also to test the model at $J_{\text{crit}} = 1000\,\text{J}_{21}$ which may be an appropriate value for a $\text{T} = 10^5\,\text{K}$ spectrum (see Wolcott-Green et al. (2011)). For the simulation values, we see a much steeper decline in the probability of a halo receiving a super-critical flux (driven mainly by the mean LW luminosity density). Hence, for redshifts approaching $z \sim 20$ the probability of a halo receiving a supercritical flux is negligible. This is in comparison to the analytic model where the probabilities only decline slowly.

Note that we do not include any direct comparison to observational nor simulation data. It is not possible to derive these probabilities from observations especially at such high redshifts. As stated earlier, the `Renaissance` simulations cannot capture the incredibly rare halos that receive such high levels of LW radiation. Any nonzero probabilities from other large-scale simulations would likely yield very low values e.g. less than 10^{-9}.

3.3.2 Heavy Seed Number Density

Putting everything together, we now plot the number density of halos acting as heavy seed formation sites $n_{\text{heavy seed host}}(z)$ as a function of redshift z in Figure 3.7. In total we plot 10 datasets. With the exception of the black dots, all

dotted datasets are the median values of a redshift bin. These datasets include: our fiducial model with $J_{\rm crit} = 300\,{\rm J}_{21}$ (green line) and $J_{\rm crit} = 1000\,{\rm J}_{21}$ (red line); our `Renaissance`-augmented model with $J_{\rm crit} = 300\,{\rm J}_{21}$ (green dots) and $J_{\rm crit} = 1000\,{\rm J}_{21}$ (red dots); the heavy seed number density from Trinca et al. (2022) (solid blue line with circular markers); the DCBH number density from Chiaki et al. (2023) (solid magenta line with circular dots); the heavy seed formation site number density from McCaffrey et al. (2025) (orange dots); and the heavy seed formation site number density from D14 with $J_{\rm crit} = 300\,{\rm J}_{21}$ (black dots).

We also include an AGN number density estimate from Inayoshi (2025). This model is based on the observed and inferred abundance of LRDs, suggesting that LRDs are a phase in galaxy evolution. The brown dashed line in Figure 3.7 shows this fit for $6 \leq z \leq 10$. The brown dots are the inferred AGN number densities based on recent observations for $6.5 \leq z \leq 8.5$ from Kokorev et al. (2024) and Kocevski et al. (2025). The fit from Inayoshi (2025) was normalised such that the AGN number density matches the observed LRD number density of $\approx 3 \times 10^{-5}$ cMpc^{-3} for $z \sim 4 - 7$. We include these estimates to provide context for our heavy seed datasets but we must note that a heavy seed number density cannot be directly compared to these AGN number density estimates. These AGN number densities which are informed by recent observations likely account for only the most active of AGN, while in reality many AGN will be quiescent and thus making the total AGN number density larger. We also note that only a fraction of heavy seeds will undergo efficient growth to reach SMBH masses by $z \sim 6$. Thus in Figure 3.7, if a heavy seed number density estimate at $z \sim 10$ is equal to or greater than this AGN number density estimate, that pathway may be viable to account for SMBH number densities. If a heavy seed number density estimate is less than the AGN number density estimate, that pathway can at best only account for a fraction of SMBHs.

For our fiducial models (green and red lines), we are unable to match results from D14 (black dots) exactly despite following their methodology and our results deviate from theirs, particularly at high redshift. Without access to their code base we cannot determine where the discrepancy arises. Our code base and pipeline will be publicly available on GitHub but until then may be accessed upon request.

Both the results from the fiducial model and the results of D14 do however agree that the number density of heavy seed black holes (or indeed heavy seed hosting halos) is less that 10^{-6} cMpc^{-3} at $z \gtrsim 10$. With the number density of MBH hosting galaxies at least two orders of magnitude greater than this (and potentially likely much higher) at $z \gtrsim 4$ (e.g. Pérez-González et al., 2024; Inayoshi, 2025), the LW channel is likely unable to explain the high abundances of MBHs in the early Universe based on our fiducial model. This is the first takeaway from our analysis.

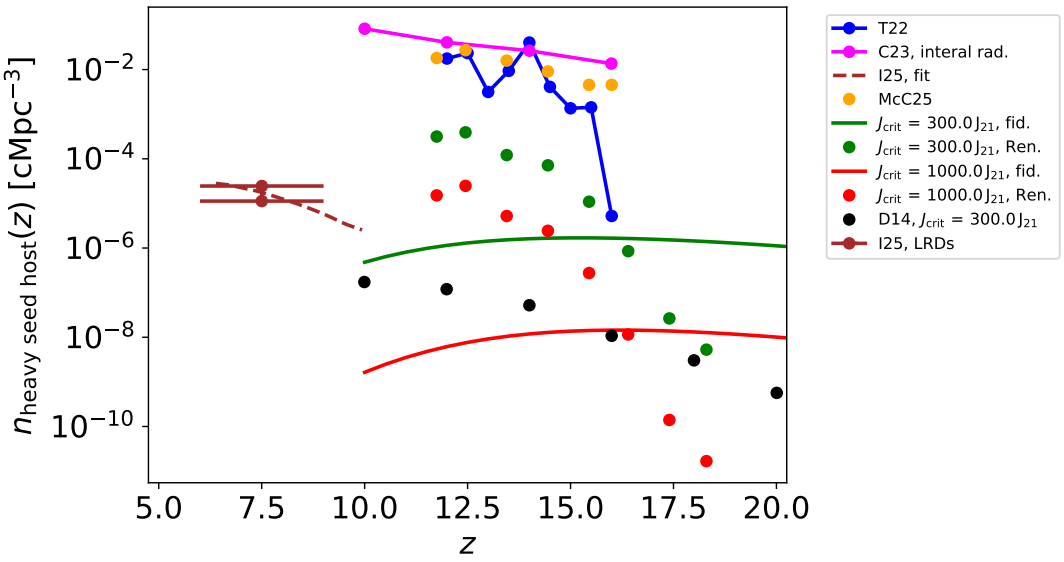

Figure 3.7: Number density of heavy seeds vs. redshift. Black dots are original points taken from D14, green and red lines show our use of the same analytic model methodology as outlined in D14, the green and red dots use `Renaissance`-informed data as part of the analytic model, orange dots are from McCaffrey et al. (2025), the solid blue line with circular markers is from Trinca et al. (2022), the solid magenta line with circular markers is from Chiaki et al. (2023) (with internal radiation), and the brown lines are from Inayoshi (2025) (dashed line for the AGN number density fit; dots for the LRD number density estimate based on observations). The LW-only channel models (D14, fiducial model, `Renaissance`-augmented model) are unable or only very marginally able to reproduce recent JWST high-z AGN number density of $\gtrsim 10^{-4}$ cMpc^{-3}. On the other hand, the models of McCaffrey et al. (2025), Trinca et al. (2022) and Chiaki et al. (2023) produce higher number densities and are thus more compatible with recent JWST observations.

We plot the results using values obtained from the `Renaissance`-informed analytic models as green ($J_{\text{crit}} = 300\,\text{J}_{21}$) and red dots ($J_{\text{crit}} = 1000\,\text{J}_{21}$). In this case the results are more encouraging - albeit with a steeper decline. Note that we are not using the `Renaissance` output to make predictions but use their mean LW luminosity density values $\langle L_{\text{LW, Ren.}}(z, M)\rangle$ and the impact of genetic and external metal pollution is informed by their $P_{\text{pristine, Ren.}}(z)$ function (see Figure 3.5 and Figure 3.4 respectively). We see that the number density of heavy seed hosting halos peaks at approximately 10^{-4} cMpc^{-3} at $z \sim 12.5$ for $J_{\text{crit}} = 300$ J$_{21}$. These numbers are on the face of it consistent, albeit marginally, with the recent results from JWST (see AGN number density estimates from Inayoshi (2025) (brown dots and brown dashed line)). However, our models are for the seeds and not the candidate AGN detected by JWST. Given the growth requirements of the seeds combined with the expected duty cycle of AGN, these number densities are still likely incompatible with current JWST observations.

We also plot more recent results by Trinca et al. (2022) (solid blue line with

circular markers), Chiaki et al. (2023) (solid magenta line with circular dots) and McCaffrey et al. (2025) (orange dots). McCaffrey et al. (2025) used the `Renaissance` simulations to analyse the formation and later the growth of heavy seed black holes while accounting for rapid assembly and merger history of halos. We do not account for growth in this comparison and only consider their number density of heavy seed formation sites. They used the following criteria when identifying halos that may host massive black holes:

- $\mathrm{T_{vir}} \gtrsim 10^4$ K,
- $Z < 10^{-3}\,\mathrm{Z_\odot}$,
- $M(r < 0.5R_{\mathrm{vir}})/M(r < R_{\mathrm{vir}}) > 0.5$,
- $\dot{M} > 0.1\,\mathrm{M_\odot\,yr^{-1}}$.

The results from McCaffrey et al. (2025) show that the formation of heavy seed MBHs via the so-called rapid assembly channel results in significantly higher number densities with values of approximately 10^{-2} cMpc^{-3} or higher. These results from McCaffrey et al. (2025) are consistent with recent JWST results (again with the caveat that the growth of seeds and the duty cycle of AGN will push these number densities downwards).

Trinca et al. (2022) performed a similar analysis to McCaffrey et al. (2025) using the Cosmic Archaeology Tool (CAT), a semi-analytic model which allowed them to follow the formation of the first stars and black holes while accounting for accretion and mergers. They also account for how star formation in mini-halos can be affected by LW flux from nearby highly star-forming galaxies. This inhibits H_2 cooling and potentially sterilises these halos until they reach the atomic-cooling regime. In their model, if a dark matter halo meets the following conditions:

1. $\mathrm{T_{vir}} \gtrsim 10^4$ K,
2. $Z < 10^{-3.8}\,\mathrm{Z_\odot}$,
3. $J_{\mathrm{LW}} > 300\,\mathrm{J_{21}}$,

then a heavy seed black hole with $M_{\mathrm{BH}} = 10^5$ M$_\odot$ is set at the centre of the galaxy within the halo. Their data in Figure 3.7 indicate the number density of newly-formed heavy seeds at a given redshift. Their results show similar number densities to McCaffrey et al. (2025) with peak values 10^{-2} cMpc^{-3}. Their model shows number densities significantly beyond the LW-only channel, again compatible with more recent results from JWST.

When computing the number density of DCBHs, Chiaki et al. (2023) consider both external and internal LW radiation, rather than only external sources like we

do. They make a direct comparison to Trinca et al. (2022) by considering halos with $T_{vir} > 10^4$ K, $J_{crit} = 300$ J_{21} and $Z < 10^{-3.8}$ $Z_\odot$. Internal radiation from a single halo depends on its LW photon emissivity (from both Pop III and Pop II stars) and the radius of the galaxy hosted by that halo (where the galaxy radius is 10% of the halo virial radius). External radiation received by a single halo is computed from the total LW flux from all other halos and is dependent on LW photon emissivity and the distance between the target and source halos. Metal pollution is accounted for via chemical evolution equations of Pop I/II stars and supernova winds. Their highest number density value is almost 10^{-1} cMpc^{-3} at $z = 10$.

Additionally, Bhowmick et al. (2021) explored a similar LW channel with the inclusion of low gas angular momentum to track SMBH seed formation and Bhowmick et al. (2024) used the `BRAHMA` simulations to track DCBH formation. Both works found that more efficient heavy seeding channels may be necessary to account for the most massive black holes at high redshift.

In summary, Figure 3.7 tells us that D14, our re-implementation of the D14 model and the `Renaissance`-augmented model show results which are incompatible with recent JWST data. Other pathways investigated by McCaffrey et al. (2025), Trinca et al. (2022) and Chiaki et al. (2023) appear more promising to explain the overall MBH population. A similar result was shown by Bhowmick et al. (2021).

3.4 Discussion and Conclusions

In this Chapter, we have reviewed the analytic model of Dijkstra et al. (2014) in terms of calculating the number density of MBHs that can be formed through the so-called Lyman-Werner (LW) channel. In this framework, a super-critical flux of LW radiation irradiates a target halo. The target halo must have a mass exceeding the atomic-cooling threshold and must be metal-free. The super-critical flux required can vary from halo to halo but is likely to be excess of 300 J_{21}. Such a high value can only be produced by a nearby neighbouring halo. A weakness of this model is assuming that there is no correlation between a halo being metal-free and receiving a super-critical LW flux i.e. we multiply the probabilities $P_{\rm pristine}(z)$ and $P_{\rm LW}(z, J_{\rm crit})$. More realistically, a super-critical LW flux may suppress star formation in a progenitor halo and thus the target halo has an increased probability of being metal-free. Such an analysis of the merger history of the target halos is beyond the scope of this study.

In agreement with D14, we find that the number density of target halos receiving a critical flux in excess of 300 J_{21} is approximately 10^{-6} cMpc^{-3} at $z = 10$ (see Figure 3.7). The number densities drop, as expected, towards higher redshifts. Despite considerable effort, we were unable to reproduce the exact

results of D14 and our fiducial model results differ from the D14 results at $z > 10$. We varied the cosmology implemented, the integration limits for neighbouring halo mass M and separation r, how the halo-halo correlation function was computed and the definition of the mean LW luminosity density. Our analysis tools and pipeline will be available on GitHub. Our analysis, following the methodology of D14, shows that the number density of heavy seeds is almost constant out to very high redshift ($z \gtrsim 20$) - this is primarily due to how the mean LW luminosity $\langle L_{\text{LW, fid.}}(z, M) \rangle$ produced by a halo is calculated in the D14 model. Nonetheless, our analysis agrees very well with the D14 as we approach $z = 10$. However, in both cases the number densities remain close to or below 10^{-6} cMpc^{-3}.

To check the physical consistency of the D14 model, we augment the analytic model with information taken directly from the `Renaissance` simulation suite. Specifically, we take data of the mean LW luminosity density $\langle L_{\text{LW, Ren.}}(z, M) \rangle$ produced as a function of redshift and halo mass and the pristine fraction $P_{\text{pristine, Ren.}}(z)$ of halos as a function of redshift (see Figures 3.5 and 3.4). Using this augmented model, we find that number density of heavy seed hosting halos increases steeply between $z \sim 18$ and $z \sim 10$. The peak number density of heavy seed hosting halos reaching values close to 10^{-4} cMpc^{-3} at $z \sim 10$.

The `Renaissance`-informed models are nonetheless still likely incompatible with the recent results on AGN fractions at high-redshift (e.g. Pérez-González et al., 2024; Greene et al., 2024; Inayoshi, 2025) given subsequent growth requirements of the seeds combined with the expected duty cycle of AGN. A slight weakness of this model is the lack of incorporation of baryonic matter streaming velocities (Tseliakhovich & Hirata, 2010). This would suppress star formation in halos with masses $\lesssim 10^6$ M$_\odot$ (Tseliakhovich et al., 2011; O'Leary & McQuinn, 2012; Xu et al., 2014). This is an order of magnitude below the M$_{\text{min}}$ values we consider, so this may not affect our results greatly. It could push $P_{\text{pristine, Ren.}}(z)$ to higher values since star formation would be suppressed in more progenitor halos, leading to more target halos avoiding genetic metal pollution.

We have shown through our heavy seed number density predictions that the LW-only channel is likely sub-dominant compared to other channels when accounting for AGN number density estimates based on recent observations. While these observations are still hotly debated and the exact make-up of the JWST galaxies unclear, even if some fraction of the galaxies host AGN (as is strongly suspected) then the LW-only channel cannot be responsible - the predicted number densities are simply too low.

Chapter 4

Summary and Conclusions

4.1 Aims

It is an incredibly exciting time for both theoretical and observational astrophysics (at time of writing but hopefully still at time of reading). With the recent launch of the James Webb Space Telescope (JWST), we have thrown open a window to the high-redshift Universe by observing distant galaxies and quasars never seen before. These data have challenged our models of supermassive black hole (SMBH) formation and may be key to revealing their origins. Additionally, the upcoming launch of the Laser Interferometer Space Antenna (LISA) promises detections of gravitational waves of black hole mergers from the high-redshift Universe. What sets it apart from existing ground-based gravitational wave detectors is the capability of detecting mergers from intermediate-mass black holes (IMBHs). This population would bridge the mass gap between stellar mass black holes and SMBHs and act as a potential seed for SMBHs.

In §2, we aimed to test well-known fitting functions of the halo mass function at high redshift against simulation results. We had this goal in mind to investigate if these fitting functions could be a source of error when comparing JWST data to cosmological models. We do this by running dark matter-only `Enzo` and `SWIFT` simulations, creating halo catalogues from the output and using these halo catalogues to create numerical number density functions. We compare these to number densities derived from popular fitting functions: Press & Schechter (1974), Sheth et al. (2001), Reed et al. (2007) and Watson et al. (2013) (both Spherical Overdensity (SO) and Friends-of-Friends (FoF)). When creating the halo catalogues, we use both the FOF (Friends-of-Friends (Efstathiou et al., 1985)) and HOP (particle "hopping" (Eisenstein & Hut, 1998)) halo finders to minimise our results being biased by our choice of halo finder.

In §3, our goal is to compare the number density of IMBHs informed by an analytic model accounting for Lyman-Werner (LW) radiation and metal pollution (Dijkstra et al., 2014) with one informed by `Renaissance` simulation results. This

is to investigate whether or not recent JWST observations could be accounted for by this heavy seed formation pathway alone. In both models, we use the Sheth et al. (2001) halo mass function and we assume that the LW flux received at a prospective formation site is dominated by a single nearby neighbouring source. In our fiducial model, the mean LW luminosity density emitted by a neighbour is determined by an analytic function of redshift z and mass M, and we account for both genetic metal pollution from progenitor halos and external supernova outflows from neighbours. In the `Renaissance`-informed model, the mean LW luminosity density is determined from the mean luminosity of a given mass bin at a given redshift. We also account for metal pollution but with no distinction between genetic and external enrichment.

4.2 Conclusions

In §2, we find that generally there is reasonable agreement between number densities from the (semi-)analytic halo mass functions and from the simulation output. Our simulations begin at $z = 127$ and end at $z = 10$. We take output at snapshots $z = 20$, $z = 15$ and $z = 10$ as they are part of an era of the Universe that is relatively unexplored. We also end our simulations at $z = 10$ as now we are able to observe objects at this redshift thanks to JWST. The agreement is strongest at the lowest masses (10^6 to 10^7 h^{-1} $M_\odot$) and $z = 10$ where the fits overestimate the number densities by a factor of ~ 2 compared to simulation data. At higher redshifts ($z = 15$) and masses ($M > 10^7$ h^{-1} $M_\odot$), the discrepancy widens with the Press & Schechter (1974) fit performing the poorest (underestimating the simulated number density by a factor of ~ 100) and the Sheth et al. (2001) performing the best (at best agreeing with the simulated number density within a factor of 2). We find that the discrepancy is wider when comparing `SWIFT` to `Enzo` for the highest masses ($M \sim 10^9$ to 10^{10} h^{-1} $M_\odot$) at $z = 15$ using the FOF halo finder. The SMT fit underestimates the `SWIFT` number density by a factor of ~ 5 in this mass window but overestimates the `Enzo` number density by less than a factor of 2 in the same window. This may be due to how the FOF halo finder is employed between the different simulation suites. This cross-simulation discrepancy is absent when considering the HOP halo finder. Given this agreement between (semi-)analytic fits and numerical simulations, the halo mass function (especially SMT and WatsonFoF) is unlikely to be a significant source of error when comparing JWST data to ΛCDM predictions of the high-redshift Universe. Possibly more dominant sources of error include cosmic variance, stellar mass estimation and some halos losing dark matter (giving the impression of a higher baryon-dark matter ratio) which were all explored by Chen et al. (2023).

In §3, we are unable to replicate the number density values of Dijkstra et al.

(2014) using their model. Our redshift range is $10 \leq z \leq 30$ and our number density values match for $z = 10$ but deviate as redshift increases. We find that both the LW supercritical probability and heavy seed number density vary little with redshift for a fixed value of $J_{\rm crit}$. The halo mass function decreases as redshift increases while the mean LW luminosity density increases with redshift due its dependence on the free-fall time. These effects somewhat cancel each out and we are left with relatively flat redshift evolution, with the number density peaking at $z \sim 15$ and slowly decreasing as redshift increases $z \gtrsim 15$. In the `Renaissance`-informed model, we see a much sharper decrease in number density as redshift increases. This is due in part to the `Renaissance`-informed mean LW luminosity density either varying little with redshift (low mass) or decreasing as redshift increases (high mass). The highest number densities produced ($n_{\text{heavy seed host}} \sim 10^{-4}$ cMpc^{-3}, $z \sim 10$, $J_{\rm crit} = 300$ J$_{21}$, `Renaissance`-informed model) are too low to account for JWST observations. These number densities refer to seed black holes only and due to the accretion rates and AGN duty cycles required for SMBHs, they would be too low to account for the AGN number densities from JWST observations. A model that accounts for rapid assembly due to major and minor galaxy mergers would be more promising (see McCaffrey et al. (2025)).

4.3 Future Work

As stated in the previous section, the inclusion of rapid assembly to our heavy seed formation model from §3 would make it more physical. This would involve accounting for major and minor mergers of halos (and their galaxies), which would heat the gas and delay star formation. This would result in the dark matter halo (prospective formation site) growing and creating a deeper potential well, allowing for supermassive star (SMS) formation. Tracking such an effect would require merger trees showing the merger history of a given halo. This could be achieved using either the C package `consistent-trees` (Behroozi et al., 2012) or the C++ package `TreeFrog` (Elahi et al., 2019). As shown by McCaffrey et al. (2025), the number densities produced could align better with JWST observations.

Additionally, baryonic streaming velocities would act as another mechanism to inhibit cooling and delay typical star formation. The velocities of the baryons relative to the dark matter would result in the baryons needing additional time to lose their kinetic energy before they could collapse, also allowing the dark matter potential well to deepen and later have a SMS form. Kulkarni et al. (2021) have shown that this is not simply an effect that acts independently of LW radiation: the two effects are not multiplicative but will influence one another.

In §3, we also treat metal enrichment acting independently of LW background radiation but a more robust treatment would account for its dependence on the

background flux $J_{\rm bg}$ (Trenti & Stiavelli, 2009).

A natural extension to estimating the IMBH number density would be estimating the number density of IMBH binary systems. Gravitational waves from these binary merging events would be detectable by the upcoming space-based detector LISA. Like with the influence of rapid assembly mentioned above, computing the number density of binaries would require building merger trees and accounting for what are the most favourable merging conditions.

Bibliography

Abbott B. P. et al., 2019, ApJ, 882, L24

Abbott R. et al., 2023, The Astrophysical Journal Supplement Series, 267, 29

Agarwal B., Khochfar S., 2015, MNRAS, 446, 160

Agarwal B., Smith B., Glover S., Natarajan P., Khochfar S., 2016, MNRAS, 459, 4209

Aihara H. et al., 2011, ApJS, 193, 29

Almeida A. et al., 2023, ApJS, 267, 44

Alpher R. A., Herman R., 1948, Nature, 162, 774

Alvarez M. A., Wise J. H., Abel T., 2009, ApJ, 701, L133

Ananna T. T., Bogdán Á., Kovács O. E., Natarajan P., Hickox R. C., 2024, ApJ, 969, L18

Andika I. T. et al., 2022, AJ, 163, 251

Arrabal Haro P. et al., 2023, Nature, 622, 707

Astropy Collaboration et al., 2022, ApJ, 935, 167

Astropy Collaboration et al., 2018, AJ, 156, 123

Astropy Collaboration et al., 2013, A&A, 558, A33

Bañados E. et al., 2018, Nature, 553, 473

Bakels L., 2018, *Convert* `GADGET` *binary and hdf5 files*. https://github.com/luciebakels/GADGET_convert_binary_hdf5

Bardeen J. M., Bond J. R., Kaiser N., Szalay A. S., 1986, Astrophys. J., 304, 15

Barkana R., Loeb A., 2001, Physics Reports, 349, 125

Behroozi P. S., Wechsler R. H., Wu H.-Y., Busha M. T., Klypin A. A., Primack J. R., 2012, The Astrophysical Journal, 763, 18

Bhowmick A. K., Blecha L., Torrey P., Kelley L. Z., Vogelsberger M., Nelson D., Weinberger R., Hernquist L., 2021, Monthly Notices of the Royal Astronomical Society, 510, 177–196

Bhowmick A. K. et al., 2024, MNRAS, 533, 1907

Binney J., Tremaine S., 2008, *Galactic Dynamics: Second Edition*. Princeton University Press

Bogdán Á. et al., 2024, Nature Astronomy, 8, 126

Boylan-Kolchin M., 2023, Nature Astronomy, 7, 731

Brown R. A., 1996, in *Science with the Hubble Space Telescope - II*, Benvenuti P., Macchetto F. D., Schreier E. J., eds., p. 603

Brummel-Smith C. et al., 2019, The Journal of Open Source Software, 4, 1636

Bryan G. L., Norman M. L., 1997a, arXiv e-prints, astro, arXiv:astro-ph/9710187

Bryan G. L., Norman M. L., 1997b, in *Astronomical Society of the Pacific Conference Series*, Vol. 12, Computational Astrophysics; 12th Kingston Meeting on Theoretical Astrophysics, Clarke D. A., West M. J., eds., p. 363

Bryan G. L., Norman M. L., 1998, The Astrophysical Journal, 495, 80–99

Bryan G. L., Norman M. L., O'Shea B. W., Abel T., Wise J. H., Turk M. J., The Enzo Collaboration, 2014, ApJS, 211, 19

Bunker A. J., et al., 2023, Astronomy & Astrophysics, 677, A88

Cameron A. J., Katz H., Rey M. P., Saxena A., 2023, MNRAS, 523, 3516

Carloni Y., Luongo O., Muccino M., 2025, Phys. Rev. D, 111, 023512

Carniani S. et al., 2024, Nature, 633, 318

Carroll B. W., Ostlie D. A., 2017, *An Introduction to Modern Astrophysics, Second Edition*. Cambridge University Press

Castellano M. et al., 2024, ApJ, 972, 143

Chakraborty P., Sarkar A., Wolk S., Schneider B., Brickhouse N., Lanzetta K., Foster A., Smith R., 2024, arXiv e-prints, arXiv:2406.05306

Charbonnel C., Schaerer D., Prantzos N., Ramírez-Galeano L., Fragos T., Kuruvanthodi A., Marques-Chaves R., Gieles M., 2023, A&A, 673, L7

Chen P., Wise J. H., Norman M. L., Xu H., O'Shea B. W., 2014, ApJ, 795, 144

Chen Y., Mo H. J., Wang K., 2023, MNRAS, 526, 2542

Cheng H., Greengard L., Rokhlin V., 1999, Journal of Computational Physics, 155, 468

Chiaki G., Chon S., Omukai K., Trinca A., Schneider R., Valiante R., 2023, MNRAS, 521, 2845

Chilingarian I. V., Katkov I. Y., Zolotukhin I. Y., Grishin K. A., Beletsky Y., Boutsia K., Osip D. J., 2018, The Astrophysical Journal, 863, 1

Clesse S., 2015, arXiv e-prints, arXiv:1501.00460

Colless M. et al., 2001, MNRAS, 328, 1039

Colless M. et al., 2003, arXiv e-prints, astro, 10.48550/arXiv.astro-ph/0306581

Copeland E. J., Sami M., Tsujikawa S., 2006, International Journal of Modern Physics D, 15, 1753

Croton D. J. et al., 2006, Monthly Notices of the Royal Astronomical Society, 365, 11–28

De Barros S. et al., 2017, Astronomy & Astrophysics, 608, A123

Dijkstra M., Ferrara A., Mesinger A., 2014, MNRAS, 442, 2036

Dijkstra M., Haiman Z., Mesinger A., Wyithe J. S. B., 2008, Monthly Notices of the Royal Astronomical Society, 391, 1961

Dubois Y. et al., 2014, MNRAS, 444, 1453

Efstathiou G., 2025, Philosophical Transactions of the Royal Society of London Series A, 383, 20240022

Efstathiou G., Davis M., White S. D. M., Frenk C. S., 1985, The Astrophysical Journal Supplement Series, 57, 241, publisher: IOP ADS Bibcode: 1985ApJS...57..241E

Einstein A., 1915, Sitzungsberichte der Königlich Preußischen Akademie der Wissenschaften (Berlin), 844

Eisenstein D. J., Hu W., 1998, The Astrophysical Journal, 496, 605, publisher: IOP ADS Bibcode: 1998ApJ...496..605E

Eisenstein D. J., Hut P., 1998, The Astrophysical Journal, 498, 137, publisher: IOP ADS Bibcode: 1998ApJ...498..137E

Elahi P. J., Poulton R. J. J., Tobar R. J., Cañas R., Lagos C. d. P., Power C., Robotham A. S. G., 2019, Publications of the Astronomical Society of Australia, 36

Fan X., Bañados E., Simcoe R. A., 2023, ARA&A, 61, 373

Fan X. et al., 2006, AJ, 132, 117

Farr W. M., Sravan N., Cantrell A., Kreidberg L., Bailyn C. D., Mandel I., Kalogera V., 2011, ApJ, 741, 103

Fernandez R., Bryan G. L., Haiman Z., Li M., 2014, MNRAS, 439, 3798

Finkelstein S. L. et al., 2024, ApJ, 969, L2

Förster Schreiber N. M., Wuyts S., 2020, ARA&A, 58, 661

Friedmann A., 1922, Zeitschrift fur Physik, 10, 377

Frigo M., Johnson S., 2005, *Proceedings of the IEEE*, 93, 216

Galli D., Palla F., 1998, A&A, 335, 403

Gardner J. P. et al., 2023, PASP, 135, 068001

Gardner J. P. et al., 2006, Space Sci. Rev., 123, 485

Geller M. J., Huchra J. P., 1989, Science, 246, 897

Gentile F. et al., 2024, ApJ, 973, L2

Greene J. E., Ho L. C., 2004, ApJ, 610, 722

Greene J. E. et al., 2024, ApJ, 964, 39

Greene J. E., Strader J., Ho L. C., 2020, ARA&A, 58, 257

Greenstein J. L., Schmidt M., 1964, ApJ, 140, 1

Gunn J. E. et al., 2006, The Astronomical Journal, 131, 2332

Guth A. H., 1981, Phys. Rev. D, 23, 347

Habouzit M., Volonteri M., Latif M., Dubois Y., Peirani S., 2016, MNRAS, 463, 529

Hahn O., Abel T., 2011, MNRAS, 415, 2101

Hainline K. N. et al., 2024, ApJ, 976, 160

Harikane Y., Nakajima K., Ouchi M., Umeda H., Isobe Y., Ono Y., Xu Y., Zhang Y., 2024, ApJ, 960, 56

Harikane Y. et al., 2023, ApJ, 959, 39

Hayward C. C., Torrey P., Springel V., Hernquist L., Vogelsberger M., 2014, MNRAS, 442, 1992

Heger A., Fryer C. L., Woosley S. E., Langer N., Hartmann D. H., 2003, ApJ, 591, 288

Helton J. M. et al., 2025, Nature Astronomy, 10.1038/s41550-025-02503-z

Hinshaw G. et al., 2013, ApJS, 208, 19

Hirano S., Hosokawa T., Yoshida N., Kuiper R., 2017, Science, 357, 1375

Hu H., Inayoshi K., Haiman Z., Ho L. C., Ohsuga K., 2025, ApJ, 983, L37

Hubble E., 1929, *Proceedings of the National Academy of Sciences*, 15, 168

Huchra J., Davis M., Latham D., Tonry J., 1983, ApJS, 52, 89

Huško F., Lacey C. G., 2023, MNRAS, 520, 5090

Inayoshi K., 2025, ApJ, 988, L22

Inayoshi K., Visbal E., Haiman Z., 2020, ARA&A, 58, 27

Izumi T. et al., 2021, ApJ, 914, 36

Jiang L. et al., 2016, The Astrophysical Journal, 833, 222

Johnson J. L., 2012, in *The First Galaxies*, Springer Berlin Heidelberg, pp. 177–222

Kannan R. et al., 2023, MNRAS, 524, 2594

Kaspi S., Smith P. S., Netzer H., Maoz D., Jannuzi B. T., Giveon U., 2000, ApJ, 533, 631

Keller B. W., Munshi F., Trebitsch M., Tremmel M., 2023, ApJ, 943, L28

Khandai N., Di Matteo T., Croft R., Wilkins S., Feng Y., Tucker E., DeGraf C., Liu M.-S., 2015, MNRAS, 450, 1349

Kim J.-h. et al., 2014, ApJS, 210, 14

Klessen R. S., Glover S. C. O., 2023, ARA&A, 61, 65

Klypin A. A., Trujillo-Gomez S., Primack J., 2011, The Astrophysical Journal, 740, 102

Knebe A. et al., 2011, MNRAS, 415, 2293

Kocevski D. D. et al., 2025, ApJ, 986, 126

Kocevski D. D. et al., 2023, ApJ, 954, L4

Kokorev V. et al., 2024, ApJ, 968, 38

Kokorev V. et al., 2023, ApJ, 957, L7

Kormendy J., Ho L. C., 2013, ARA&A, 51, 511

Kreidberg L., Bailyn C. D., Farr W. M., Kalogera V., 2012, ApJ, 757, 36

Kulkarni M., Visbal E., Bryan G. L., 2021, ApJ, 917, 40

Labbé I. et al., 2023, Nature, 616, 266

Lacey C., Cole S., 1994, Monthly Notices of the Royal Astronomical Society, 271, 676–692

Lambrides E. et al., 2024, arXiv e-prints, arXiv:2409.13047

Landt H., Elvis M., Ward M. J., Bentz M. C., Korista K. T., Karovska M., 2011, MNRAS, 414, 218

Larson R. L. et al., 2023, ApJ, 953, L29

Latif M. A., Bovino S., Van Borm C., Grassi T., Schleicher D. R. G., Spaans M., 2014a, MNRAS, 443, 1979

Latif M. A., Niemeyer J. C., Schleicher D. R. G., 2014b, MNRAS, 440, 2969

Latif M. A., Whalen D. J., Khochfar S., Herrington N. P., Woods T. E., 2022, Nature, 607, 48

Leitherer C. et al., 1999, ApJS, 123, 3

Lemaître G., 1931, MNRAS, 91, 483

Li J. et al., 2025, ApJ, 981, 19

Li W., Inayoshi K., Qiu Y., 2021, ApJ, 917, 60

Lu S., Frenk C. S., Bose S., Lacey C. G., Cole S., Baugh C. M., Helly J. C., 2025, MNRAS, 536, 1018

Lukić Z., Heitmann K., Habib S., Bashinsky S., Ricker P. M., 2007, ApJ, 671, 1160

Lupi A., Haardt F., Dotti M., Fiacconi D., Mayer L., Madau P., 2016, MNRAS, 456, 2993

Lupi A., Haiman Z., Volonteri M., 2021, MNRAS, 503, 5046

Ma Y. et al., 2025, ApJ, 981, 191

Madau P., Dickinson M., 2014, ARA&A, 52, 415

Madau P., Haardt F., Dotti M., 2014, ApJ, 784, L38

Madau P., Rees M. J., 2001, ApJ, 551, L27

Maiolino R. et al., 2025, MNRAS, 538, 1921

Maiolino R. et al., 2024, A&A, 691, A145

Maiolino R. et al., 2024, Astronomy & Astrophysics, 691, A145

Maiolino R. et al., 2024, Nature, 627, 59

Marinacci F. et al., 2018, MNRAS, 480, 5113

Martin J., Ringeval C., Vennin V., 2014, Phys. Dark Univ., 5-6, 75

Matsuoka Y. et al., 2019, ApJ, 872, L2

Matthee J. et al., 2024, ApJ, 963, 129

Mayer L., Capelo P. R., Zwick L., Di Matteo T., 2024, ApJ, 961, 76

Mayer L., Fiacconi D., Bonoli S., Quinn T., Roškar R., Shen S., Wadsley J., 2015, ApJ, 810, 51

Mayer L., Kazantzidis S., Escala A., Callegari S., 2010, Nature, 466, 1082

Mayer L., van Donkelaar F., Messa M., Capelo P. R., Adamo A., 2025, ApJ, 981, L28

McCaffrey J., Hardin S., Wise J. H., Regan J. A., 2023, The Open Journal of Astrophysics, 6, 47

McCaffrey J., Regan J., Smith B., Wise J., O'Shea B., Norman M., 2025, The Open Journal of Astrophysics, 8

Mehta D., Regan J. A., Prole L., 2024, The Open Journal of Astrophysics, 7

Monaghan J. J., Lattanzio J. C., 1985, A&A, 149, 135

More S., Kravtsov A. V., Dalal N., Gottlöber S., 2011, ApJS, 195, 4

Mortlock A., Conselice C. J., Bluck A. F. L., Bauer A. E., Grützbauch R., Buitrago F., Ownsworth J., 2011, MNRAS, 413, 2845

Murray S., Diemer B., Chen Z., Neuhold A., Schnapp M., Peruzzi T., Blevins D., Engelman T., 2021, Astronomy and Computing, 36, 100487

Murray S. G., Power C., Robotham A. S. G., 2013, Astronomy and Computing, 3, 23

Naiman J. P. et al., 2018, MNRAS, 477, 1206

Nandal D., Regan J. A., Woods T. E., Farrell E., Ekström S., Meynet G., 2024, A&A, 683, A156

Naoz S., Yoshida N., Gnedin N. Y., 2012, ApJ, 747, 128

Naoz S., Yoshida N., Gnedin N. Y., 2013, ApJ, 763, 27

NASA, 2025, James Webb Space Telescope. https://science.nasa.gov/mission/webb/

Natarajan P., Pacucci F., Ricarte A., Bogdán Á., Goulding A. D., Cappelluti N., 2024, ApJ, 960, L1

Nelson D. et al., 2019a, Monthly Notices of the Royal Astronomical Society, 490, 3234–3261

Nelson D. et al., 2018, MNRAS, 475, 624

Nelson D. et al., 2019b, Computational Astrophysics and Cosmology, 6

Nobels F. S. J., Schaye J., Schaller M., Ploeckinger S., Chaikin E., Richings A. J., 2024, MNRAS, 532, 3299

Norman M. L., Bryan G. L., 1999, in *Astrophysics and Space Science Library*, Vol. 240, Numerical Astrophysics, Miyama S. M., Tomisaka K., Hanawa T., eds., p. 19

Norman M. L., Bryan G. L., Harkness R., Bordner J., Reynolds D., O'Shea B., Wagner R., 2007, arXiv e-prints, arXiv:0705.1556

O'Leary R. M., McQuinn M., 2012, The Astrophysical Journal, 760, 4

O'Shea B. W., Bryan G., Bordner J., Norman M. L., Abel T., Harkness R., Kritsuk A., 2004, arXiv e-prints, astro, 10.48550/arXiv.astro-ph/0403044

O'Shea B. W., Nagamine K., Springel V., Hernquist L., Norman M. L., 2005, ApJS, 160, 1

O'Shea B. W., Wise J. H., Xu H., Norman M. L., 2015, ApJ, 807, L12

O'Brennan H., Regan J. A., Power C., Ward S., Brennan J., McCaffrey J., 2024, The Open Journal of Astrophysics, 7

Pacucci F., Nguyen B., Carniani S., Maiolino R., Fan X., 2023, ApJ, 957, L3

Peeples M. S. et al., 2019, ApJ, 873, 129

Peiris H. V. et al., 2003, The Astrophysical Journal Supplement Series, 148, 213

Penzias A. A., Wilson R. W., 1965, ApJ, 142, 419

Pérez-González P. G. et al., 2024, ApJ, 968, 4

Perlmutter S. et al., 1999, ApJ, 517, 565

Pillepich A. et al., 2018, MNRAS, 475, 648

Pillepich A. et al., 2019, Monthly Notices of the Royal Astronomical Society, 490, 3196–3233

Pizzati E. et al., 2024, MNRAS, 534, 3155

Planck Collaboration et al., 2014, A&A, 571, A16

Planck Collaboration et al., 2020, A&A, 641, A6

Power C., Knebe A., 2006, MNRAS, 370, 691

Power C., Navarro J. F., Jenkins A., Frenk C. S., White S. D. M., Springel V., Stadel J., Quinn T., 2003, MNRAS, 338, 14

Power C., Robotham A. S. G., Obreschkow D., Hobbs A., Lewis G. F., 2016, MNRAS, 462, 474

Press W. H., Schechter P., 1974, ApJ, 187, 425

Price D. J., 2012, Journal of Computational Physics, 231, 759, special Issue: Computational Plasma Physics

Reed D. S., Bower R., Frenk C. S., Jenkins A., Theuns T., 2007, Monthly Notices of the Royal Astronomical Society, 374, 2, publisher: OUP ADS Bibcode: 2007MNRAS.374....2R

Regan J., 2023, The Open Journal of Astrophysics, 6, 12

Regan J., Volonteri M., 2024, The Open Journal of Astrophysics, 7, 72

Regan J. A., Haehnelt M. G., 2009, MNRAS, 396, 343

Regan J. A., Haehnelt M. G., Viel M., 2007, MNRAS, 374, 196

Regan J. A., Visbal E., Wise J. H., Haiman Z., Johansson P. H., Bryan G. L., 2017, Nature Astronomy, 1, 0075

Regan J. A., Wise J. H., Woods T. E., Downes T. P., O'Shea B. W., Norman M. L., 2020, The Open Journal of Astrophysics, 3, 15

Reines A. E., Volonteri M., 2015, ApJ, 813, 82

Rennehan D., 2022. https://github.com/rennehan/yt-swift/tree/main/yt

Rennehan D., 2024, ApJ, 975, 114

Rezzolla L., Most E. R., Weih L. R., 2018, The Astrophysical Journal Letters, 852, L25

Richards G. T. et al., 2006, AJ, 131, 2766

Riess A. G. et al., 2011, ApJ, 730, 119

Riess A. G. et al., 2016, ApJ, 826, 56

Riess A. G. et al., 2004, ApJ, 607, 665

Robertson B. E., Ellis R. S., Furlanetto S. R., Dunlop J. S., 2015, The Astrophysical Journal Letters, 802, L19

Robertson H. P., 1935, ApJ, 82, 284

Robertson H. P., 1936a, ApJ, 83, 187

Robertson H. P., 1936b, ApJ, 83, 257

Rubin V. C., Ford, Jr. W. K., 1970, ApJ, 159, 379

Savitzky A., Golay M. J. E., 1964, Analytical Chemistry, 36, 1627

Schaller M., Gonnet P., Draper P. W., Chalk A. B. G., Bower R. G., Willis J., Hausammann L., 2018, Astrophysics Source Code Library, ascl:1805.020, ADS Bibcode: 2018ascl.soft05020S

Schaller M., et al., 2024, Monthly Notices of the Royal Astronomical Society, publisher: OUP ADS Bibcode: 2024MNRAS.tmp..925S

Schauer A. T. P., Glover S. C. O., Klessen R. S., Clark P., 2021, MNRAS, 507, 1775

Schauer A. T. P., Regan J., Glover S. C. O., Klessen R. S., 2017, MNRAS, 471, 4878

Schaye J. et al., 2015, MNRAS, 446, 521

Schmidt M., 1963, Nature, 197, 1040

Scholtz J. et al., 2024, A&A, 687, A283

SDSS Collaboration, 2008, *A giant astronomical survey completes its mission: A new mission begins*. https://classic.sdss.org/news/releases/20080815.mission_final.php

Shang C., Bryan G. L., Haiman Z., 2010, Monthly Notices of the Royal Astronomical Society, 402, 1249

Sheth R. K., Mo H. J., Tormen G., 2001, Monthly Notices of the Royal Astronomical Society, 323, 1

Sheth R. K., Tormen G., 1999, MNRAS, 308, 119

Shi Y., Kremer K., Hopkins P. F., 2024, A&A, 691, A24

Shields G. A., 1999, Publications of the Astronomical Society of the Pacific, 111, 661

Skory S., Turk M. J., Norman M. L., Coil A. L., 2010, ApJS, 191, 43

Smith B., Sigurdsson S., Abel T., 2008, Monthly Notices of the Royal Astronomical Society, 385, 1443

Smith B. et al., 2022, *yt_astro_analysis version 1.1.1*. https://zenodo.org/records/5911048

Smith B. D., Regan J. A., Downes T. P., Norman M. L., O'Shea B. W., Wise J. H., 2018, MNRAS, 480, 3762

Spergel D. N. et al., 2003, ApJS, 148, 175

Springel V., 2005, MNRAS, 364, 1105

Springel V., 2010, Monthly Notices of the Royal Astronomical Society, 401, 791–851

Springel V., Frenk C. S., White S. D. M., 2006, Nature, 440, 1137–1144

Springel V. et al., 2017, Monthly Notices of the Royal Astronomical Society, 475, 676–698

Springel V. et al., 2005, Nature, 435, 629

Springel V., Yoshida N., White S. D. M., 2001, New A, 6, 79

Stark D. P., Topping M. W., Endsley R., Tang M., 2025, arXiv e-prints, arXiv:2501.17078

Starobinskiĭ A. A., 1979, Soviet Journal of Experimental and Theoretical Physics Letters, 30, 682

Steinhardt C. L., Kokorev V., Rusakov V., Garcia E., Sneppen A., 2023, ApJ, 951, L40

Sun G., Faucher-Giguère C.-A., Hayward C. C., Shen X., Wetzel A., Cochrane R. K., 2023, ApJ, 955, L35

Tanaka T. L., Li M., 2014, MNRAS, 439, 1092

Thorne J. P., Landt H., Huang J., Hernández Santisteban J. V., Horne K., Cackett E. M., Winkler H., Sanmartim D., 2025, Monthly Notices of the Royal Astronomical Society, 537, 3746–3768

Tremaine S. et al., 2002, ApJ, 574, 740

Tremmel M., Karcher M., Governato F., Volonteri M., Quinn T. R., Pontzen A., Anderson L., Bellovary J., 2017, MNRAS, 470, 1121

Trenti M., Stiavelli M., 2007, ApJ, 667, 38

Trenti M., Stiavelli M., 2009, The Astrophysical Journal, 694, 879

Trenti M., Stiavelli M., 2009, ApJ, 694, 879

Trinca A., Schneider R., Valiante R., Graziani L., Zappacosta L., Shankar F., 2022, MNRAS, 511, 616

Trinca A. et al., 2024, arXiv e-prints, arXiv:2412.14248

Tseliakhovich D., Barkana R., Hirata C. M., 2011, MNRAS, 418, 906

Tseliakhovich D., Hirata C., 2010, Phys. Rev. D, 82, 083520

Turk M. J., Smith B. D., Oishi J. S., Skory S., Skillman S. W., Abel T., Norman M. L., 2011, The Astrophysical Journal Supplement Series, 192, 9, publisher: IOP, ADS Bibcode: 2011ApJS..192....9T

Übler H. et al., 2023, A&A, 677, A145

van den Bosch F. C., More S., Cacciato M., Mo H., Yang X., 2013, MNRAS, 430, 725

Venemans B. P. et al., 2020, ApJ, 904, 130

Vogelsberger M. et al., 2014, Nature, 509, 177

Walker A. G., 1937, *Proceedings of the London Mathematical Society*, 42, 90

Wang F. et al., 2021, ApJ, 907, L1

Warren M. S., Abazajian K., Holz D. E., Teodoro L., 2006, ApJ, 646, 881

Watson W. A., Iliev I. T., D'Aloisio A., Knebe A., Shapiro P. R., Yepes G., 2013, Monthly Notices of the Royal Astronomical Society, 433, 1230–1245

Weinberg D. H., Colombi S., Davé R., Katz N., 2008, ApJ, 678, 6

White S. D. M., Rees M. J., 1978, MNRAS, 183, 341

Wise J. H., 2019, Contemporary Physics, 60, 145

Wise J. H., Regan J. A., O'Shea B. W., Norman M. L., Downes T. P., Xu H., 2019, Nature, 566, 85

Witten C. et al., 2024, Nature Astronomy, 8, 384–396

Wolcott-Green J., Haiman Z., Bryan G. L., 2011, MNRAS, 418, 838

Wolf C., Bian F., Onken C. A., Schmidt B. P., Tisserand P., Alonzi N., Hon W. J., Tonry J. L., 2018, Publications of the Astronomical Society of Australia, 35

Wolf C., Lai S., Onken C. A., Amrutha N., Bian F., Hon W. J., Tisserand P., Webster R. L., 2024, Nature Astronomy, 8, 520–529

Xu H., Ahn K., Wise J. H., Norman M. L., O'Shea B. W., 2014, ApJ, 791, 110

Xu H., Norman M. L., O'Shea B. W., Wise J. H., 2016a, ApJ, 823, 140

Xu H., Wise J. H., Norman M. L., 2013, ApJ, 773, 83

Xu H., Wise J. H., Norman M. L., Ahn K., O'Shea B. W., 2016b, ApJ, 833, 84

Yang J. et al., 2021, ApJ, 923, 262

Yoshida N., Abel T., Hernquist L., Sugiyama N., 2003, ApJ, 592, 645

Yung L. Y. A., Somerville R. S., Finkelstein S. L., Wilkins S. M., Gardner J. P., 2024a, MNRAS, 527, 5929

Yung L. Y. A., Somerville R. S., Nguyen T., Behroozi P., Modi C., Gardner J. P., 2024b, MNRAS, 530, 4868

Zel'dovich Y. B., 1970, A&A, 5, 84

Zhang T., Liao S., Li M., Gao L., 2019, MNRAS, 487, 1227

Zwick L., Mayer L., Haemmerlé L., Klessen R. S., 2023, MNRAS, 518, 2076

Zwicky F., 1933, Helvetica Physica Acta, 6, 110

Zwicky F., 1937, ApJ, 86, 217